Order Number 9432330

Growth modes of Fe on Cu single crystal surfaces

Cao, Yuqun, Ph.D.

City University of New York, 1994

U·M·I
300 N. Zeeb Rd.
Ann Arbor, MI 48106

GROWTH MODES OF Fe ON Cu SINGLE CRYSTAL SURFACES

by

Yuqun Cao

A dissertation submitted to the Graduate Faculty in Physics in partial fulfillment of the requirements for the degree of Doctor of Philosophy, The City University of New York

1994

This manuscript has been read and accepted by the Graduate Faculty in Physics in satisfaction of the dissertation requirement for the degree of Doctor of Philosophy.

4/24/94
Date

Chair of Examining Committee

4/28/94
Date

Edward R. Dayton
Executive Officer

Supervisory Committee:

PEDRO A. MONTANO, D.Sc., Chair

FRED H. POLLAK, Ph.D

HITOSHI HOMMA, Ph.D

MARTEN L. DENBOER, Ph.D

KEGANG HUANG, Ph.D

The City University of New York

ABSTRACT

GROWTH MODES OF Fe ON Cu SINGLE CRYSTAL SURFACES

by

Yuqun Cao

Adviser: Professor Pedro A. Montano

Using the High Resolution Low Energy Electron Diffraction (HRLEED) technique as our primary method, we investigated the initial growth stage of Fe thin films on the Cu(100), (110) and (111) substrates at different deposition temperatures under the Ultra High Vacuum (UHV) environment. We also investigated the thermal stability of the thin films that were grown in various conditions. Our HRLEED measurement shows that the growth of Fe on the Cu surfaces is a complex process. It is far from the simple hetero-epitaxial system that might be expected on the basis of lattice match and mutual immiscibility. The better Fe epitaxial films are grown in the higher temperature regime. The Fe films grown at low and room temperature are not thermal stable and will undergo an irreversible structure re-arrangement when heated to high temperature. The annealing process helps to reduce the defects of the overlayer, thus improve the quality of the thin film. A model of surface atoms re-arrangement is introduced to explain the LEED spot intensity up-shift and the drop of the Fe Auger signal by the annealing process.

ACKNOWLEDGMENTS

To Professor Pedro A. Montano, my thesis advisor, I wish to express the deepest gratitude for his valuable guidance and constant encouragement throughout this thesis work. He also provides the opportunities for me to learn and use the most recent new techniques and to develop the essential skills in research. Those are the most important experiences I have in my graduate study and will continue to benefit me afterwards.

To Professor Hitoshi Homma of Brooklyn College†, I am most grateful for his constant encouragement and valuable discussions. His advises are not limited in the academic but extended to the other aspects of life.

To the other members of the committee, Professor Fred H. Pollak of Brooklyn College, Professor Martin L. DenBoer of Hunter College, and Dr. Kegang Huang of Argonne National Laboratory, I would like to express my sincerest thanks for their agreeing to serve on my committee and carefully reading of this manuscript and helpful advises.

I would like to thank all the faculty in the Physics Department who have been a great help at times of need.

I also wish to acknowledge with gratitude the Department of Physics, Brooklyn College and the Material Science Division, Argonne National Laboratory for the financial support during the course of this work.

Finally, I would like to thank my family for their constant support, encouragement and understanding. I would like to dedicate this work to my lovely wife, Xiaofang, for everything she's done for me.

† Now at the University of Houston

TABLE OF CONTENTS

LIST OF TABLES

LIST OF FIGURES

CHAPTER 1

INTRODUCTION

1.1 Overview

Growing ultra-thin Fe on a single crystal Cu surface has been a challenging subject both technologically and scientifically. The first attempt to grow iron on a copper surface was made more than 30 years ago [1]. Since then it has received considerable attention in research [2-19]. It is an interesting problem due to the special characteristics and properties of the Fe/Cu system. It can be heteroepitaxial grown along some crystallographic directions. Although the stable structure of Fe is bcc (α-Fe), fcc bulk structure of Fe (γ-Fe) exists at high temperature (T= 1183K to 1663K) [20]. The lattice constant of fcc γ-Fe matches closely with that of Cu (Fe = 3.59 Å vs. Cu = 3.61 Å, [20]). The structure parameters are favorable for layer-by-layer growth. However, the thermodynamic data of the Fe/Cu system is unfavorable of either layer-by-layer growth or forming FeCu alloy [21]. In addition to the structural properties, several recent calculations predict that fcc-Fe and particularly, ultra-thin films of fcc-Fe on Cu(100) should have interesting magnetic properties. On the experimental side much controversy has arisen as results conflict with each other and with theoretical predictions [9-19]. The conflicting experimental data on the growth of the thin films and their magnetic properties are indications that other factors, such as surface free energies, diffusion coefficients, and growth conditions (especially the substrate morphology and temperature) play a significant role in the growth process. There are many questions that remain to be clarified and need answer.

In this work, we use High Resolution LEED (HRLEED) [22, 23 and references therein] as our primary method to investigate the initial growth stage of Fe thin films on

the Cu(100), (110) and (111) substrates at different deposition temperatures. We also investigate the thermal stability of the thin films.

1.2 Magnetic Properties of Fe Thin Films

At room temperature the stable phase of Fe is body centered cubic (bcc, α-Fe). At 1183K it switches to face centered cubic (fcc, γ-Fe). The extrapolation of the lattice constant of this fcc phase to room temperature by means of the thermal expansion coefficient yields a value, which differs less than 1% from the lattice constant of fcc Cu at room temperature (see Table 1). Therefore, the epitaxial growth of Fe on Cu(100) offers the possibility to study fcc iron at room temperature. Especially the magnetic properties of these films have been of great interest in the past years. The magnetic properties of α-Fe have been investigated thoroughly and are relatively well understood. In contrast, experimental results on the magnetism of γ-Fe are contradictory. To investigate the magnetic behavior of γ-Fe it is necessary to stabilize this structure at temperatures below the critical temperature for the structural phase transition in Fe. Above this temperature γ-Fe is paramagnetic with a negative Curie temperature. It has been shown that the fcc structure may be stabilized in small Fe precipitates in Fe films on Cu surfaces [24-26]. The present results of the magnetic properties on γ-Fe films on Cu are not definite. Ferromagnetism at room temperature [27-29] as well as paramagnetism at room temperature and a phase transition to antiferromagnetic behavior at low temperature [11, 30-33] was reported for γ-Fe on different Cu surfaces. In photoemission and surface magneto-optical Kerr-effect experiments an easy axis of magnetization perpendicular to the film plane for films thinner than 6 monolayers was found [10, 34]. The axis of magnetization turns into the plane for thicker films [34]. Pappas et al [12] found an irreversible loss of magnetization on heating their thin films above 350K; at this

Table 1. Characteristics of cubic lattices.

	Simple	Body-centered	Face-centered
Volume, conventional cell	a^3	a^3	a^3
Lattice points per cell	1	2	4
Volume, primitive cell	a^3	$\frac{1}{2}a^3$	$\frac{1}{4}a^3$
Lattice point per unit volume	$1 / a^3$	$2 / a^3$	$4 / a^3$
Number of nearest neighbors	6	8	12
Nearest neighbor distance	a	$\sqrt{3}\,a / 2 = 0.866a$	$a / \sqrt{2} = 0.707a$
Number of second neighbors	12	6	6
Second neighbor distance	$\sqrt{2}\,a$	a	a
Packing fraction	$\frac{1}{6}\pi = 0.524$	$\frac{1}{8}\pi\sqrt{3} = 0.680$	$\frac{1}{6}\pi\sqrt{2} = 0.740$

Cu: fcc a = 3.61 Å

α-Fe: bcc a = 2.87 Å

γ-Fe: fcc a = 3.59 Å

temperature they observe an irreversible change of the LEED. Evidence for a strong dependence of the magnetic behavior on the growth conditions, especially the sample temperature during evaporation, was reported in experimental and theoretical work [9]. The results of investigations into the magnetic properties may strongly depend on details of the film preparation. Furthermore, the magnetic properties of thin films may be determined by magnetic anisotropies which depend on temperature and film thickness, as well as by lattice distortions and defects induced by the interface, and the purity of the fcc phase.

1.3 Epitaxial Growth of Thin Films

The term epitaxy refers explicitly to a situation where the structural integrity of the overlayer material (taken as an independent whole) is of at least equal energetic importance when compared to adsorbate-substrate bonding across the interface. Evidently, this occurs only when the separation between adatoms is quite small. The role of adsorbate-adsorbate interactions is not merely to order atoms into particular arrangements on an adsorption checkerboard determined by the substrate. Now these interactions determine a 'natural' lattice constant for the overlayer material.

Pseudomorphy refers to a situation where the overlayer material adopts a crystal structure and lattice constant which differ from their normal bulk manifestations but which match coherently to the underlying substrate. This is the normal state of affairs in submonolayer chemisorption but is highly non-trivial to arrange when the atoms of the deposit material are within a few Angstroms of another.

The crystal growth is not always as presumed in a two-dimensional fashion, one monolayer after the next, up to some desired thickness of overlayer material. As it happens, this actually appears to be the case for Sn/InSb(100) and Sn/CdTe(100). However, it is not the usual situation observed for either the growth of metals on metals

[35] or for the growth of metals on semiconductors [36]. Instead, one often finds that the deposited material 'balls up' into three-dimensional clumps which only later coalesce into a thick polycrystalline film. In fact, extensive experimental results point to the existence of three distinct growth modes. Bauer [37] proposed a topological classification of thin-film growth, in which three principal growth modes were named after their original investigators. As shown in Figure 1, (a) is Frank and van der Merwe [38], with layer-by-layer growth, where the substrate is covered totally by the first atomic layer of the adsorbate, and each following atomic layer is not begun until the underlying one is completed; (b) is Volmer and Weber [39], with growth of three-dimensional islands without a preceding monolayer; and (c) is Stranski and Krastanov [40], with layer growth up to one or more monolayers, followed by growth of three-dimensional islands.

A simple explanation of the different growth modes can be given in terms of the surface energy [37]. If the adsorbate has a surface energy γ_A, the substrate γ_S , and the interface between them γ_I , the condition $\gamma_A + \gamma_S < \gamma_I$ favors wetting of the substrate by the adsorbate, leading to layer-by-layer growth. However, the condition $\gamma_A + \gamma_S > \gamma_I$ favors a non-wetting situation, and therefore the Stranski-Frastanov or Volmer-Weber growth mode. A few suggested examples for Frank-van der Merwe growth are the systems Co/Cu(100) [41], Fe/Au(100) [41] and Ni/W(110) [42]; for Stranski-Krastanov growth Pb/Ag(111) [43] and Pb/Al(111) [44]; and for Volmer-Weber growth Pt/Au(100) [45]. In addition to these principal growth modes, other modes exist which exhibit intermediate behavior, such as the so-called "simultaneous multilayer" growth mode and the "monolayer plus simultaneous multilayer" growth mode proposed by Rhead et al [46].

Figure 1. The three principal modes of thin-film growth: (a) Frank-van der Merwe growth, (b) Volmer-Weber growth, and (c) Stranski-Krastanov growth.

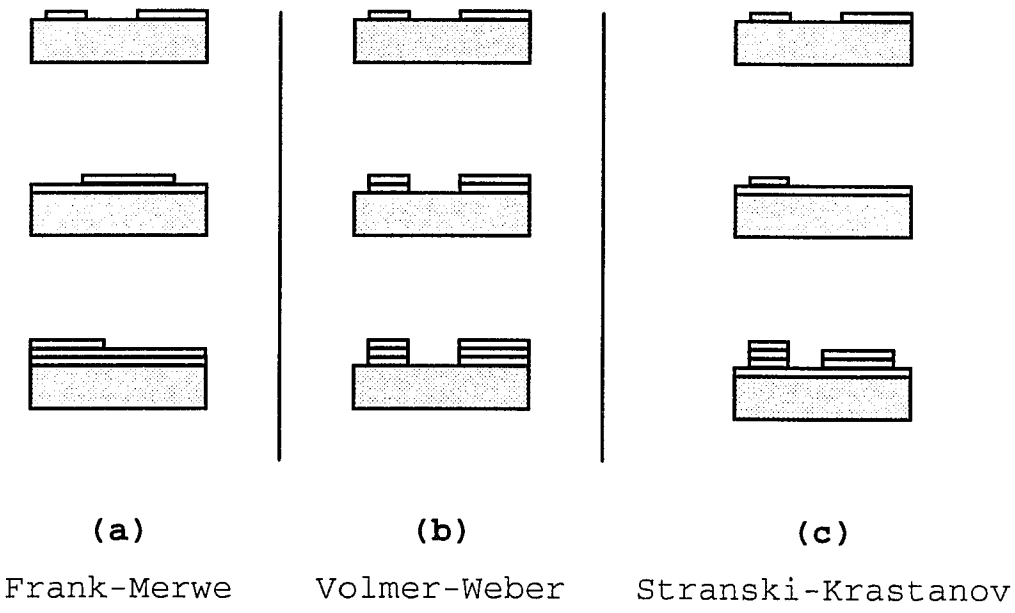

CHAPTER 2

BACKGROUND

2.1 Surface Structures and LEED

Low energy electron diffraction (LEED) is the most widely used technique for analysis of surface structures. The LEED pattern is monitored in nearly all UHV-systems to characterize on the spot the crystallinity or in general the reproducibility of the surface structure.

The information in a LEED pattern is best described with the help of Figure 2. The experimental result is given by the intensity as a function of wave vectors $\mathbf{k}_0$ of the incident wave, and $\mathbf{k}$ of the scattered wave. Restriction to elastic scattering gives $|\mathbf{k}| = |\mathbf{k}_0|$. Since the remaining five free parameters are still too much to handle all at once, further restrictions are needed. In many cases, the pattern consists of spots. By using the existence and arrangement of the spots, very important information on size and shape of the unit mesh can be obtained. If the intensity of those spots is measured (with varying $\mathbf{k}_0$), the positions within the unit mesh are calculated using high computational effort for dynamical calculations. If the surface is described by an arbitrary arrangement of identical units (e.g., unit mesh, domain, island or terrace), then the spot shape may be easily calculated from the arrangement using the kinematical approximation and with a low computational effort. Of course, the peak intensity is not correctly reproduced; therefore the positions within a unit are not determined, but rather the arrangement of units is the result of kinematical evaluation. Since the kinematical approximation yields a predictable periodicity in reciprocal space, its validity is easily checked and has been confirmed up to the measuring accuracy.

Figure 2. The information in the LEED pattern and the possibilities of its evaluation

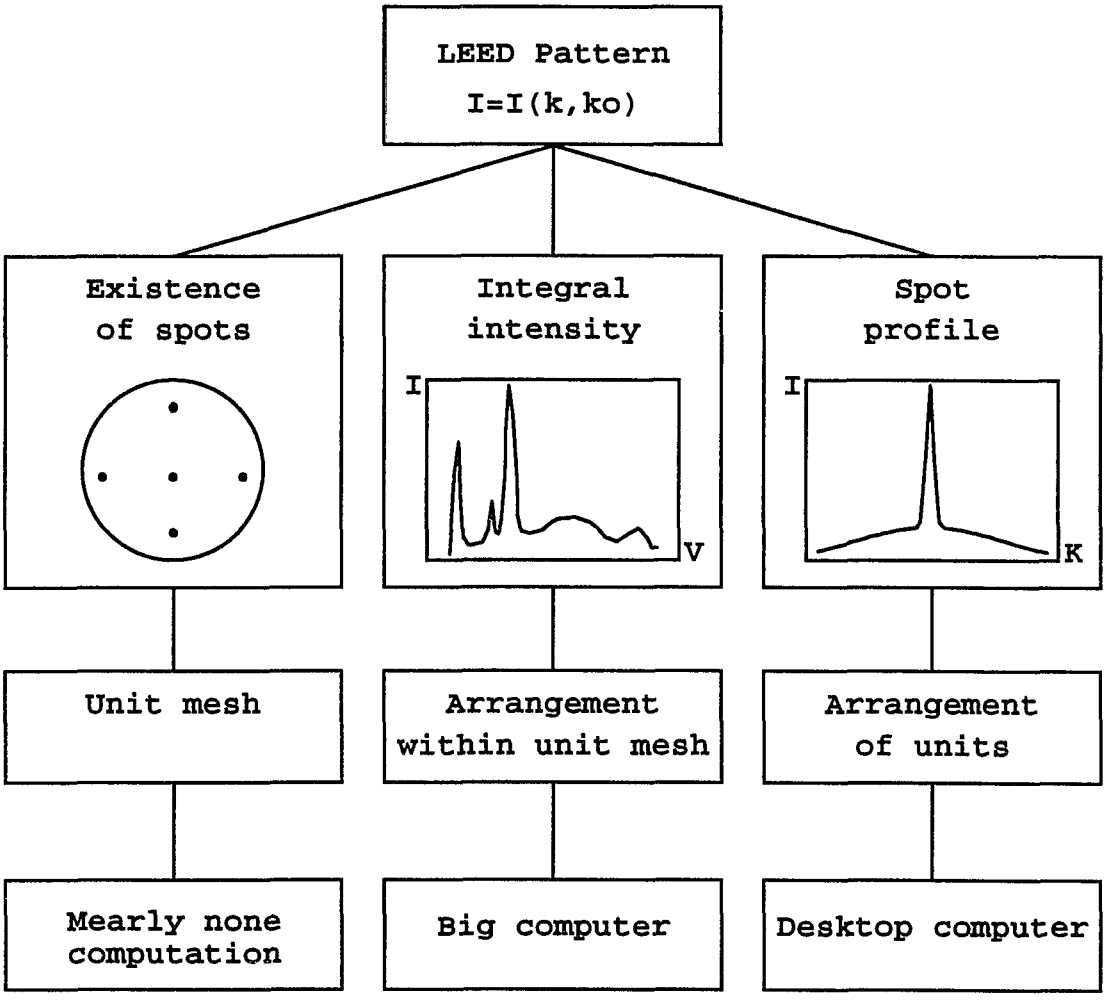

For quantitative analysis during the last decades mostly the intensity of the diffracted spots has been used to obtain, due to a well-developed dynamic theory, the position of the surface atoms within the unit mesh, provided the unit mesh is not too large and the surface is strictly periodic, that means defect-free. A lot of additional information is available as soon as, besides the existence and intensity of a spot, its profile on the screen (in general, profile in k-space) is used. In this way all kinds of deviation, from simple periodicity, periodic or non-periodic, may be derived quantitatively and qualitatively without much computation. With the development of high resolution LEED instruments, the spot profile analysis becomes possible with high accuracy and resolution in k-space providing information about defects on the sample surface or the morphology of adsorbed overlayers. A recently developed HRLEED system can provide resolution of more than 1000 Å [47, 48].

Other techniques are in use for defect characterization: Field ion microscopy provides atomic resolution. It is, however, restricted to the presence of high electric fields and to small areas (smaller than about 30 atomic distances), so that only small defect structures may be observed. Electron microscopy with scanning (SEM) or transmission mode (TEM) operates in bad vacuum or requires replicas, so that a surface is destroyed with respect to the top most atomic layer. The method is nevertheless especially good for extended defects like three-dimensional islands. Scanning tunnel microscopy (STM) shows atomic steps in details. However, it is difficult to obtain quantitative information on average values or probability distribution, since for such values an enormous number of images would be required.

2.2 Electron diffraction from a surface

The surface of crystals may be described by the positions $\mathbf{r}(\mathbf{n})$ of the surface atoms. The wave function of an electron, which is scattered from the initial wave vector $\mathbf{k}_i$ to the final wave vector $\mathbf{k}_f$ by the crystal, is

$$\Psi(\mathbf{K},\mathbf{k}_i) = \sum_{\mathbf{n}} f(\mathbf{n}) \cdot e^{-i\mathbf{K}\cdot\mathbf{r}(\mathbf{n})}, \tag{1}$$

where $\mathbf{K} = \mathbf{k}_f - \mathbf{k}_i$ is the scattering vector. The scattering amplitude $f(\mathbf{n})$ which depends on both the scattering vector $\mathbf{K}$ and the initial wave vector $\mathbf{k}_i$ combines the waves coming from the $\mathbf{n}$-th surface atom and all underlying atoms and includes therefore all dynamic effects of electron diffraction. The wave function itself is not observable, rather the intensity of the diffraction electron beam

$$I(\mathbf{K},\mathbf{k}_i) = \left|\Psi(\mathbf{K},\mathbf{k}_i)\right|^2 = \sum_{\mathbf{n},\mathbf{m}} f(\mathbf{n}) \cdot f^*(\mathbf{m}) e^{-i\mathbf{K}\{\mathbf{r}(\mathbf{n})-\mathbf{r}(\mathbf{m})\}}. \tag{2}$$

Because of the difficulties taking different scattering amplitudes $f(\mathbf{n})$ into account most of the work done on spot profile analysis up to now assume a homogeneous surface: all scattering amplitudes $f(\mathbf{n})$ are approximated by the same amplitude $f = f(\mathbf{K}, \mathbf{k}_i)$, i.e., simple kinematic approximation. Within the simple kinematic approximation we can split the intensity

$$I(\mathbf{K}, \mathbf{k}_i)=F(\mathbf{K}, \mathbf{k}_i)G(\mathbf{K}) \tag{3}$$

into the dynamic form factor

$$F(\mathbf{K}, \mathbf{k}_i)=|f(\mathbf{K}, \mathbf{k}_i)|^2 \tag{3a}$$

and the lattice factor

$$G(\mathbf{K}) = \sum_{\mathbf{n}} \left\langle e^{-idK_\perp[h(\mathbf{n}+\mathbf{m})-h(\mathbf{m})]} \right\rangle_{\mathbf{m}} \cdot e^{-ia\mathbf{K}_{||}\cdot\mathbf{n}}. \tag{3b}$$

Here $\mathbf{r}(\mathbf{n})$ is just written by $\mathbf{r}(\mathbf{n}) = a\mathbf{n} + d_z h(\mathbf{n})$ for a square lattice and brackets $\langle ... \rangle_{\mathbf{m}}$ denote averaging with respect to $\mathbf{m}$.

Often the lattice factor is written with the help of the pair correlation C(**n**, h) which denotes the probability to find two surface atoms separated by a lateral distance a and a vertical distance dh (h denotes an integer):

$$G(\mathbf{K}) = \sum_{\mathbf{n},h} C(\mathbf{n},h) \cdot e^{-idK_\perp h} \cdot e^{-ia\mathbf{K}_\parallel \mathbf{n}}. \tag{4}$$

The lattice factor contains the information about the surface structure because it only depends on the surface profile h(**n**).

A flat, defect free surface produces sharp spots because its lattice factor is

$$G_{ideal}(\mathbf{K}_\parallel) = \sum_{\mathbf{n}} \delta(\mathbf{K}_\parallel - \frac{2\pi}{a}\mathbf{n}). \tag{5}$$

On the other hand, if the surface is rough, on a perfect substrate, the spot consists of a sharp central spike $I_0(K_\perp)$ surrounded by a broadening $I_{diff}(K_\perp,\mathbf{K}_\parallel)$ schematically shown in Figure 3 [48]. The reason for this is that the lattice factor is split into a central part $G_{ideal}(\mathbf{K}_\parallel)$ and a diffuse profile. Here $G_{ideal}(\mathbf{K}_\parallel)$ is due to the summation of the scattered amplitudes at the exact Bragg positions. Its intensity is reduced by a factor $G_0(K_\perp)$ due to destructive interference. If the number of layers is finite, it is $G_0(K_\perp) \neq 0$ for most values of $K_\perp$ (the maximum number of zeros is given by the number of layers). Both, spike and shoulder, vary in intensity with $K_\perp$ periodically:

$$G(\mathbf{K}) = G_0(K_\perp)G_{ideal}(\mathbf{K}_\parallel) + [1 - G_0(K_\perp)]\Phi_{step}(K_\perp,\mathbf{K}_\parallel), \tag{6}$$

where we have introduced a scaled diffuse profile by

$$\Phi_{step}(K_\perp,\mathbf{K}_\parallel) = \frac{I_{diff}(K_\perp,\mathbf{K}_\parallel)}{\int_{BZ} I_{diff}(K_\perp,\mathbf{K}_\parallel)d\mathbf{K}_\parallel}, \tag{7}$$

whose integral intensity varies in anti-phase to the central spike.

Figure 3. Profiles of electron diffraction spots (intensity vs. scattering vector $K_{||}$ at different values for $K_{\perp}$ or energy E) for a randomly stepped surface. Steps at the surface produce a splitting of the spot into a central spike and a broadening. Because of the interference of the electron waves both vary with vertical component of the scattering vector $K_{\perp}$ in anti-phase: at the in-phase condition there is only the central spike, while at the out-of-phase condition the broadening gets its maximum.

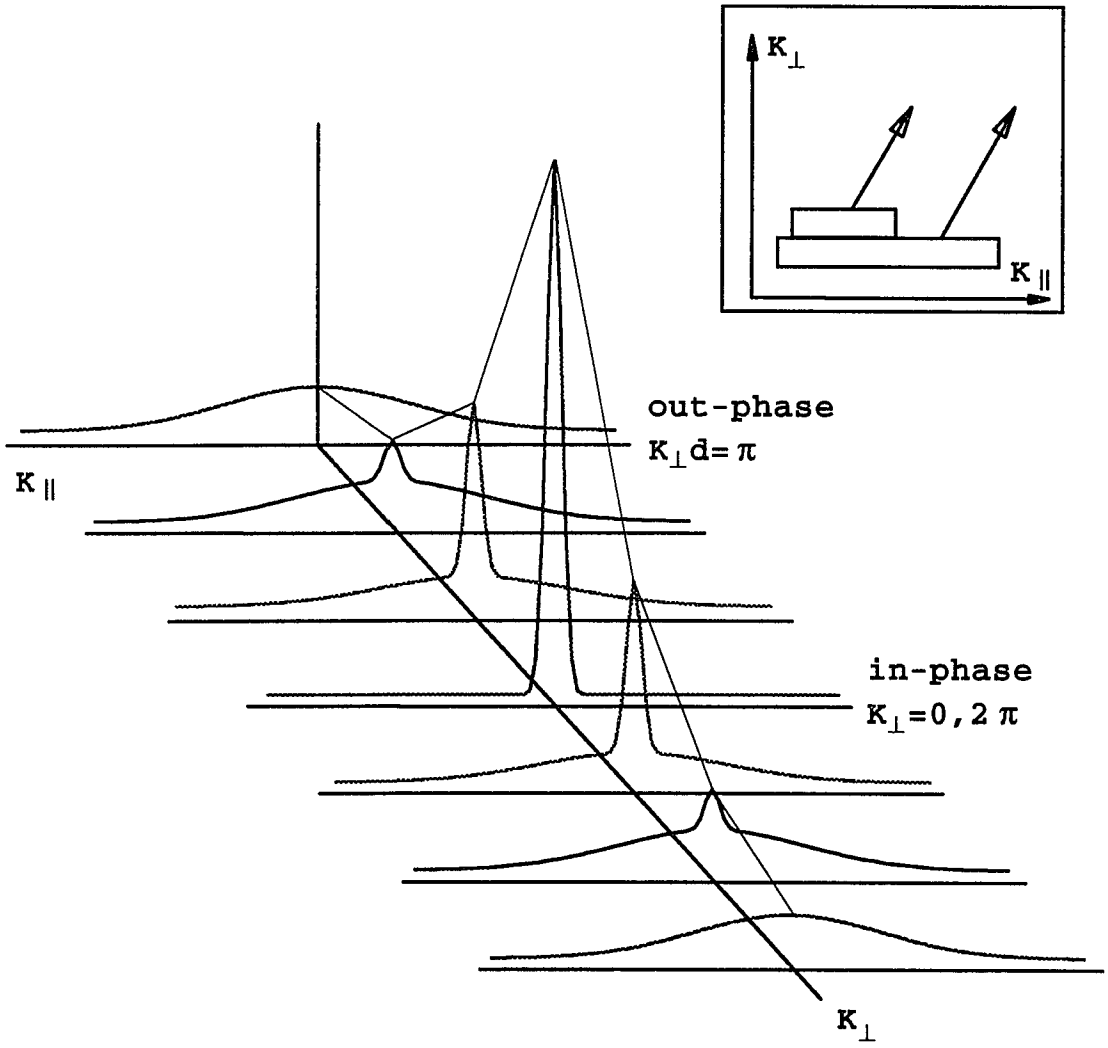

2.3 Diffraction from Defective Surface

A description of a non-periodic surface by given all atom positions is too complicated. In many cases it is sufficient to describe the surface using finite periodic units like terraces or superstructure domains. To evaluate the correlation for a surface of random or of regular arrangement of different sizes, information of how the units are arranged is needed, i.e., the distribution $p_l(\Gamma)$. $p_l(\Gamma)$ is the probability of finding a surface unit at level l with Γ unit meshes in size. The sum over all the surface layers,

$$P(\Gamma) = \sum_l p_l(\Gamma), \tag{8}$$

is the probability of finding a finite unit with Γ unit meshes in size, and the sum over all possible Γ,

$$P_l = \sum_\Gamma p_l(\Gamma), \tag{9}$$

gives the layer distribution which is the probability to find a surface unit in the level l. If the size distribution and the layer distribution are independent of each other, then these two probabilities are a complete description of the averaged surface.

An equivalent variation of the above probabilities are used as well with

$$P'(\Gamma) = \Gamma \cdot P(\Gamma) \Big/ \sum_\Gamma \Gamma \cdot P(\Gamma), \tag{10}$$

giving the probability that an arbitrary surface atom is found on a terrace of width Γ, and

$$P'_l = \sum_\Gamma \Gamma \cdot p_l(\Gamma), \tag{11}$$

is the probability that a surface atom is found on layer l. Figure 4 shows the procedure to derive the terrace and layer distributions from HRLEED intensity and vise versa.

The coherence length is a measure of the surface that interference arises within such distance. Within the coherence length, phase differences follow a pre-determined manner. On the other hand, the waves or particles scattered from distance beyond the coherence

Figure 4. Procedure to derive terrace distribution and layer distribution from HRLEED

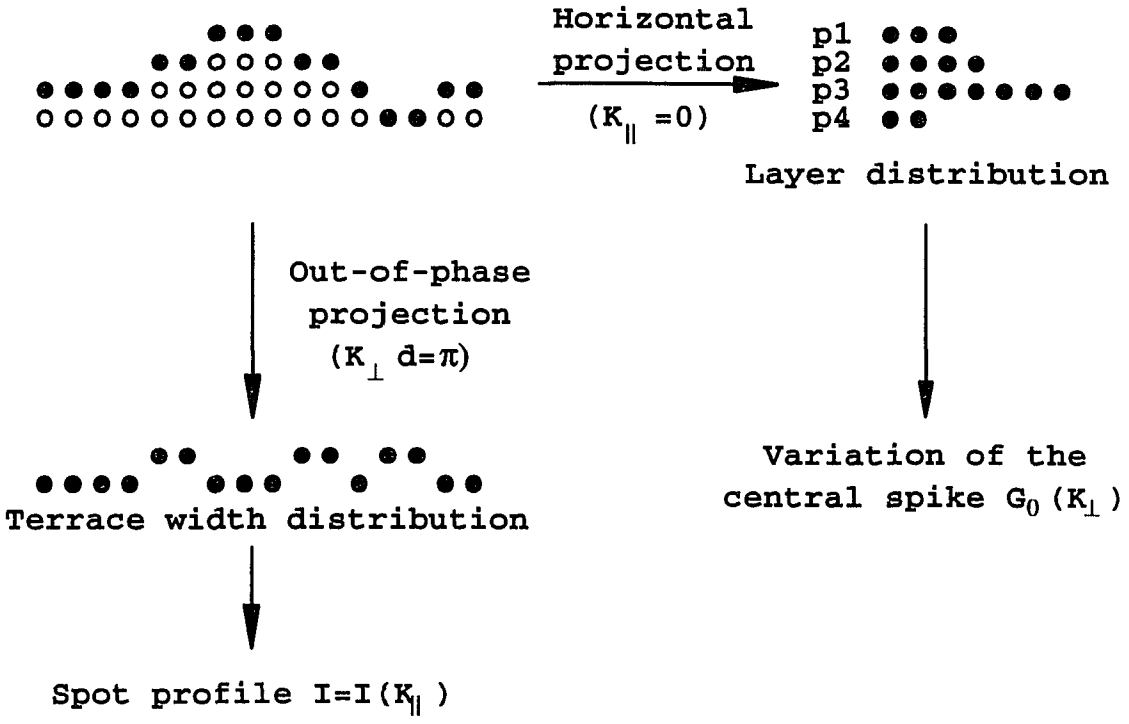

length will not interfere with each other because the phases differ randomly. The total intensity is just the sum of each individual scattered intensity.

In our case, the coherence length of the surface is the average domain size. It is adequate to do the summations in the computation just up to the coherence length since there is not interference between domains,

2.4 Instrumental limitations

The effects of the instrument on the LEED pattern have been carefully described by Park and coworkers [49-51] who used the transfer function t(**x**) and its width (transfer width) to characterize the instrumental limitation. So far, we have tacitly assumed that the diffraction pattern is produced by an ideal instrument, i.e. the electron beam is coherent over the whole sample. For that purpose, we would need a point source with mono-energetic electron emission and an aberration-free focusing device, so that the intensity distribution in the focusing plane I(**K**) is strictly the Fraunhofer diffraction pattern or the Fourier transform of the surface atom arrangement (more exactly of its auto-correlation f(**x**)), where **x** represents the coordinates at the sample surface and $\mathbf{K} = \mathbf{k} - \mathbf{k}_0$ the scattering vector and the coordinates in reciprocal space. To demonstrate the real case in analogy to classical optics, a LEED system is sketched in Figure 5 using optical symbols. The upper part shows the ideal point source which is focused into a δ-function. If a mirror, whose auto-correlation shape is t(**x**), is placed in between, then the focus is broadened to a function T(**K**), which is the Fourier transform of t(**x**). The lower part shows a real arrangement, where due to the finite size of electron source and the optical aberrations, the focus is no more a δ-function but rather a finite function T(**K**), called the instrument response function. According to the coherence conditions of classical optics and using the Fourier theorem, the wave forming T(**K**) is described by a superposition of ideal monochromatic partial waves, each of which constitutes a wave as in the upper part

Figure 5. Transfer width and instrument limitation

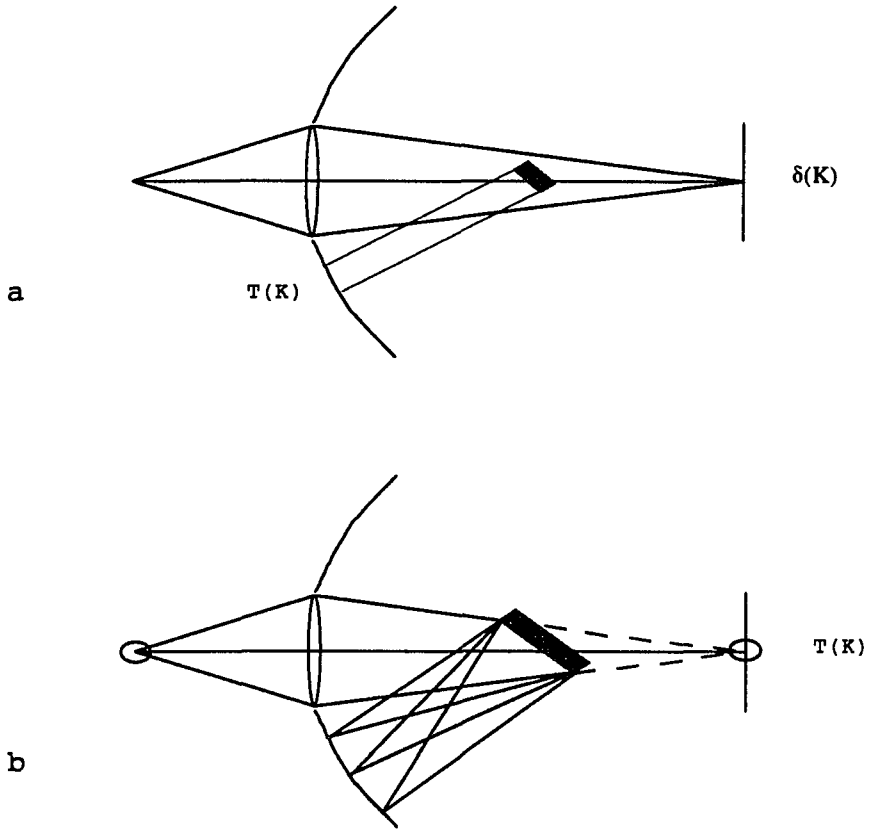

of Figure 5. If a large (ideal) crystal is placed into the beam, the observed pattern on the screen is the diffraction pattern I(**K**) of the crystal with respect to each partial wave. The superposition of all subwaves I(**K**) is approximated by a convolution of I(**K**) with T(**K**),

$$J(\mathbf{K}) = I(\mathbf{K})*T(\mathbf{K}) = F\{f(\mathbf{x})\}*F\{t(\mathbf{x})\} = F\{f(\mathbf{x})\cdot t(\mathbf{x})\}. \quad (12)$$

Here F{...} means Fourier transform. The convolution is strictly correct only for monochromatic sources, taking care of extended source and optical aberrations. For variable energies, the convolution is only approximately correct for limited ranges of **K**. Since the instrument response function T(**K**) may be approximated by a gaussian function, the transfer function t(**x**) may be described in the same way or just by a window, transparent up to a distance t_W, called transfer width. Here t_W is equal to the half-width of the function t(**x**). Therefore, interference for distances wider than t_W is suppressed. The function t(**x**) may be used as in the upper part of Figure 5, taking just a sample of size t_W. The transfer width t(x) provides a complete and correct information on the instrumental limitation.

2.5 Numerical calculation

The diffraction intensity can be computed for a given layer distribution probability p_l by using the method outlined above, and compared to the experimental data. It is possible to obtain quantitative or qualitative information about the surface by comparing the computed results with the experiment results. Figure 6 shows some diffraction spot profiles and their corresponding surface structures.

Here we outline the computer program we developed to analyze the spot profiles. The surface structure can be described by a distribution function,

$$P(l, \Gamma) = \{ \text{ probability of finding a step of size } \Gamma \text{ at layer } l \}. \quad (13)$$

Γ is the step size and l is the layer number (l = 0 for the substrate, see Figure 7). The following quantities can be derived from $P(l, \Gamma)$,

a. size distribution $P(\Gamma)$ = { probability of finding a step with size G }

$$= \sum_{l} P(l,\Gamma);$$

b. layer distribution $P(l)$ = { probability of finding a surface atom at layer l }

$$= \sum_{\Gamma} \Gamma \cdot P(l,\Gamma);$$

c. step distribution P_l = { probability of finding a step at layer l }

$$= \sum_{\Gamma} P(l,\Gamma);$$

d. coverage θ

$$= \frac{\sum_{l,\Gamma} l \cdot \Gamma \cdot P(l,\Gamma)}{\sum_{l,\Gamma} \Gamma \cdot P(l,\Gamma)}$$

To simplify the model for the computation, we assume that l and Γ are independent,

$$P(l, \Gamma) = P_l \cdot P(\Gamma). \tag{14}$$

To compute the diffraction intensity with given P_l and $P(\Gamma)$, we need to generate a set of surfaces according to the distributions. The following procedure will generate a surface,

```
procedure
Start from n = 0
Repeat until n reaches the coherence length
   generate an l_j using P_l, generate an Γ_j using P(Γ)
   the next Γ_j atoms will be on layer l_j
   n ← n + Γ_j
end.
```

For each generated surface, the diffraction amplitude is

$$A(K) = \sum_{j} e^{iK \cdot R_j} \tag{15}$$

Figure 6. Spot profiles for a flat surface, a stepped surface within two levels, random steps and steps with regular size or regular distance.

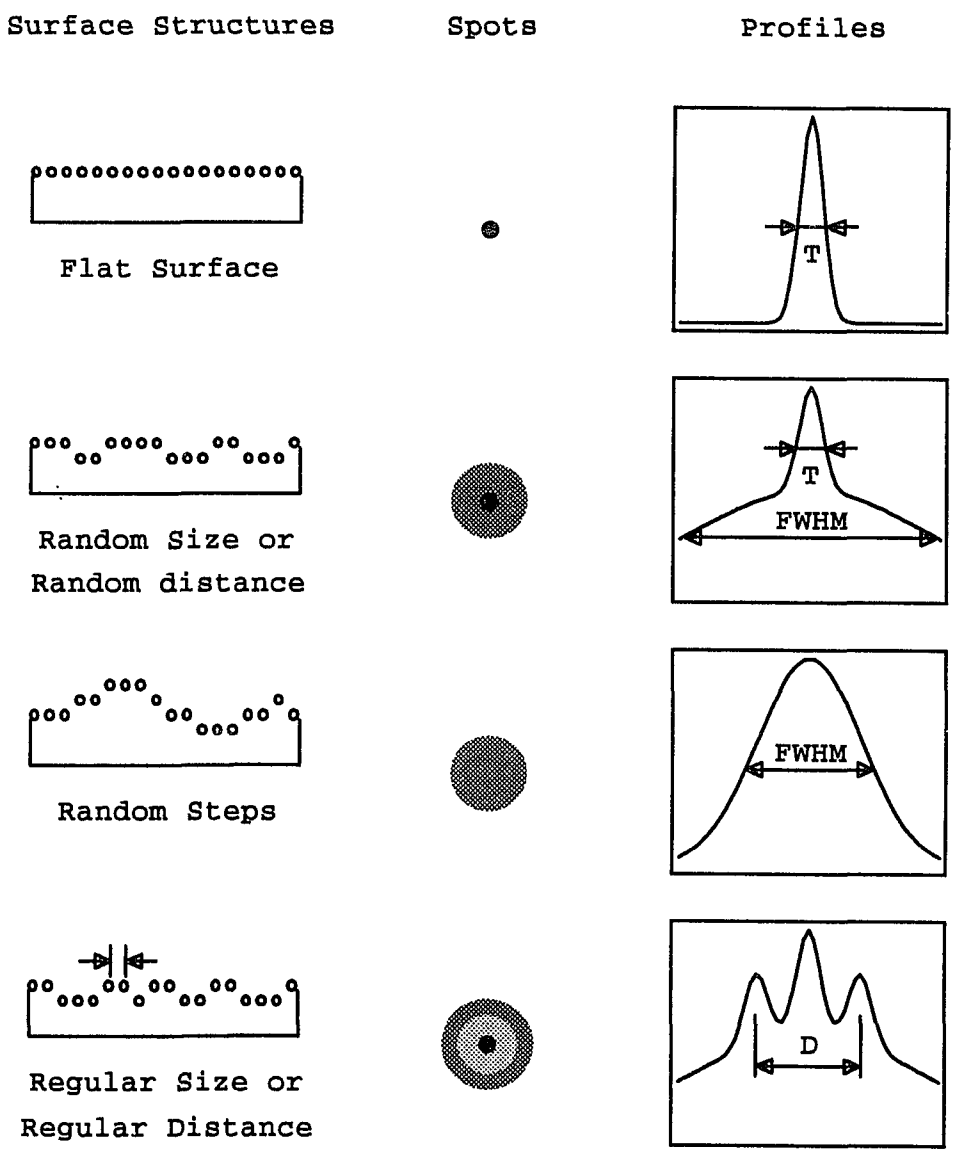

Figure 7. Computational model of surface.

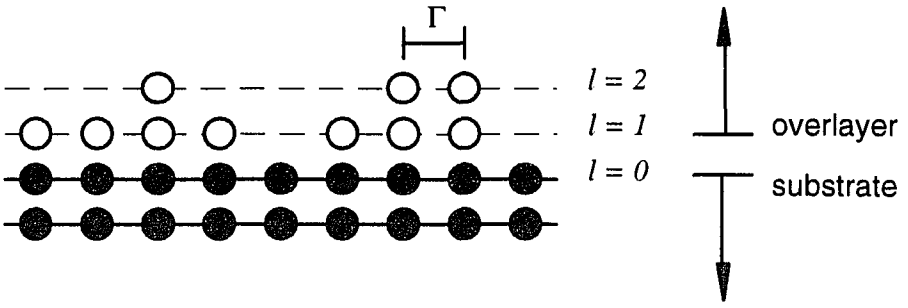

Figure 8. Computed spot profile

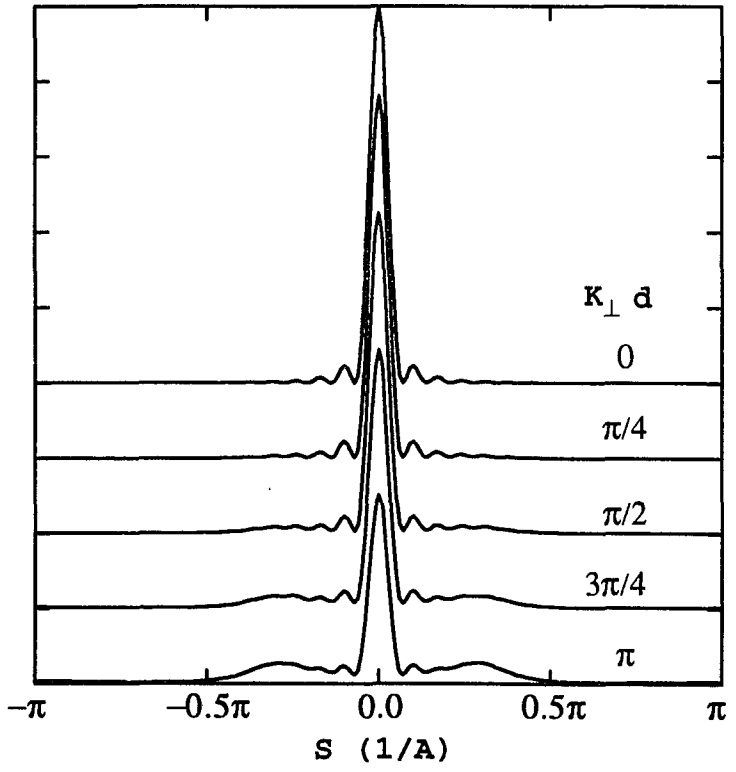

where

$\mathbf{K} = \mathbf{k}_f - \mathbf{k}_i$, (momentum transfer)

$\mathbf{R}_j = \mathbf{a}\cdot n_x + \mathbf{b}\cdot n_y + \mathbf{d}\cdot l$, (surface atom position)

and

j is bounded by the coherence length. The total intensity is then the average of the intensities from all the generated surfaces:

$I(\mathbf{K}) = \langle |A(\mathbf{K})|^2 \rangle$.

It is difficult to generate a 2-dimensional surface that satisfies a given distribution function, so we use 1-dimensional model instead,

$\mathbf{R} = \mathbf{a}\cdot n + \mathbf{d}\cdot l$

$\mathbf{K}\cdot\mathbf{R} = K_{\parallel}\cdot\mathbf{a}\cdot n + K_{\perp}\mathbf{d}\cdot l$.

The in-phase and out-phase condition are given by:

$K_{\perp}d = 2\pi i$ (16)

and

$K_{\perp}d = (2\pi+1)i$ (17)

where i is some integers. Figure 8 is the computed result of a 2-layer system with the following parameters: coherence length = 30 atomic distances; l = 0, 1, 2 with $p_0 = p_1 = p_2 = 1/3$; Γ = 1, 2, 3, 4, 5 with P(3) = 0.56, P(2)=P(4) = 0.21, P(1)=P(5)=0.01 (Gaussian distribution). The coverage θ = 1ML in this case.

2.6 LEED Temperature Dependence Based on the Debye Model

The thermal vibration causes the atoms moving around their equilibrium positions. This will add a random phase to the scattering factor of each atom. Thus the LEED intensity would be averaged on the atomic displacement.

$$\langle I(\mathbf{K},\mathbf{k}_i)\rangle_T = \left|\Psi(\mathbf{K},\mathbf{k}_i)\right|^2 = \sum_{n,m} f(\mathbf{n})\cdot f^*(\mathbf{m}) e^{-iK\{r(n)-r(m)+\Delta P(t,n,m)\}} \quad (18)$$

where ΔP counts the displacement of the atom from the equilibrium position and <...> means taking the average. Assuming a complete random phase, we then have the average

$$< I >_T \propto e^{\frac{1}{2}<|\mathbf{K}\cdot\Delta\mathbf{P}|^2>_T} = e^{-2M} \tag{19}$$

Using the Debye model of the density of the state for the thermal vibration, which assume the linear dispersion relation and a cutoff frequency ω_D, we get the Debye-Waller factor

$$2M = \frac{3\hbar^2|\mathbf{k}-\mathbf{k}'|^2}{2m_a k_B \Theta}\left[\left(\frac{T}{\Theta}\right)^2 \int_0^{\frac{\Theta}{T}} \frac{x}{e^x - 1} dx + \frac{1}{4}\right] \tag{20}$$

where $\Theta = \frac{\hbar c}{k_B}\frac{2\pi}{b}\left(\frac{3}{4\pi}\right)^{\frac{1}{3}}$ is the Debye temperature and b the lattice constant. At high temperature ($T >> \Theta$), it approximates to

$$2M = \frac{3\hbar^2 T|\mathbf{k}-\mathbf{k}'|^2}{2m_a k_B \Theta^2} \tag{21}$$

2.7 Auger Electron Spectroscopy (AES) and Thin Overlayer

In 1925, P. Auger first observed the so-called Auger electrons in a Wilson cloud chamber [52]. He explained this occurrence as being due to a radiationless transition in atoms excited by a primary x-ray photon source. In 1953, Lander first pointed out that Auger electrons arising from solid samples can be detected in the energy distribution curve of secondary electrons from surfaces subjected to electron bombardment [53]. Moreover, low-energy Auger electrons (~1 keV kinetic energy) can escape from only the first several atomic layers of a surface since they are strongly absorbed by even a monolayer of atoms. Thus Auger electron spectroscopy (AES) possesses high surface sensitivity. This is one characteristic that makes AES very useful for the study of thin films. For such applications, an important development in AES occurred when Harris showed that the sensitivity of the detection of Auger electrons can be improved by differentiating the

electron energy distribution curve with respect to the energy [54]. Furthermore, Weber and Johnson demonstrated that, provided the Auger line profile does not change, the peak-to-peak height in the differentiated energy distribution curves is proportional to the Auger current in the peak [55]. Therefore, in addition to its surface sensitivity, AES also can be used for quantitative studies of thin films.

The Auger process involves three energy levels: an empty core level (E_1) and two higher levels (E_2 and E_3), Figure 9. In this internal process, an electron from one of the higher levels fills the core level while the other is ejected with the balance of the energy. So the kinetic energy E of the ejected electron (called an Auger electron after its discoverer) is approximately given by

$$E = E_1 - E_2 - E_3 , \qquad (22)$$

where the binding energies are taken to be positive numbers. The emitting electron can also come from the same level from which another electron fills the empty core level, i.e., $E_2 = E_3$. This is called the Kronig transition. The empty core level is typically created by bombarding the specimen with an electron beam of several keV.

The surface sensitive nature of AES is a result of the short inelastic mean free path (IMFP) of the emitted electrons. For example, the IMFP of a 50 eV electron in a solid is about 5Å and increases slowly with kinetic energy approximately as $\sqrt{E}$ [56]. Only those electrons which have not scattered inelastically emerge from the sample with the characteristic energy of the element that emitted them. Since most elements have electrons with binding energies (and therefore ejected Auger electron energies E) in the 50-1500 eV range, they have short IMFPs and high surface sensitivity.

Figure 10 shows the geometry for an Auger experiment involving a thin uniform overlayer of element A on a semi-infinite substrate of element B. The interface between the alloy overlayer and the B substrate is assumed to be perfectly sharp. We can derive the

Figure 9. Creation of an Auger electron. The core electron at the energy level E1 is knocked out by energetic electrons or photons leaving a hole behind, denoted by the small white circle. One of the higher level electrons (the black circles, at level E2 and E3) fills in the hole while another electron (called the Auger electron) is ejected with the balance of the energy. The ejected electron has a characteristic energy that can be used to identify the element of the atom.

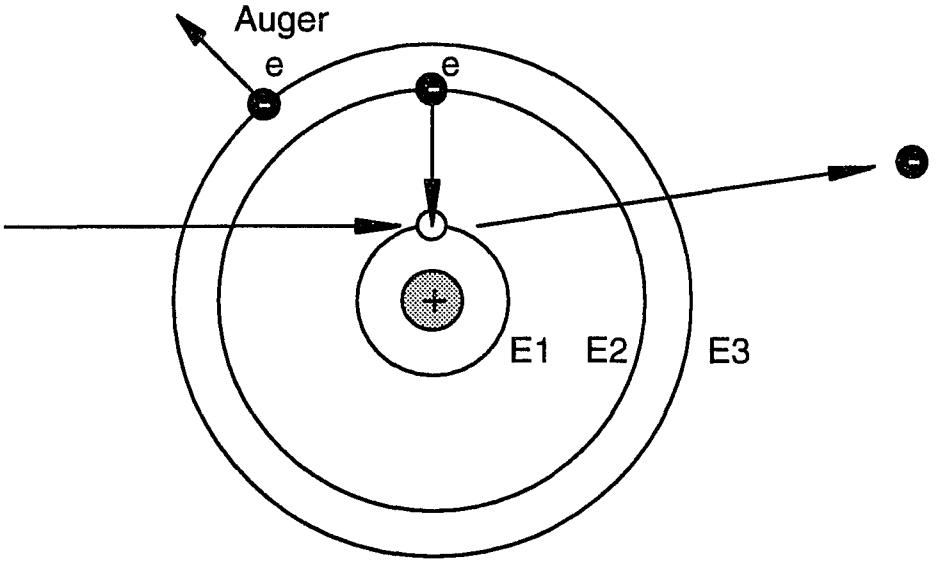

Figure 10. Geometry for the case of a uniform overlayer of element A on a substrate of element B. The Auger intensity changes exponentially with overlayer thickness *d*.

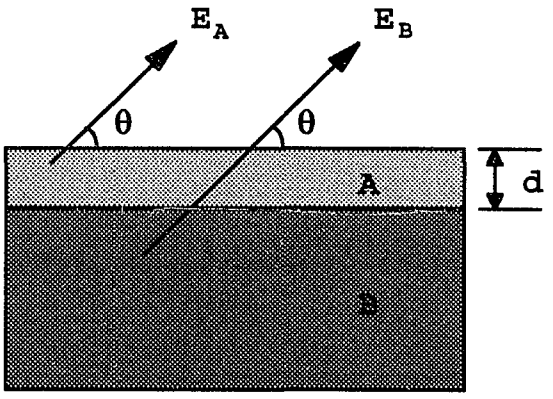

Thin film limit:

$$\frac{I_A(d)}{I_A^\infty} = (1 - e^{-d/\lambda_A(E_A)\cos\theta})\left(\frac{R_B(E_A)}{R_A(E_A)}\right)$$

$$\frac{I_B(d)}{I_B^\infty} = e^{-d/\lambda_A(E_B)\cos\theta}$$

The corrected intensity I_A is approximately given by:

$$\frac{I_A}{I_A^\infty} = \frac{I_A(d)}{I_A^\infty}\left(1 + \left(\frac{R_B(E_A)}{R_A(E_A)} - 1\right)e^{-d/l_A}\right)$$

where

$R_\mu(E_A) = 1 + r_\mu(E_A)$ for μ = A and B

E_A, E_B: Auger energy of interest

λ_A, λ_B: inelastic mean free path

r_A, r_B: backscattering factor

l_A: characteristic backscattering length

intensities as a function of the overlayer thickness d by making the usual (and usually valid) assumption that the interaction of the electrons as they travel through the solid can be characterized by an inelastic mean free path λ. Then the intensity of B is just that of the bulk material I_B^∞ attenuated by the overlayer,

$$\frac{I_B(d)}{I_B^\infty} = e^{-d/\lambda_A(E_B)\cos\theta}. \tag{23}$$

The intensity of A is somewhat complicated by the fact that the backscattered electrons are from material B. For the case of a thin overlayer, all of the backscattering occurs in B. In this case, the contribution to the Auger intensity of A atoms excited by these backscattered electrons can be written as $I_{A_p} r_B(E_A)$, where I_{A_p} is the contribution from atoms excited by the primary beam. The backscattering factor for element B. $r_B(E_A)$, is a function of the primary beam energy E_p, the angle of incidence of the primary beam, and the Auger energy of interest (E_A in this case). Then the total Auger intensity for A is given by

$$I_A(d) = I_{A_p}(d)(1 + r_B(E_A)). \tag{24}$$

Similarly, the intensity from bulk element A (our intensity reference) can be written as

$$I_A^\infty = I_{A_p}^\infty (1 + r_A(E_A)). \tag{25}$$

Combining Equations 24 and 25 with the analog of Equation 23 for the overlayer results in the following equation for the overlayer intensity,

$$\frac{I_A(d)}{I_A^\infty} = (1 - e^{-d/\lambda_A(E_A)\cos\theta})\left(\frac{R_B(E_A)}{R_A(E_A)}\right) \tag{26}$$

where $R_\mu(E_A) = 1 + r_\mu(E_A)$. Equations 23 and 26 describe the intensities in the limit of a "thin" film.

Figure 11 illustrates a typical spectrum of Auger experiment. A 3-5 keV electron beam is used to excite the specimen and the ejected electrons are energy analyzed. Auger

Figure 11. Spectrum for a Fe/Cu overlay showing the peaks from Auger electrons and the elastically scattered primary beam.

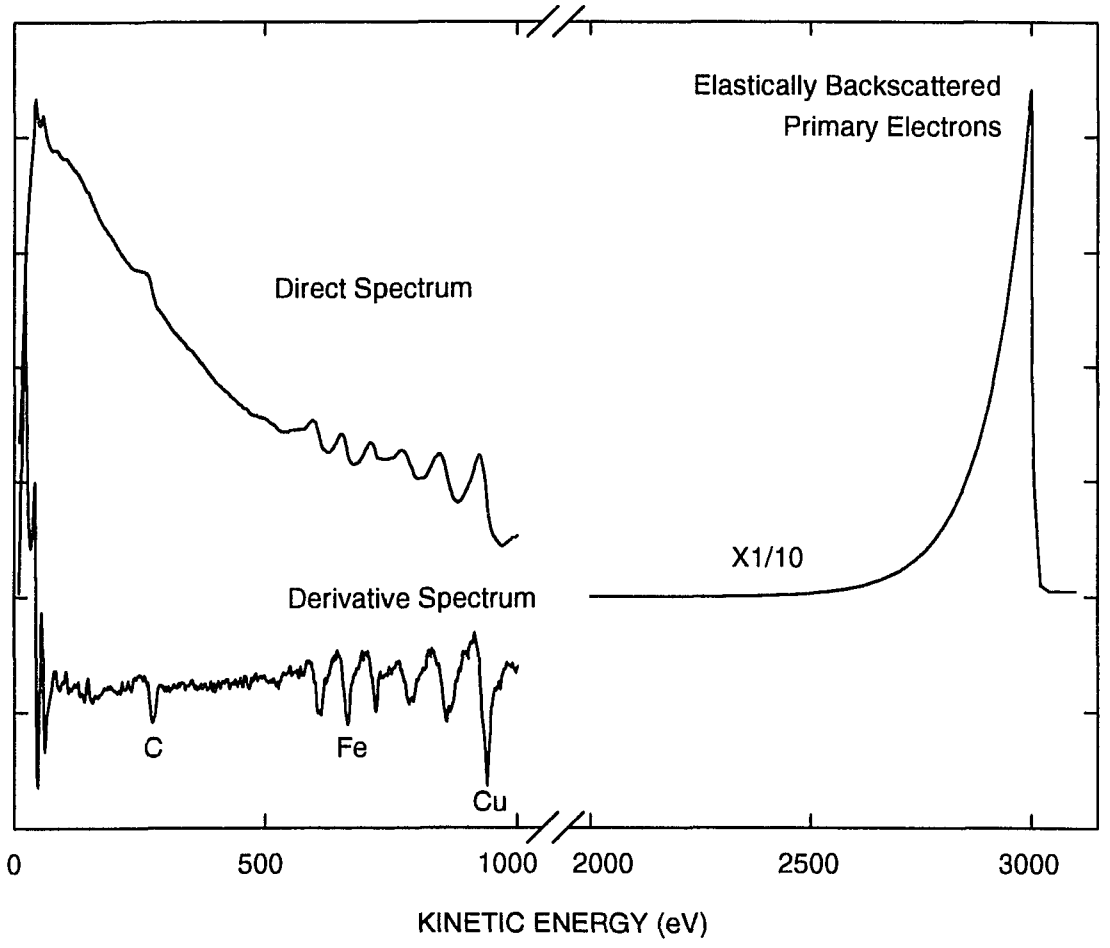

electrons manifest themselves as small peaks riding on a high background of inelastically scattered electrons. Also, each peak is asymmetric due to a tail of inelastically scattered Auger electrons on the low-energy side of the peak. Because of this high background signal and peak asymmetry, the traditional way to treat Auger spectrum is to acquire a derivative spectrum or take the derivative numerically. The result is a curve with strong negative excursions corresponding to the high-energy side of each Auger peak in the direct spectrum. For practical reasons, the Auger energies are usually defined to be the positions of these negative excursions.

CHAPTER 3

EXPERIMENTAL SETUP AND RESULTS

3.1 Experimental Setup and Description

The experiments are carried out in an ultra high vacuum (UHV) chamber (base vacuum $2x10^{-11}$ torrs). Figure 12 is the schematic diagram of the system.

The impurity sensitive surface experiments place a high demand on the vacuum system. Many UHV techniques are employed in our vacuum system to achieve the desired vacuum level. A rotary pump and a powerful turbo pump serve as the fore-vacuum stage. The turbo pump is essential to our experiment because it produces a clean vacuum without the mess of a diffusion pump. The turbo pump is also fast. It can reach 10^{-5} torr in less than 15 minutes and go below 10^{-7} torr easily. A huge ion pump is attached to the bottom of the chamber. It is switched on to obtain the ultra high vacuum when the turbo pump can not improve the vacuum further. Each time the chamber is opened and the sample changed, the chamber is filled with nitrogen gas to minimize the exposure of the UHV components to the air because any contamination will affect the UHV environment. Thus, the whole UHV system is baked at 150 °C overnight to allow a thorough out-gassing of the components when the system is sealed back again. A Titanium sublimation pump, as part of the ion pump, is fired occasionally to get rid of the remaining active elements in the vacuum chamber. Under normal operation condition, only the ion pump is left on all the time to maintain the UHV at the 10^{-10} torr region. Another technique to push to a higher vacuum is to flow liquid nitrogen through pipes embedded in the chamber. This allows us to run the experiment at 10^{-11} torr with the minimum impurity contamination.

Figure 12. Schematic drawing of experiment setup

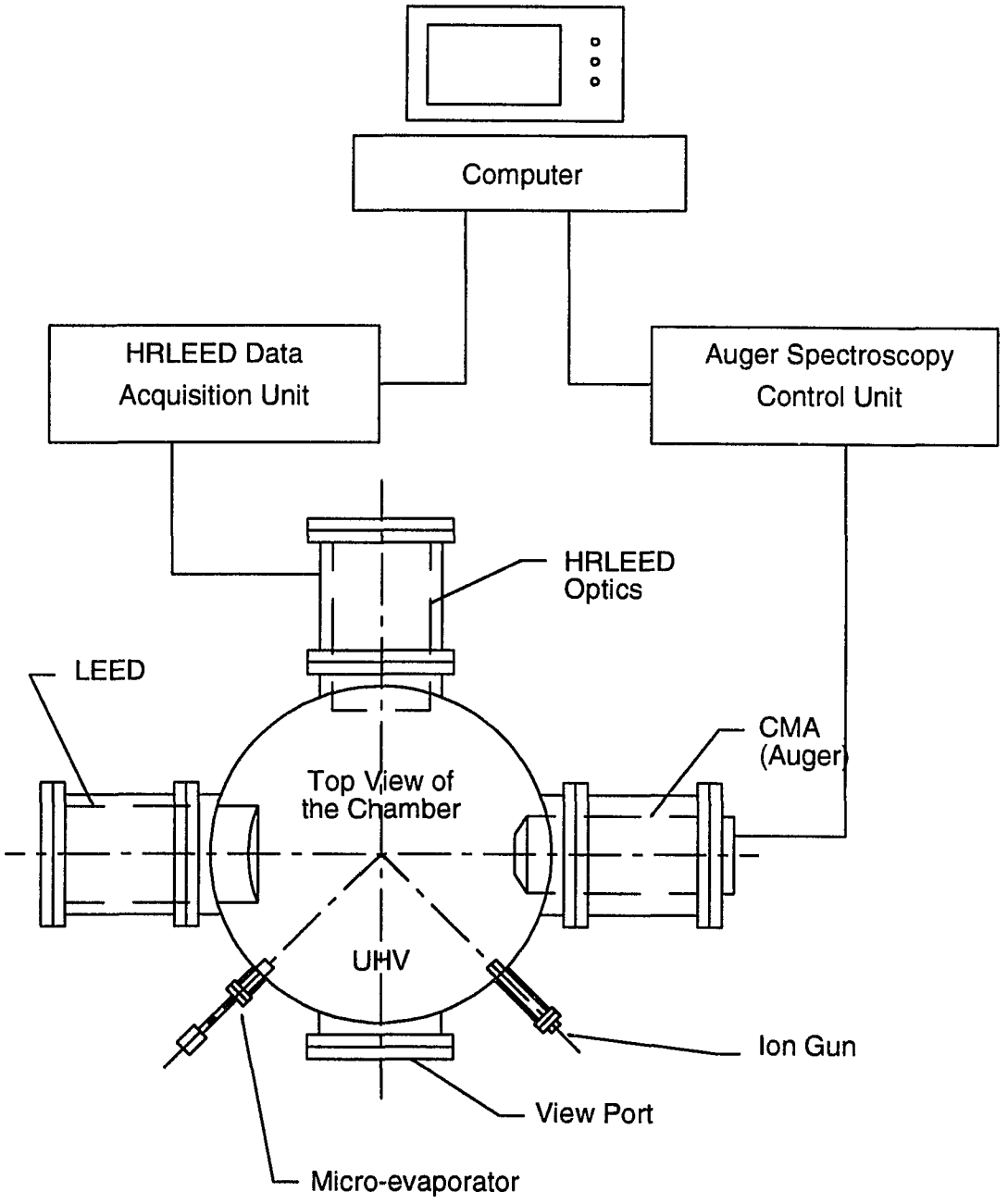

The sample is mounted on a precision manipulator (X-, Y- and Z-transition, Φ- and θ-rotation) and is positioned at the center of the chamber. Micrometers are used to set the sample position. The ranges of movement are ±1 inch in X- and Y-directions, 5 inches in Z-direction, 360° for Φ, and -5° to 30° for θ. The sample temperature can be set between 150K and 1000K by means of LN_2 cooling and electron beam heating on the back of the sample holder.

The ion gun operating with 500 eV Ar ions at 10^{-6} torr is used to clean the Cu surface. The ion gun is a simple device that produces energetic ion beam. To do the sputtering, the valve to the ion pump is shut and the Argon gas is first introduced into the chamber to the desired pressure before the sputtering begins. The Ar atoms are ionized near the filament of the ion gun and extracted out through a grid with negative voltage. The ions are accelerated to certain energy by the electric field before leaving the ion gun. The ion flux is controlled by the filament current and the Ar partial pressure while the ion energy is adjusted by the voltage applied to the electrode. Other controls such as the focus and deflection are also built in the ion gun. During the sputtering process, the Ti sublimation pump is fired periodically to keep the chamber clean.

The cylindrical mirror analyzer (CMA) is used to monitor the surface composition by measuring the Auger electron spectroscopy (AES) . A schematic drawing of the CMA is shown in the Figure 13. The primary energy of the electrons from the electron gun is adjustable from 0 to 5 keV. The two cylinders in the analyzer act as a mirror and only the electrons with the selected energy can pass through the aperture at each end of the inner cylinder. The electrons are then collected and the current is amplified by the electron multiplier. The energy is selected by the voltage applied to the cylinders.

The micro evaporator is used to deposit iron on the copper surface. It produces a point source evaporation of metals by accelerating electrons and bombarding a thin pure

Figure 13.The Cylindrical Mirror Analyzer (CMA) for measuring the Auger Electron Spectroscopy (AES).

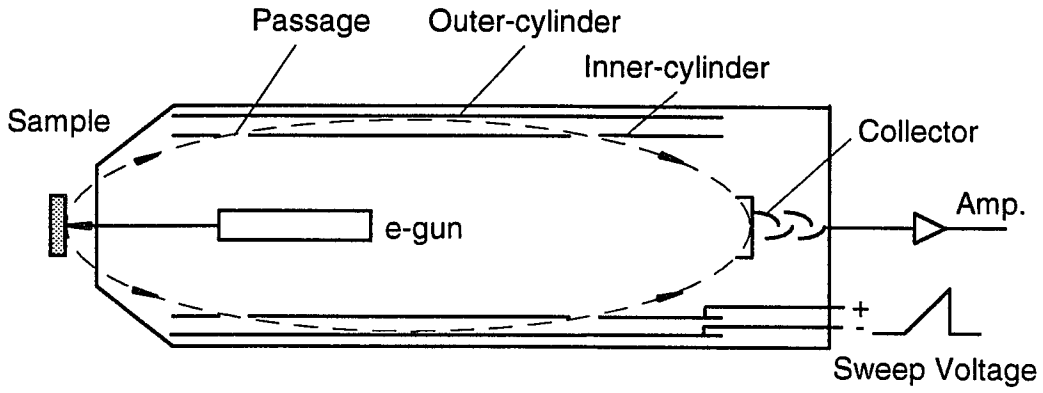

Figure 14. Schematic diagram of the micro-evaporator

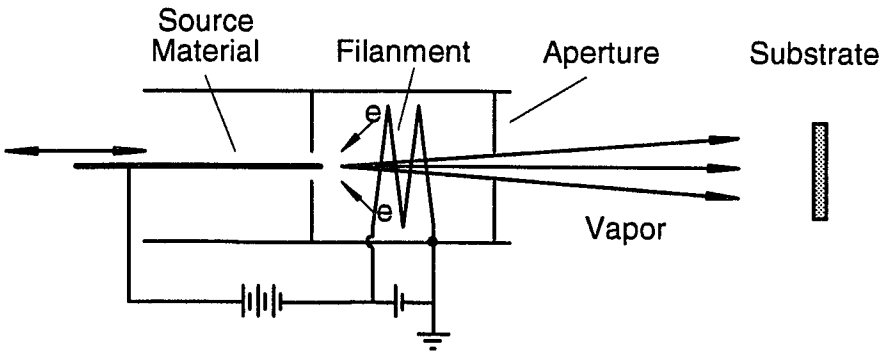

metal wire, Figure 14. The source wire can be moved in and out to control the rate and the amount of the evaporation. This method does not introduce any contamination from the source and provides an accurate deposition control.

Another unit in the system is a conventional LEED system. It is used to check the surface cleanness, smoothness and identify the crystal orientation.

The central unit for the measurement is the HRLEED system, Figure 15. Beside the usual visual inspection of an electron diffraction pattern with a fluorescent screen, this high resolution LEED instrument allows direct quantitative determination of the electron intensity distribution. For this purpose, the LEED pattern can be moved across the entrance aperture of a channeltron detector by means of two octopole fields. The electron gun in the system is a one-lens electrostatic unit optimized for small cross over diameter at low energies. It is composed of a tungsten hairpin filament with pointed tip, an extractor lens, a floatable anode, and an electrostatic lens. The electrons leaving the e-gun are deflected away from the electron optical axis by the electrical field of the first, shorter octopole. The field of the second, longer octopole deflects them back again towards the optical axis. In the simplest approximation the electron path from the gun to the crystal is thus composed of two parabolas. The ratio of the voltages applied to the first and second octopoles is chosen appropriately so that the primary electrons hit the crystal surface at the same point independent of the absolute value of these voltages. The angle of incidence, however, varies with the deflection potential. The diffracted electrons leaving the crystal pass the octopoles in the opposite direction: they are first deflected by the longer octopole and then by the short one. By scanning the octopole voltages the beam thus rocks in one point on the crystal surface so that the directions of the diffracted electrons with respect to the axis of the optical axis changes and the reflex pattern shifts across the detector. During a scan the angle between primary beam and those scattered electrons which just reach the channeltron remains constant. Its value is determined by the mechanical construction and

Figure 15. Schematic drawing of the HRLEED optics

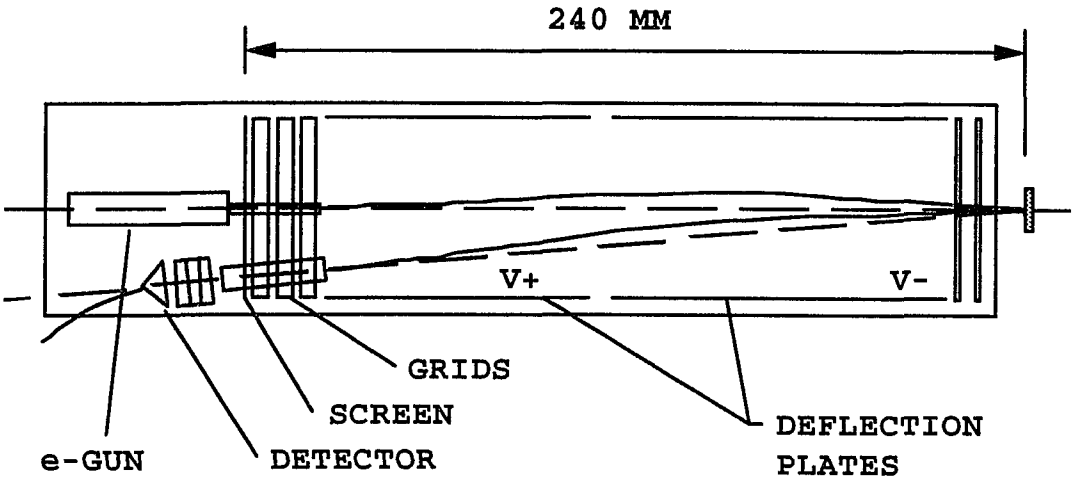

The limited instrument response of a LEED system is caused by the following major factors: the detector aperture diameter, the electron source extension, the incident electron beam diameter, and the energy spread of the beam.

$$K_{||}=2\pi\sqrt{E/150}(\sin\theta-\sin\theta_0)$$

$(\Delta K_{||})_{\Delta E}=\pi\Delta E/\sqrt{150E}\ (\sin\theta-\sin\theta_0)$	(energy spread ΔE)
$(\Delta K_{||})_{\Delta\theta}=2\pi\sqrt{E/150}\ (\cos\theta)\ \Delta\theta\ |_{\Delta\theta=d/R}$	(effective aperture d/R)
$(\Delta K_{||})_{\gamma}=2\pi\sqrt{E/150}\ (\cos\theta_0)\ \gamma\ |_{\gamma=\theta_0}$	(source extension γ)
$(\Delta K_{||})_{D}=2\pi\sqrt{E/150}\ \frac{\cos^2\theta}{\cos\theta_0}\frac{D}{R}$	(beam diameter D)

d=0.1 mm, R=240 mm, D=1 mm, $\gamma=d_S/R$=0.8 mm/240 mm=3.3 mrad

amounts to 7.5 degree. This method of spot profile analysis allows high accuracy and resolution in k-space, providing information about defects on the sample surface or the morphology of adsorbed overlayers.

In the reciprocal space, the action of the HRLEED is described by a rotation of the Ewald sphere around one point on the (0,0)-lattice rod, Figure 16. Thus the wave vector k of those electrons reaching the channeltron (α=7.5°) crosses the lattice rods one after another, i.e. the LEED pattern moves across the channeltron aperture. This shift Δk_l is proportional to the change of the deflection voltages:

$$\Delta U = c \cdot \Delta k_l \qquad (27)$$

The constant c is called deflection sensitivity of the HRLEED system. The resolution of the HRLEED is given by the full width at half maximum of a diffraction spot. It is measured by the change of the deflection voltages ΔU_0 during a scan of the spot and can be conversed to a width Δk_l in the reciprocal lattice by means of the deflection sensitivity. The corresponding angular resolution then amounts to

$$\Delta\alpha = \hbar\Delta k_{\parallel} / \sqrt{2mE} = \hbar\Delta U_o / c\sqrt{2mE}, \qquad (28)$$

where E is electron energy, m the electron mass. The resolution can also be specified in terms of the transfer width of the instrument, the characteristic of the maximum length of structural features at the surface which can still be resolved in the profile of the diffraction spots,

$$t = \frac{a}{r} = a\frac{\Delta U_1}{\Delta U_o}, \qquad (29)$$

where a is the lattice constant, ΔU_0 is the half width of a spot and ΔU_1 the difference of deflection voltages for two basic reflexes. Our HRLEED system has a maximum resolving power of 1003 Å, measured using a Si(111) crystal.

The Cu(100), (110) and (111) single crystal surfaces were cleaned prior to each iron deposition by several cycles of Ar ion sputtering and subsequent annealing at 1073 K for

Figure 16. Action of the octopole deflection unit in the reciprocal lattice. K_i denotes the wave vector of the primary electrons. k_f is the wave vector of those electrons detected by the channeltron. The angle between k_i and k_f at the surface α is kept to a constant 7.5°.

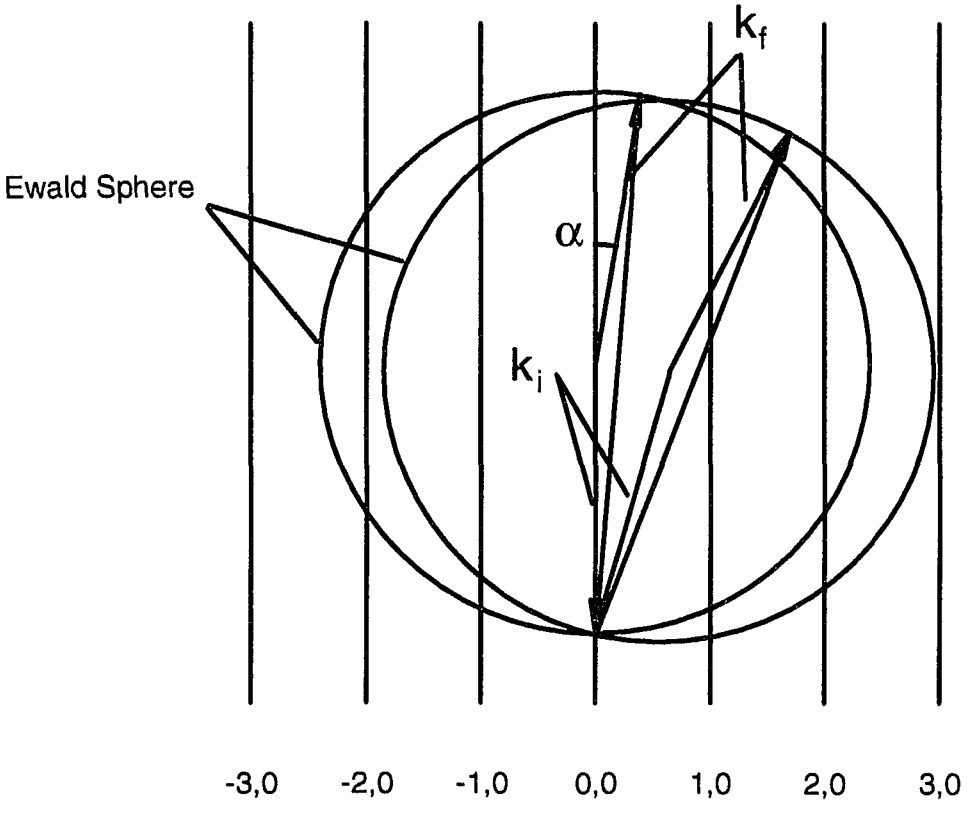

several minutes. Auger spectroscopy and conventional LEED are used to monitor the cleanness of the surface. The cleaning process is repeated until no trace of impurity is in the Auger spectrum and sharp LEED pattern is observed on the screen. The iron coverage is determined by the relative intensities of the 651 eV (Fe) and 920 eV (Cu) Auger peaks, as well as the low energy peaks (Fe: 47 eV, Cu: 105 eV). Auger spectra are also collected before and after the spot profile measurements in which the sample is heated from 173 K to 673 K. Most of the information can be obtained from the [00] spot, although some other higher index spots are recorded as a test of consistency. The data are collected and stored in the computer for later analysis.

CHAPTER 4

EXPERIMENTAL DESCRIPTION

4.1 Description of the Measurement

The spot profiles of clean Cu surfaces for all four samples (two (100)'s, one (110) and one (111)) were measured at various temperatures. Figure 17 shows a typical diffraction spot from a clean Cu surface. Fe is deposited at three different substrate temperatures: 173 K, 303 K and 473 K. The iron coverages on the Cu surfaces are 1 ML, 3 ML and 6 ML for each substrate temperature. For all the possible combinations of coverage and deposition temperature, we measure the spot profiles as a function of temperature from 173 K to 673 K. The energy dependence of the spot profiles is also investigated at various temperatures after the deposition.

4.2 Measurements on Clean Cu Surfaces

For each of the three types of Cu surfaces, we thoroughly clean the surface until no trace of impurity in the AES spectrum and clear sharp LEED images are observed before measuring the spot profiles. The sample is cooled to below 170K using LN_2 . By adjusting the LN_2 flow and the heater current, we are able to control the sample temperature within ±5K while measuring the spot profile. The spot profiles are recorded at interval of roughly 35K as the sample temperature rises from 170K up to 673K. The spot intensity and the FWHM are obtained by fitting the measured spot profile to a two-dimensional Gaussian function.

Figure 17. A Typical Spot from Clean Cu Surface

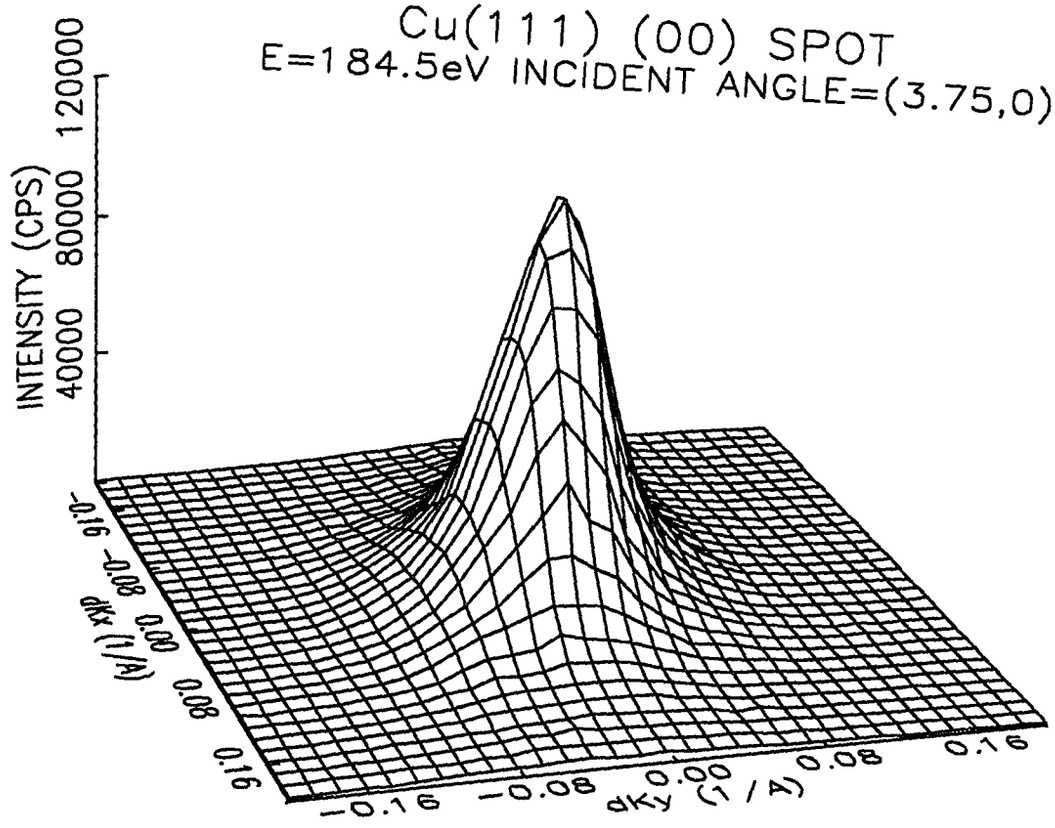

4.2.1 Cu(100)

The (00) diffraction spot is measured as function of sample temperature. The intensity of the spot decreases exponentially as the sample temperature increases, following the Debye theory, Figure 18. The shape of the spot keeps unchanged throughout the measurement, the FWHM increases slightly with temperature as expected, Figure 19. The coherence length of the Cu(100) sample surface is about 180 Å, computed from the FWHM of the spot profile. Figure 20 is a 2-dimensional spot profile of clean Cu(100) surface measured at 173K.

4.2.2 Cu(110)

The (00) diffraction spot is measured as function of sample temperature. The intensity of the spot decreases exponentially as the sample temperature increases, following the Debye theory, Figure 21. The shape of the spot keeps unchanged throughout the measurement, the FWHM increases slightly with the temperature as expected, Figure 22. The coherence length of the Cu(110) sample surface is about 180 Å, computed from the FWHM of the spot profile. Figure 23 is a 2-dimensional spot profile of clean Cu(110) surface measured at 173K.

4.2.3 Cu(111)

The (00) diffraction spot is measured as function of sample temperature. The intensity of the spot decreases exponentially as the sample temperature increases, following the Debye theory, Figure 24. The shape of the spot keeps unchanged throughout the measurement, the FWHM increases slightly with the temperature as expected, Figure 25. The coherence length of the Cu(111) sample surface is about 180 Å, computed from the FWHM of the spot profile. Figure 26 is a 2-dimensional spot profile of clean Cu(111) surface measured at 173K.

Figure 18. Spot intensity vs. temperature of a clean Cu(100) sample.

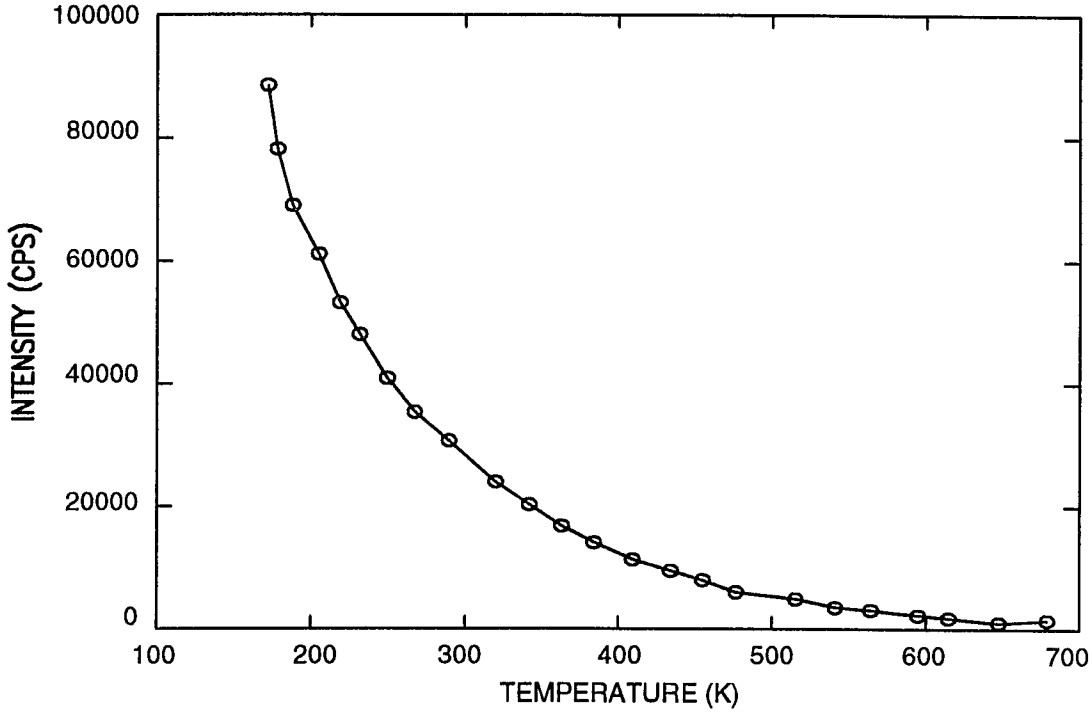

Figure 19. Spot FWHM vs. temperature of a clean Cu(100) sample.

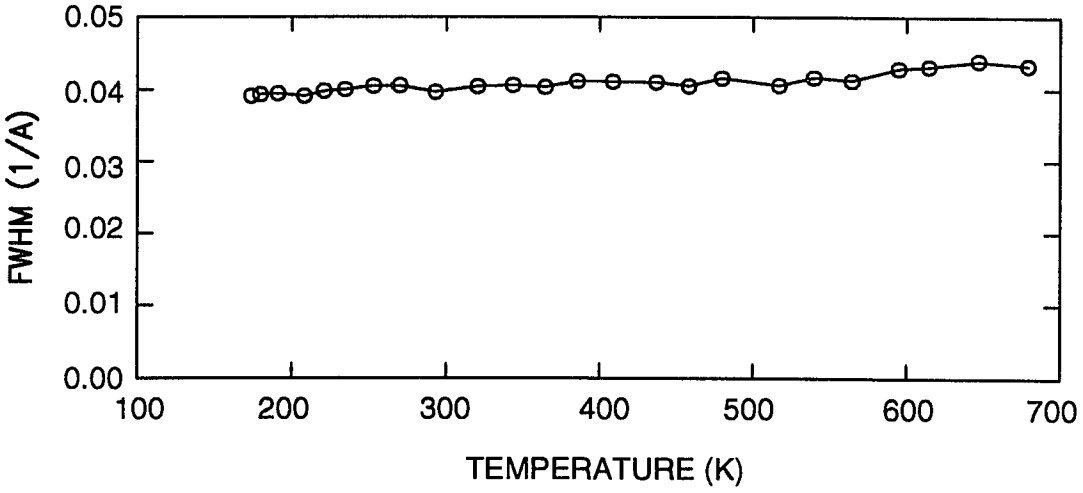

Figure 20. A 2-dimensional spot profile of clean Cu(100) surface measured at 173K.

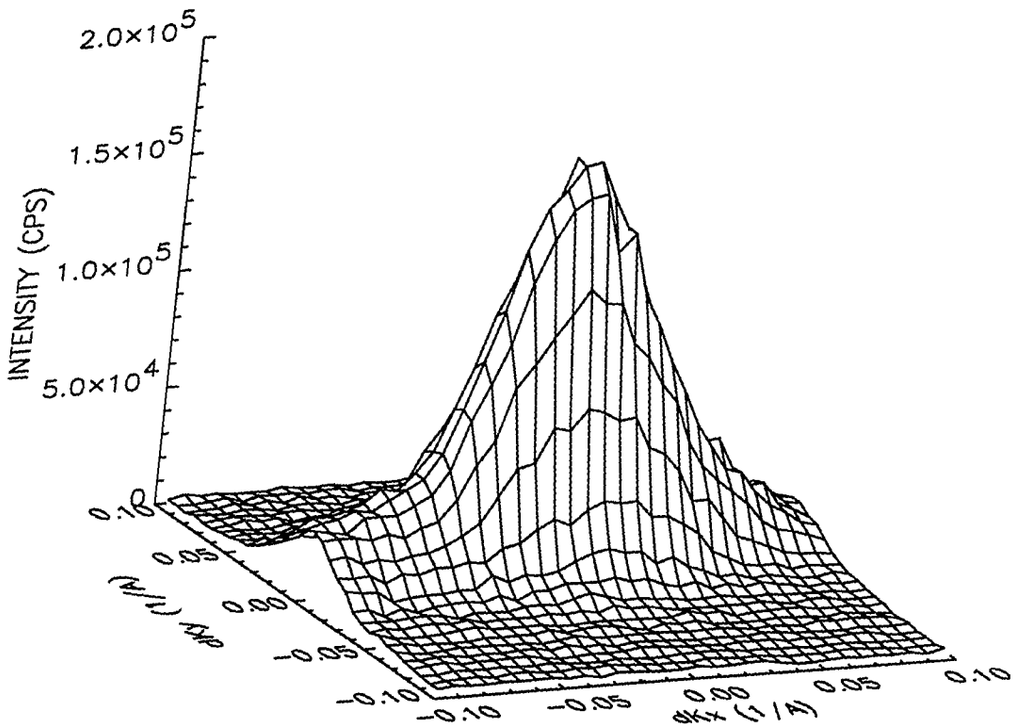

Figure 21. Spot intensity vs. temperature of a clean Cu(110) sample.

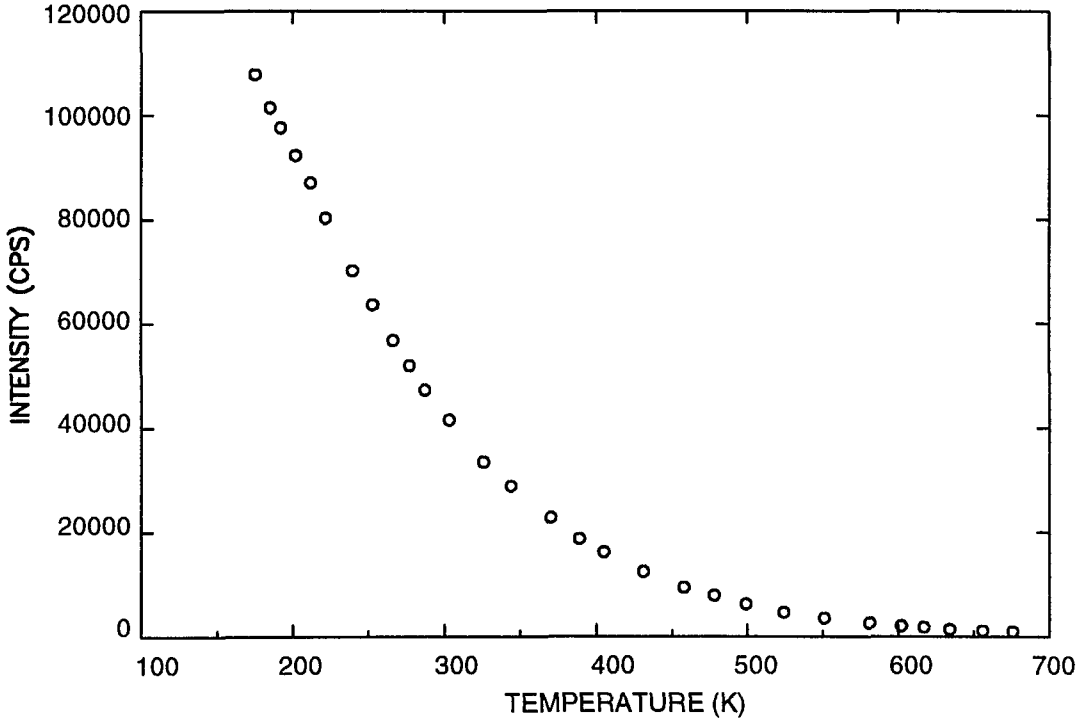

Figure 22. Spot FWHM vs. temperature of a clean Cu(110) sample.

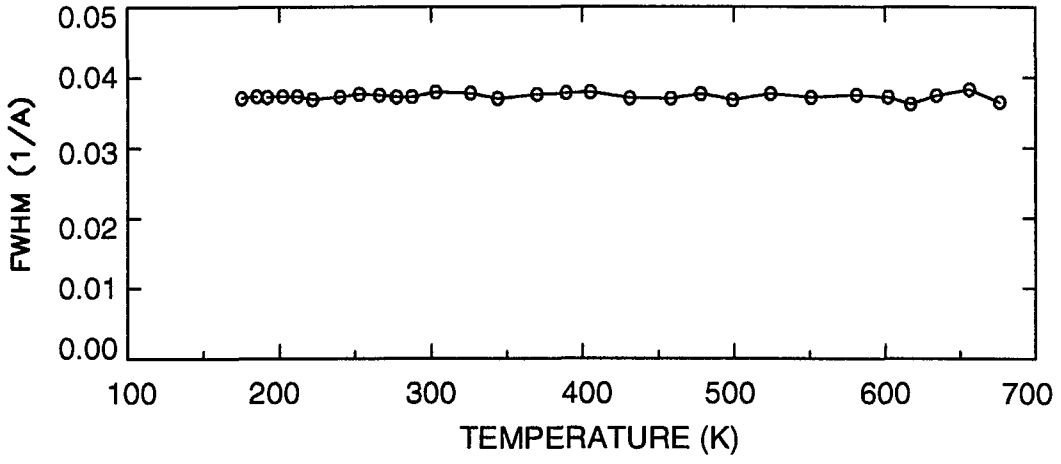

Figure 23. A 2-dimensional spot profile of clean Cu(110) surface seasured at 173K.

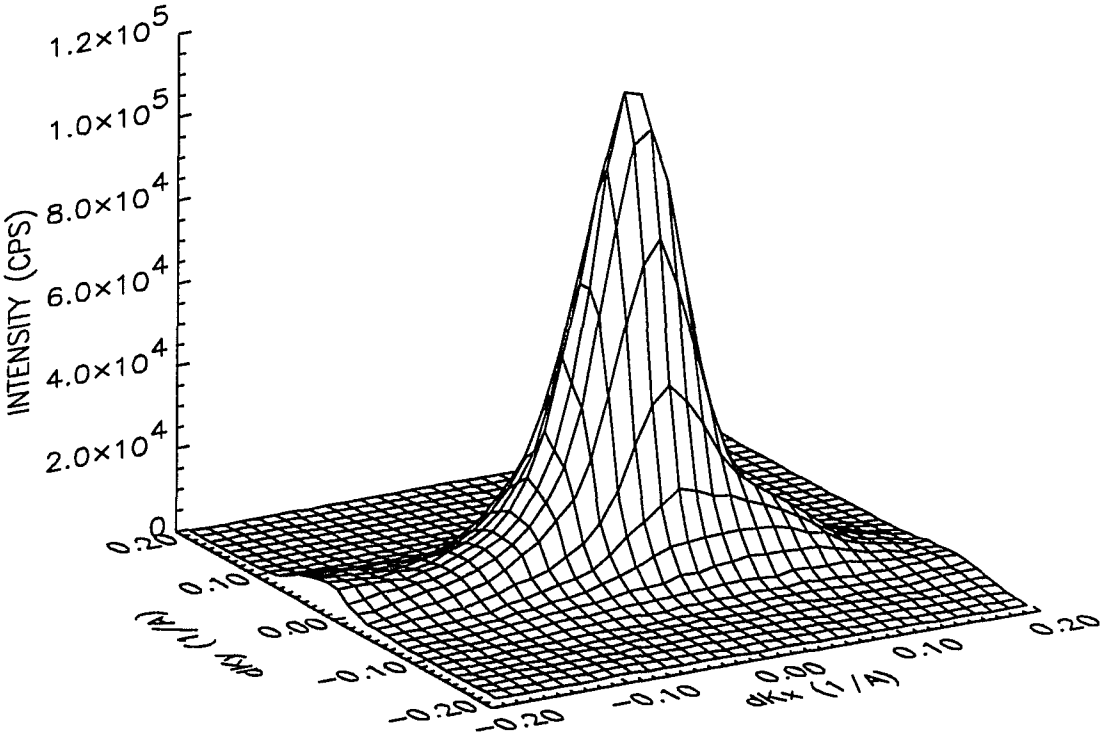

Figure 24. Spot intensity vs. temperature of a clean Cu(111) sample.

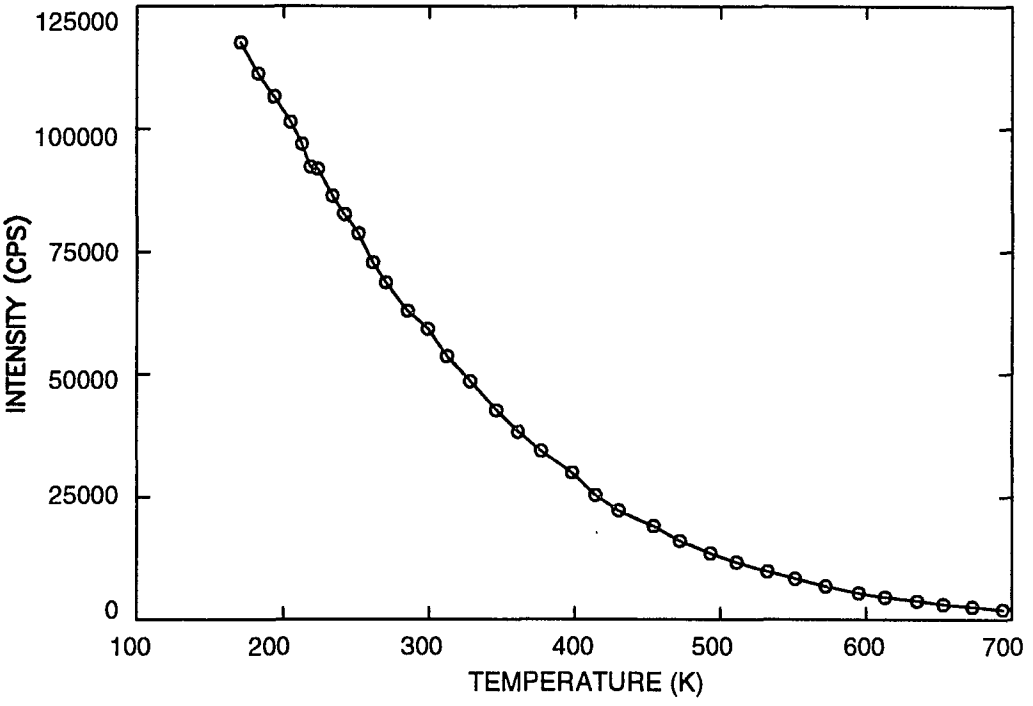

Figure 25. Spot FWHM vs. temperature of a clean Cu(111) sample.

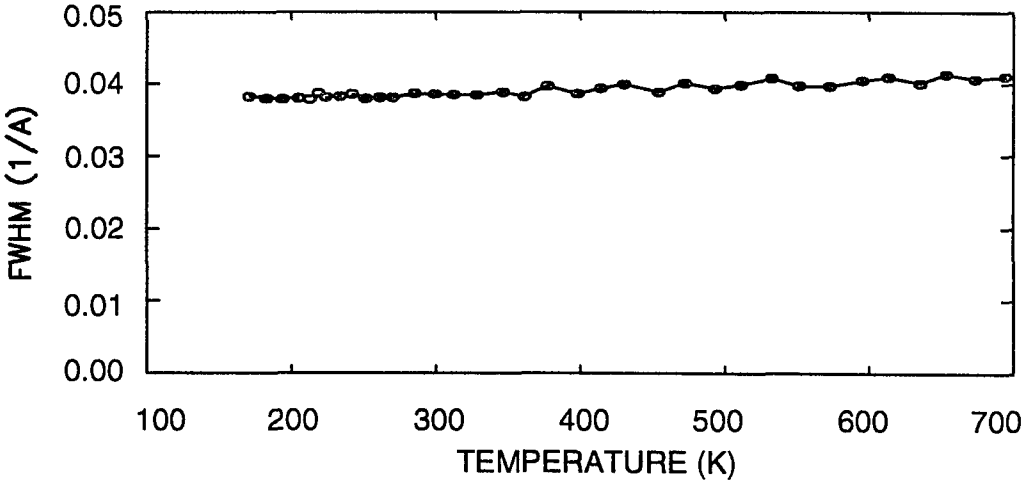

Figure 26. A 2-dimensional spot profile of clean Cu(111) surface measured at 173K.

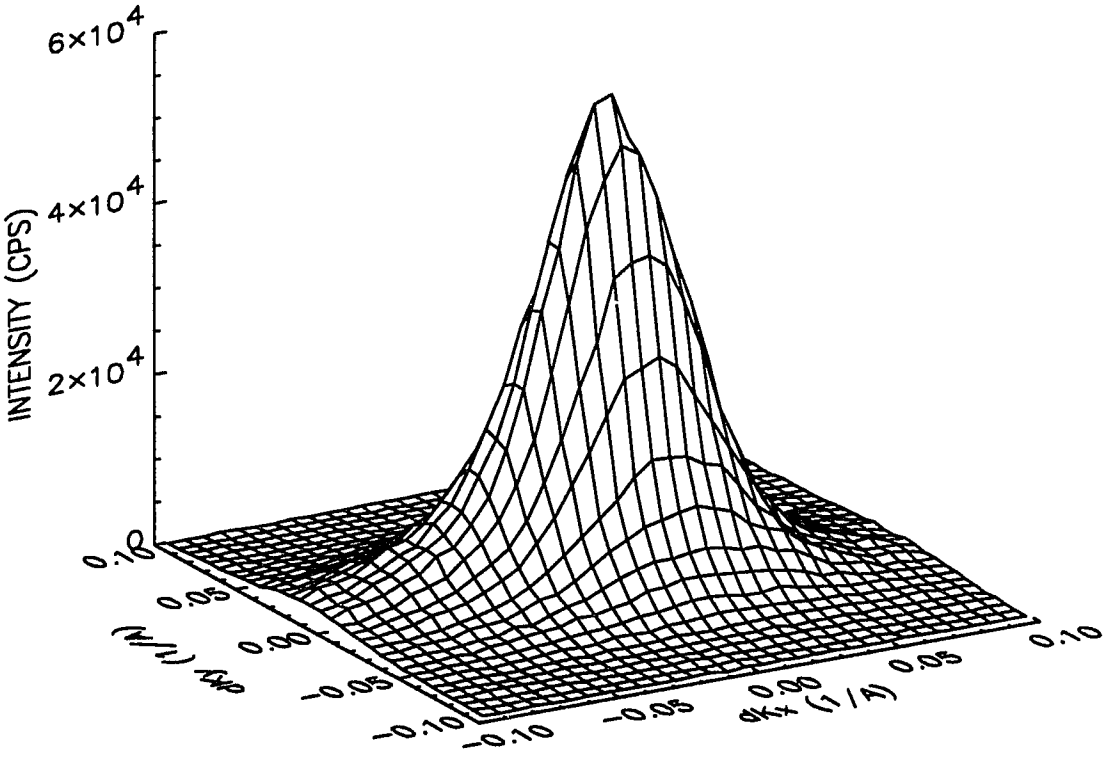

4.3 Temperature Dependence Measurements of Iron on Cu Surfaces

Iron is deposited on the three types of Cu surfaces. Before each deposition, we go through the same cleaning and annealing procedures monitored by the AES spectrum and the LEED image until a clean and smooth surface is obtained. We then set the sample to the desired temperature (170K, 300K and 473K) and deposit the iron. The AES spectrum is measured after the deposition to determine the thickness of the iron. Cu(100) is the most scientifically important surface that had been studied the most. We measure the spot profiles of 1ML, 3ML and 6ML iron deposited on Cu(100). The spot profiles for those deposited on Cu(110) and Cu(111) are too weak to measure. The weak signals of the LEED spots is an indication that the growths on the Cu(110) and Cu(111) are not as good as the one on the Cu(100). In order to get a good statistic for them, the data collection process takes very long time, making the data meaningless due to the possible contamination of the surface.

4.3.1 Cu(100)

1ML Fe deposited at high temperature

We deposit 1 monolayer Fe on Cu(100) at 473K and measure the LEED spot profiles at various temperatures. The spot is bright and sharp, indicating a smooth growth under such growth condition. The spot intensity and the width change with the temperature in a fashion similar to the clean Cu(100) (Figure 27 and Figure 28). Figure 29 shows the changes of the AES spectra of 1ML Fe/Cu(100) deposited at 473K.

1ML Fe deposited on Cu(100) at room temperature

We deposit 1 monolayer Fe on Cu(100) at 300K and measure the LEED spot profiles at various temperatures. The spot intensity is weaker than it is deposited at high temperature. The spot is also broader (Figure 30). The intensity changes exponentially in

Figure 27. Spot intensity vs. temperature of 1ML/Cu(100) deposited at 473K

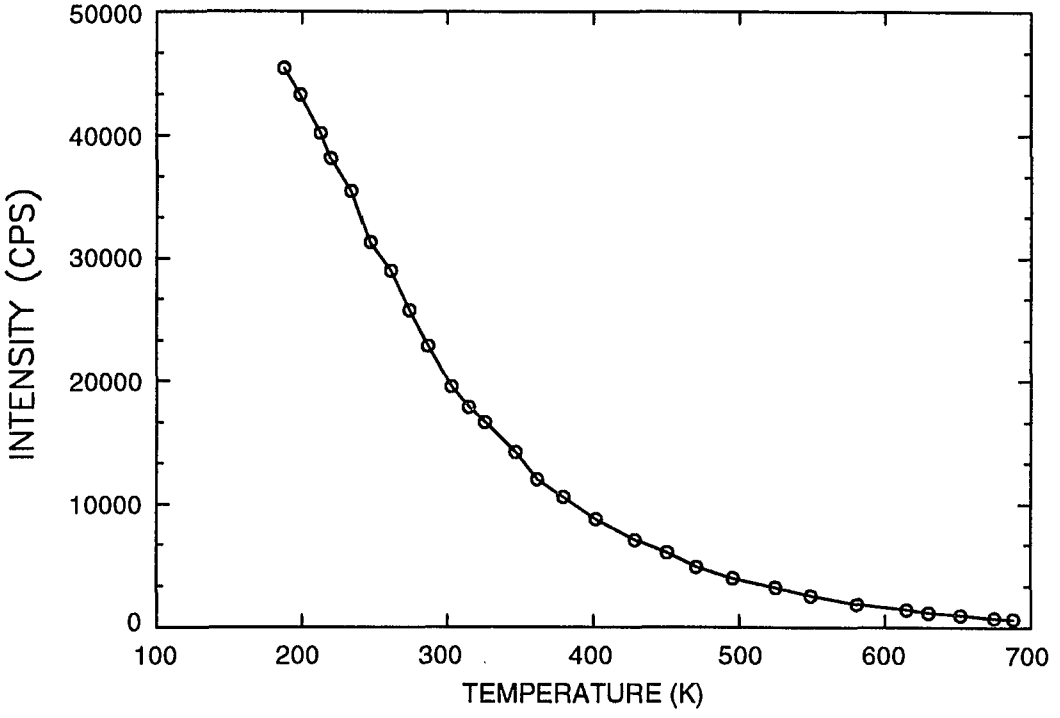

Figure 28. Spot FWHM vs. temperature of 1ML/Cu(100) deposited at 473K

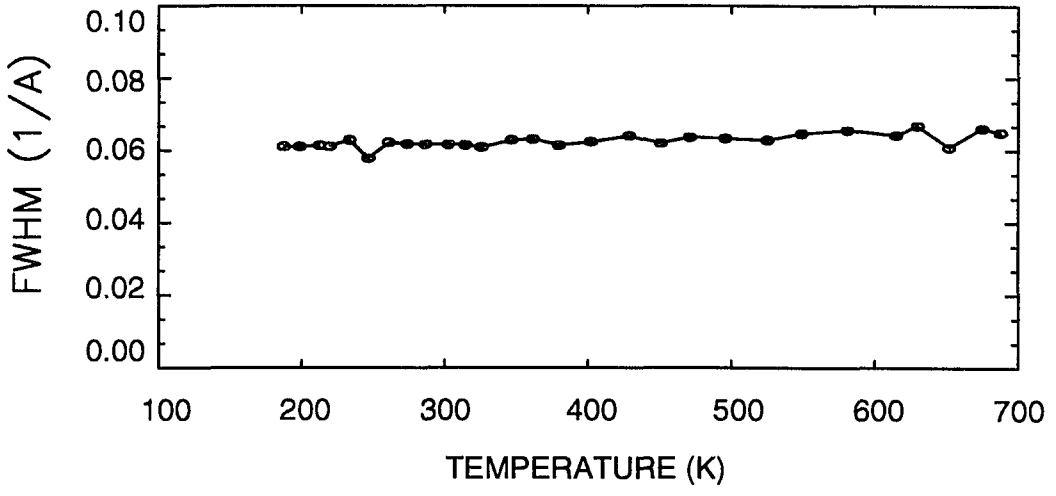

Figure 29. Changes of the AES spectra of 1ML Fe/Cu(100) deposited at 473K.

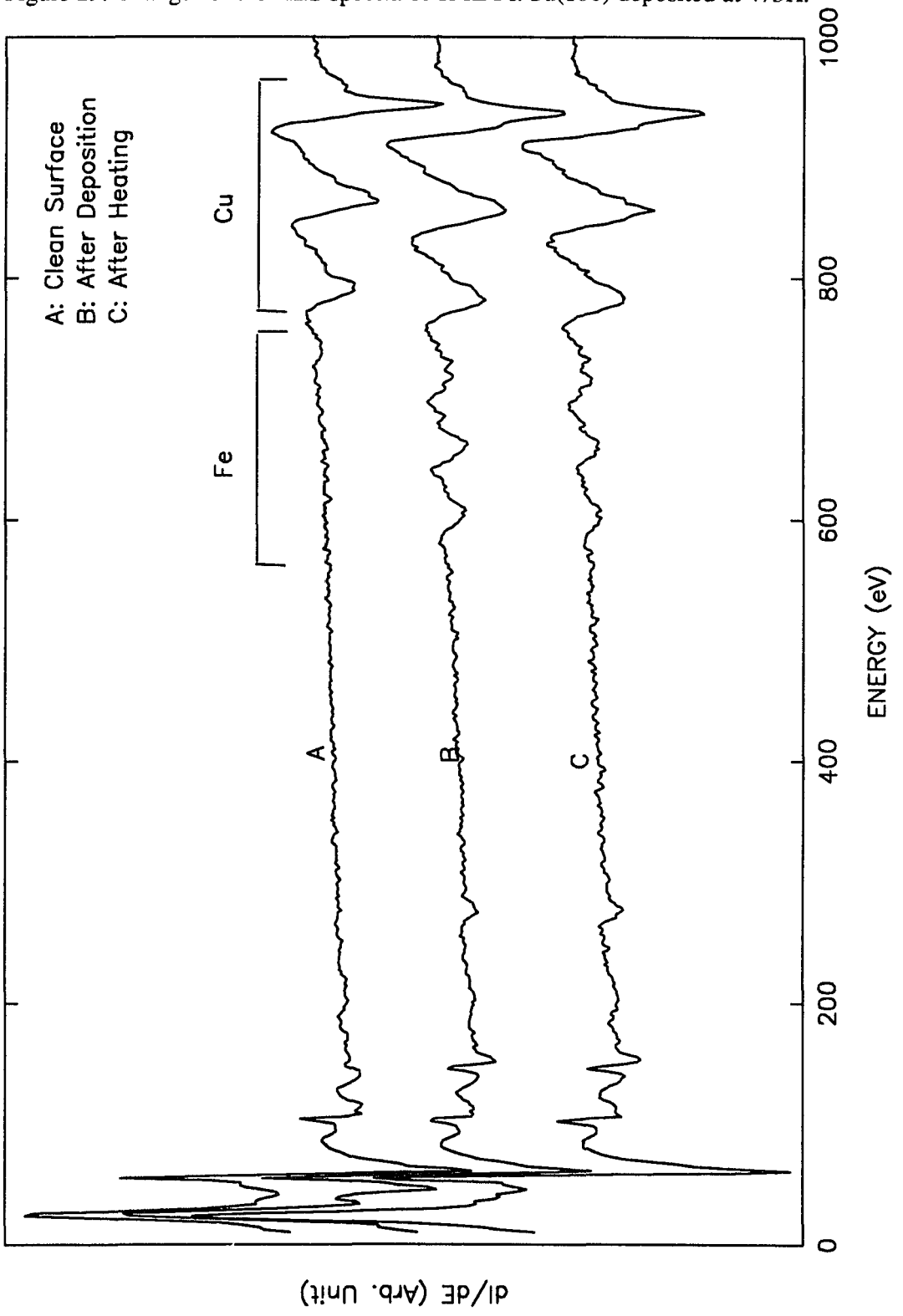

Figure 30. Spot profiles of clean Cu(100) and 1ML Fe/Cu(100) deposited at 300K.

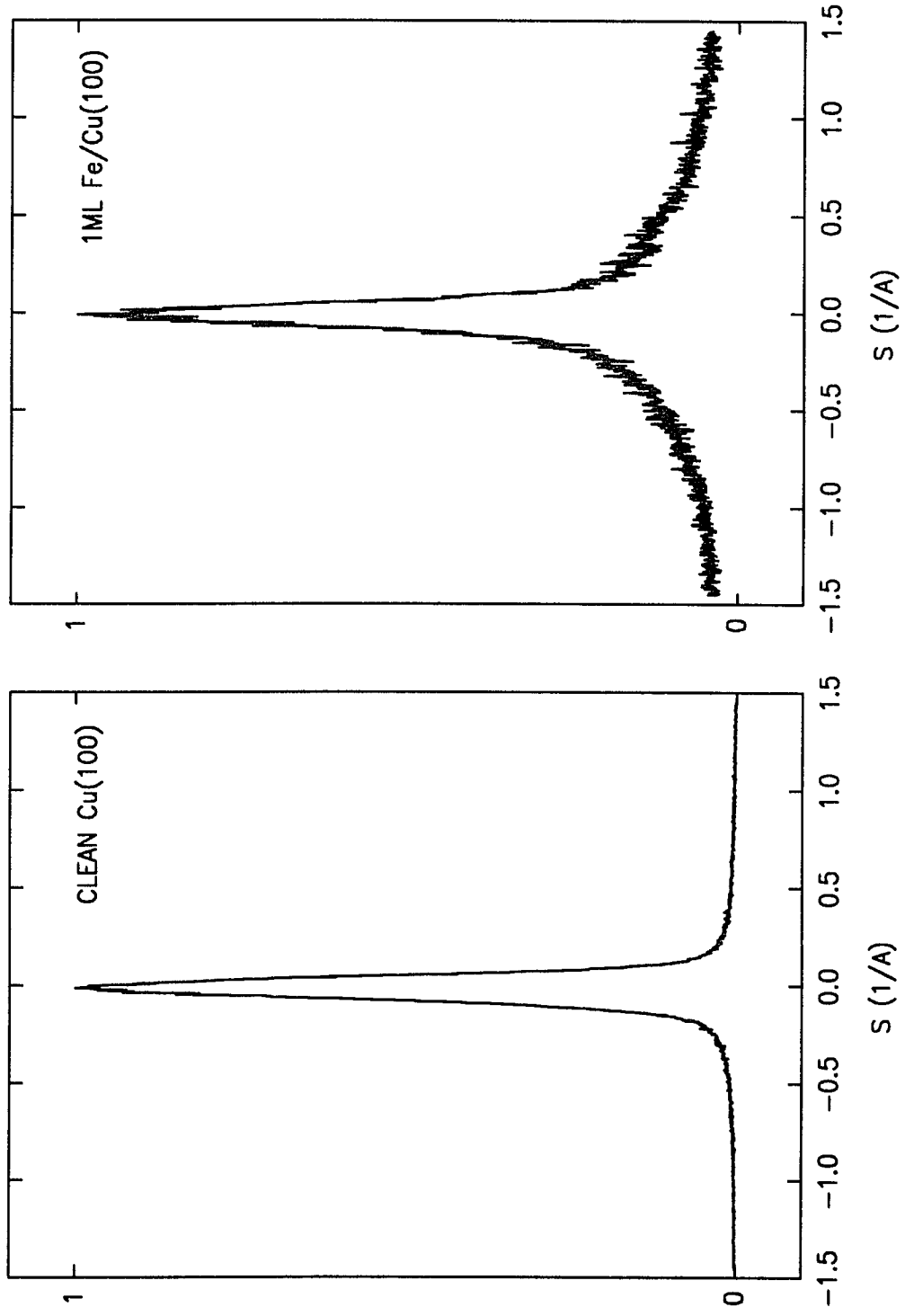

the low temperature region. At about 250K, it begins to differ from the exponential factor. The intensity bounces up a little at 550K and then decreases as the temperature continues to increase (Figure 31). The FWHM of the spots increases as the temperature rises. The increasing rate gets larger after the temperature reaches 500K (Figure 32). Figure 33 shows the changes of the AES spectra of 1ML/Cu(100) deposited at 300K.

1ML Fe deposited on Cu(100) at low temperature

We deposit 1 monolayer Fe on Cu(100) at 173K and measure the LEED spot profiles at various temperatures. The spot intensity is even weaker and the spot broader. We also see an abnormal change of the intensity around 300K (Figure 34 and Figure 35). Figure 36 shows the changes of the AES spectra of 1ML Fe/Cu(100) deposited at 173K.

3ML Fe on Cu(100) at high temperature

We deposit 3 monolayer Fe on Cu(100) at 473K and measure the LEED spot profiles at various temperatures. The result is similar to that of the clean Cu(100) and 1ML Fe deposited at high temperature (see Figure 37 and Figure 38). Figure 39 shows the changes of the AES spectra of 3ML Fe/Cu(100) deposited at 473K.

3ML Fe on Cu(100) at room temperature

We deposit 3 monolayer Fe on Cu(100) at 300K and measure the LEED spot profiles at various temperatures. The intensity decreases exponentially in the region below 500K. The intensity then goes up a little and falls back again after 550K (Figure 40). The spot FWHM increases steadily with the temperature (Figure 41). Figure 42 shows the changes of the AES spectra of 3ML Fe/Cu(100) deposited at 300K.

Figure 31. Spot intensity vs. temperature of 1ML/Cu(100) deposited at 300K

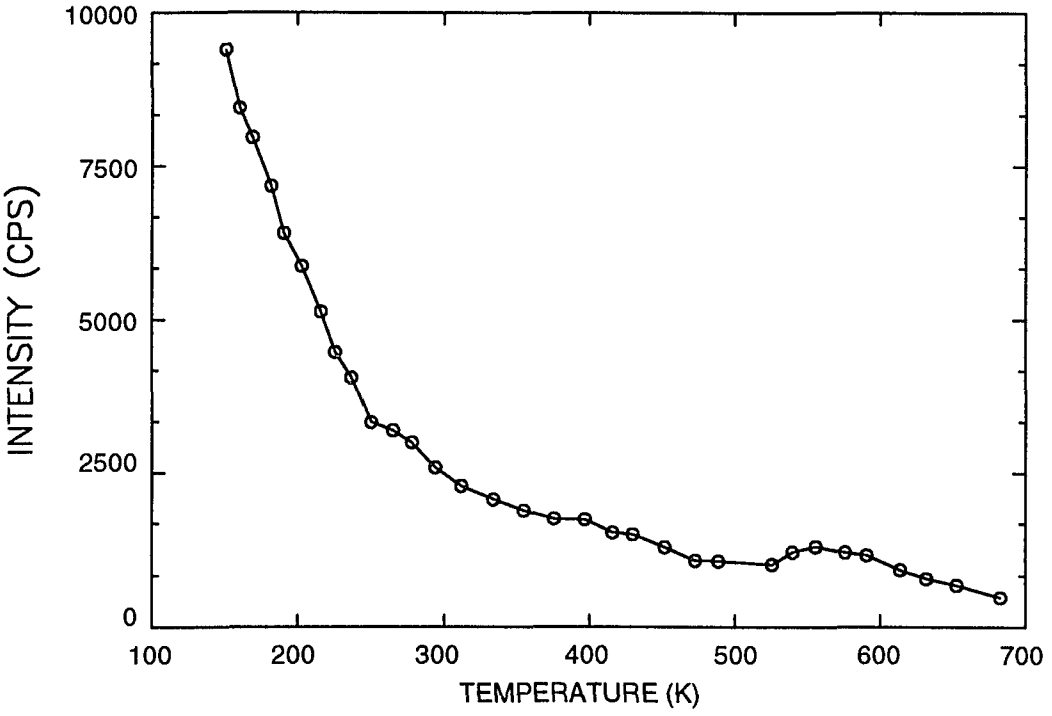

Figure 32. Spot FWHM vs. temperature of 1ML/Cu(100) deposited at 300K

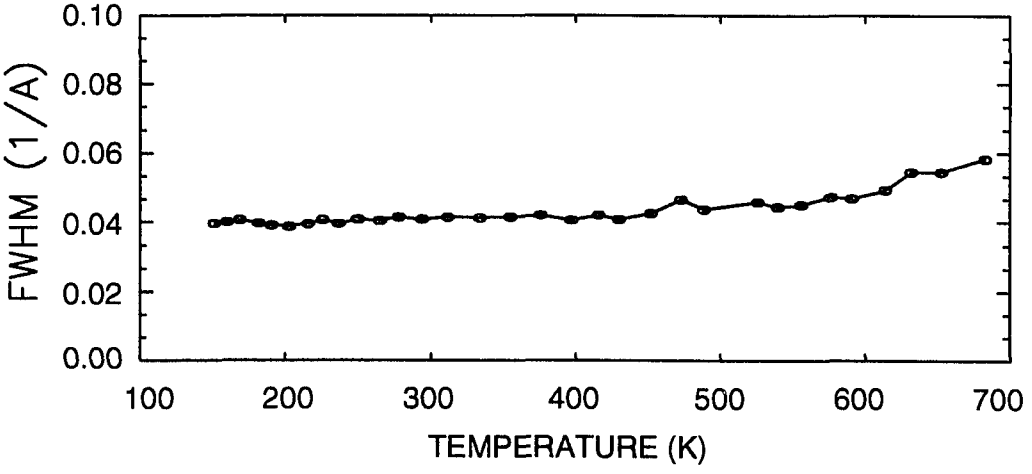

Figure 33. Changes of the AES spectra of 1ML Fe/Cu(100) deposited at 300K.

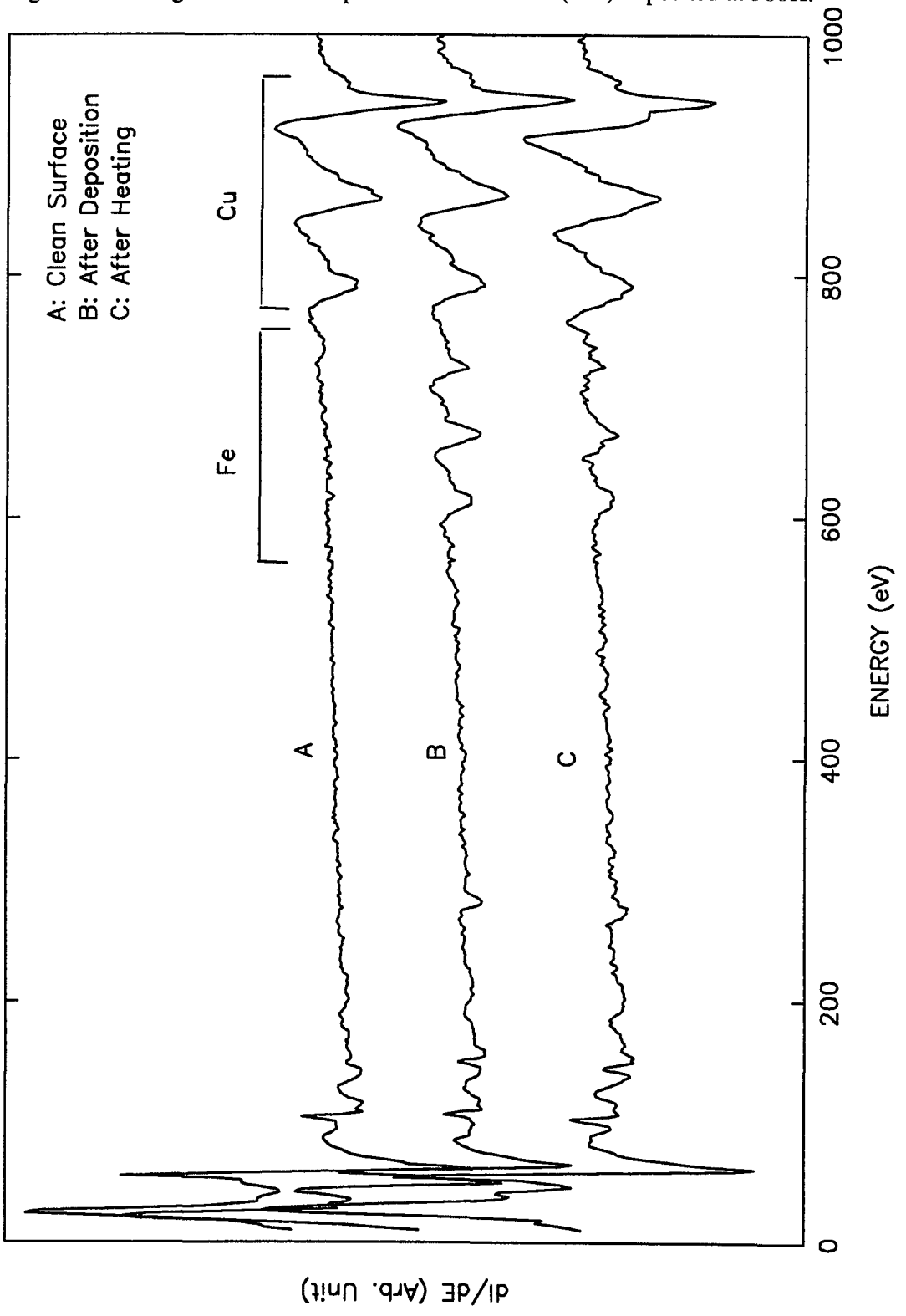

Figure 34. Spot intensity vs. temperature of 1ML/Cu(100) deposited at 173K

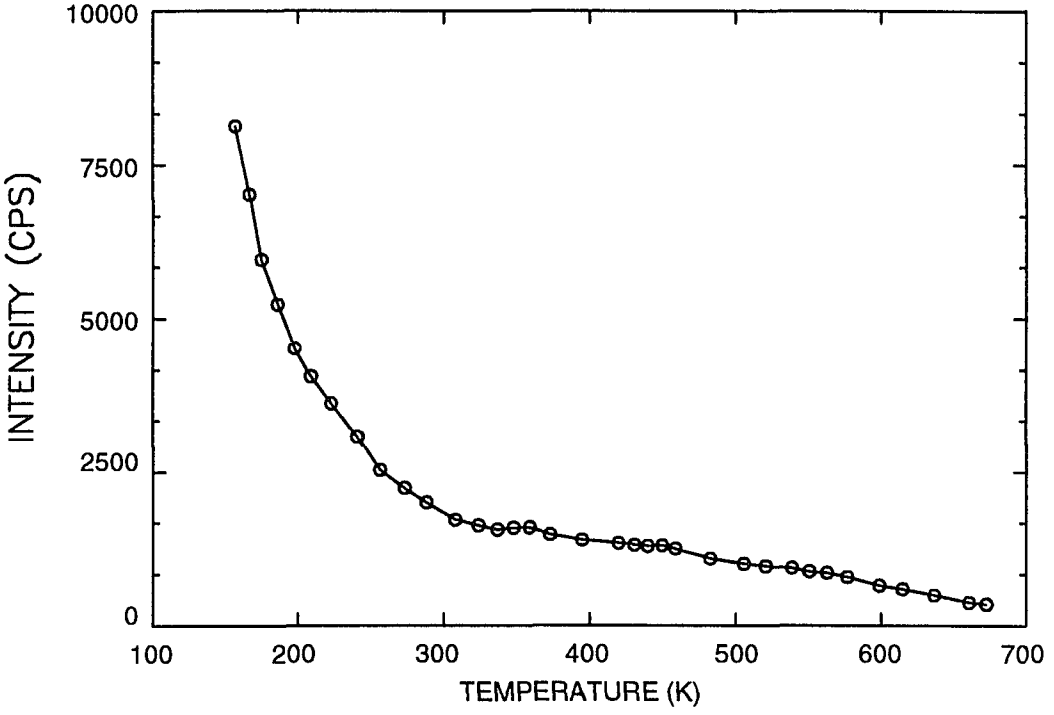

Figure 35. Spot FWHM vs. temperature of 1ML/Cu(100) deposited at 173K

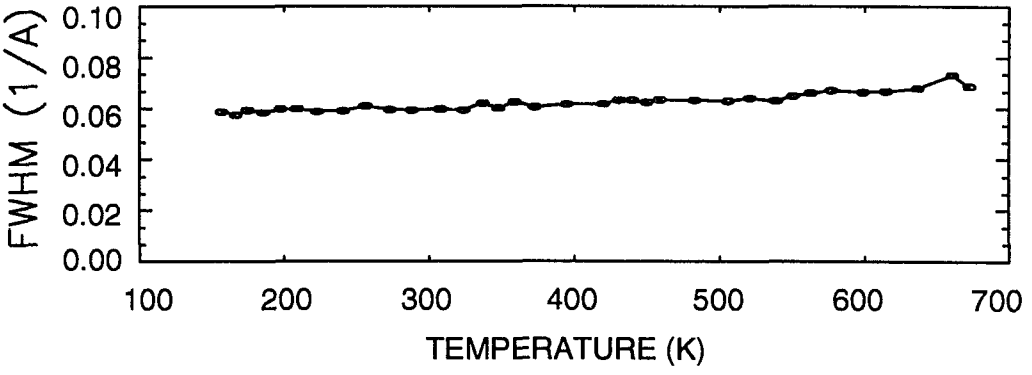

Figure 36. Changes of the AES spectra of 1ML Fe/Cu(100) deposited at 173K.

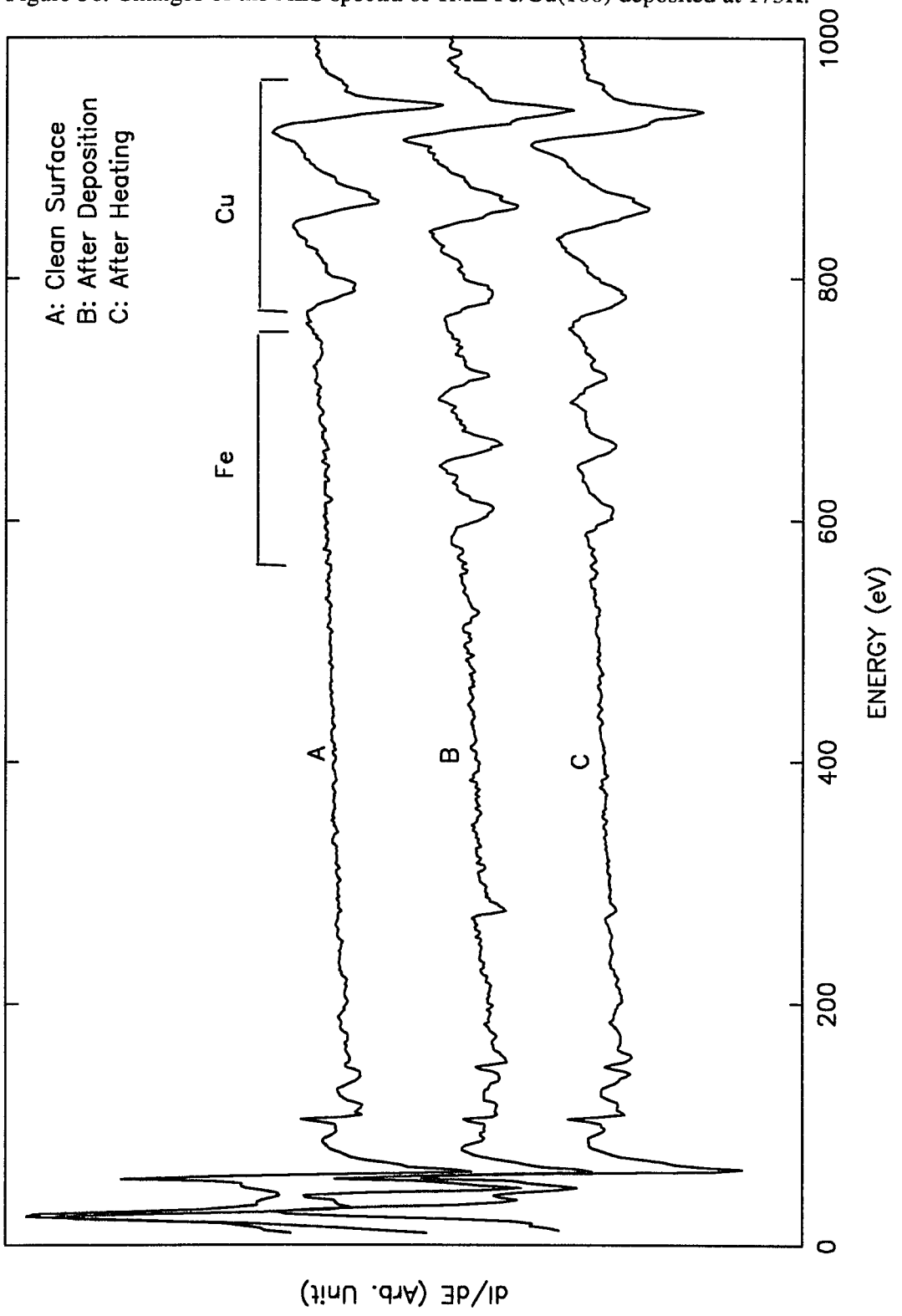

Figure 37. Spot intensity vs. temperature of 3ML/Cu(100) deposited at 473K

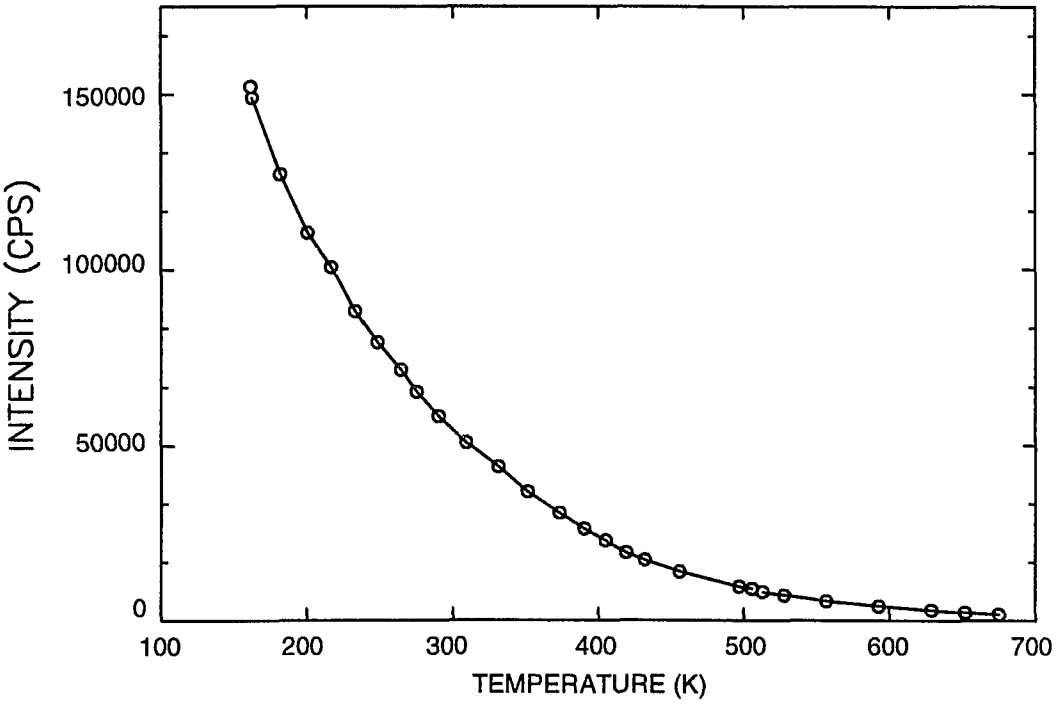

Figure 38. Spot FWHM vs. temperature of 3ML/Cu(100) deposited at 473K

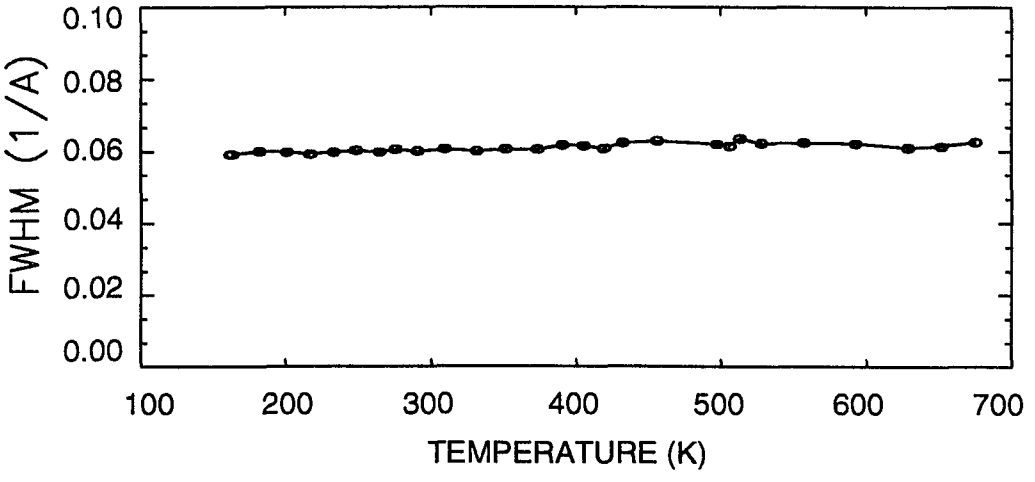

Figure 39. Changes of the AES spectra of 3ML Fe/Cu(100) deposited at 473K.

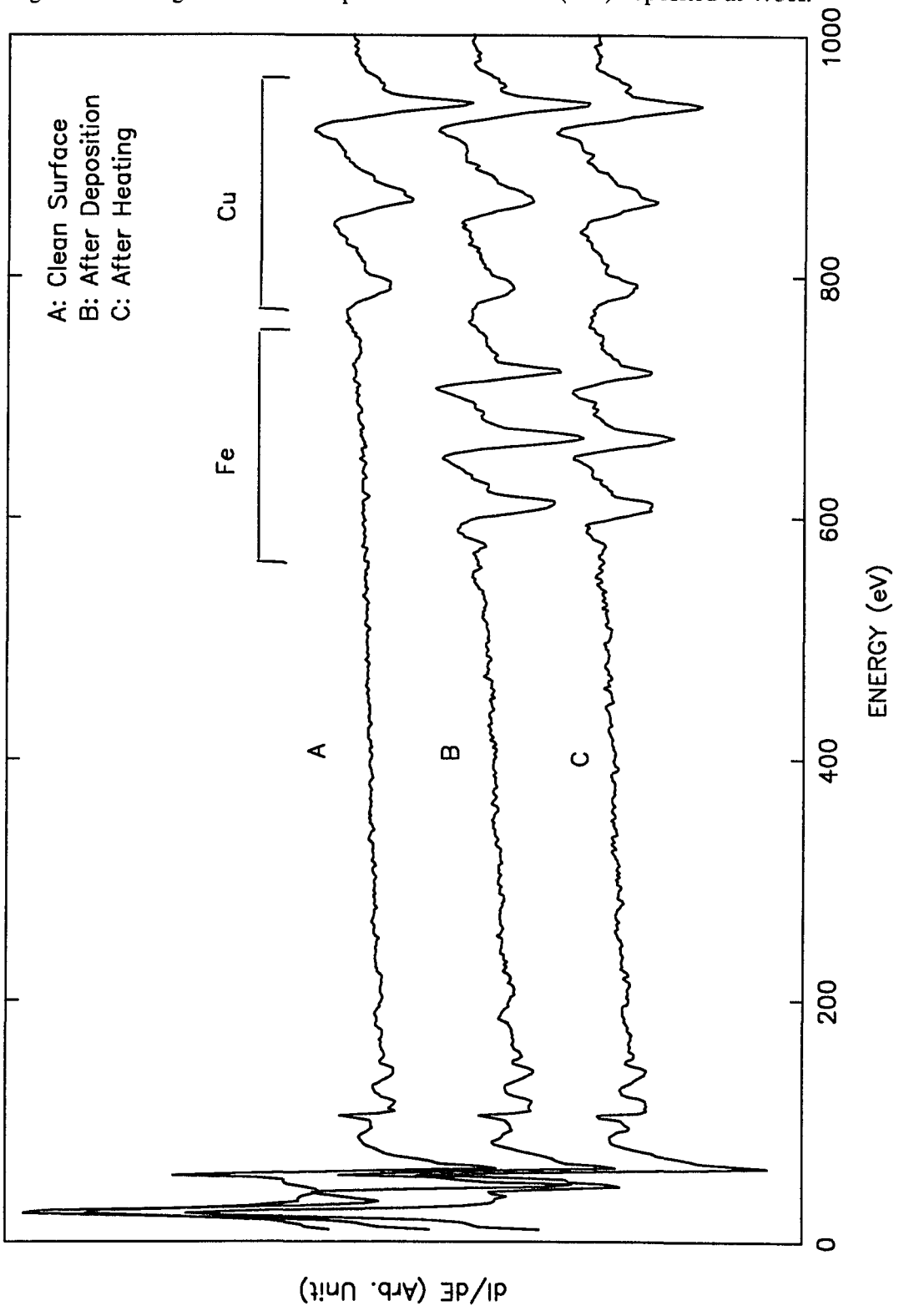

Figure 40. Spot intensity vs. temperature of 3ML/Cu(100) deposited at 300K

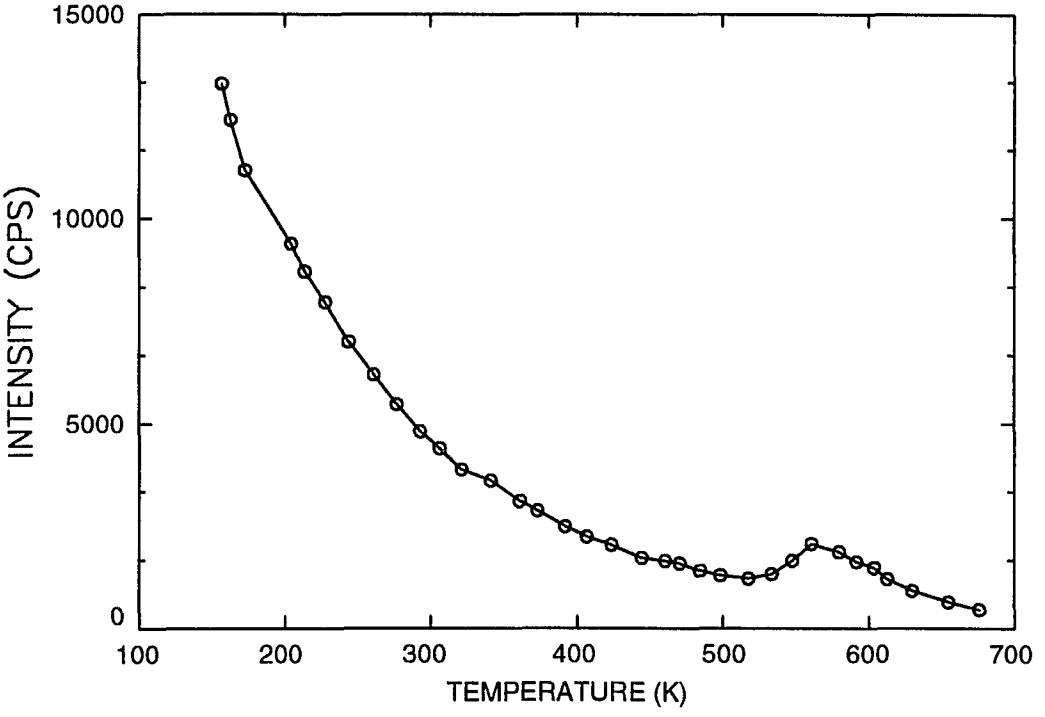

Figure 41. Spot FWHM vs. temperature of 3ML/Cu(100) deposited at 300K

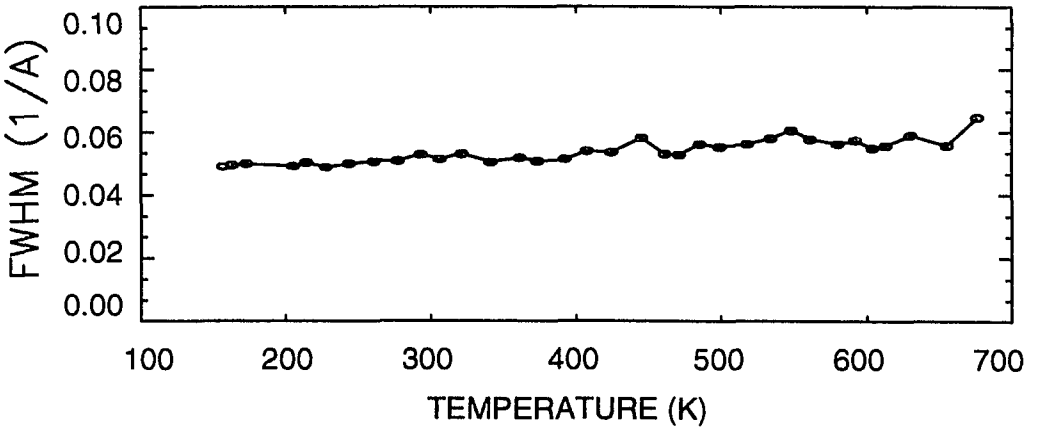

Figure 42. Changes of the AES spectra of 3ML Fe/Cu(100) deposited at 300K.

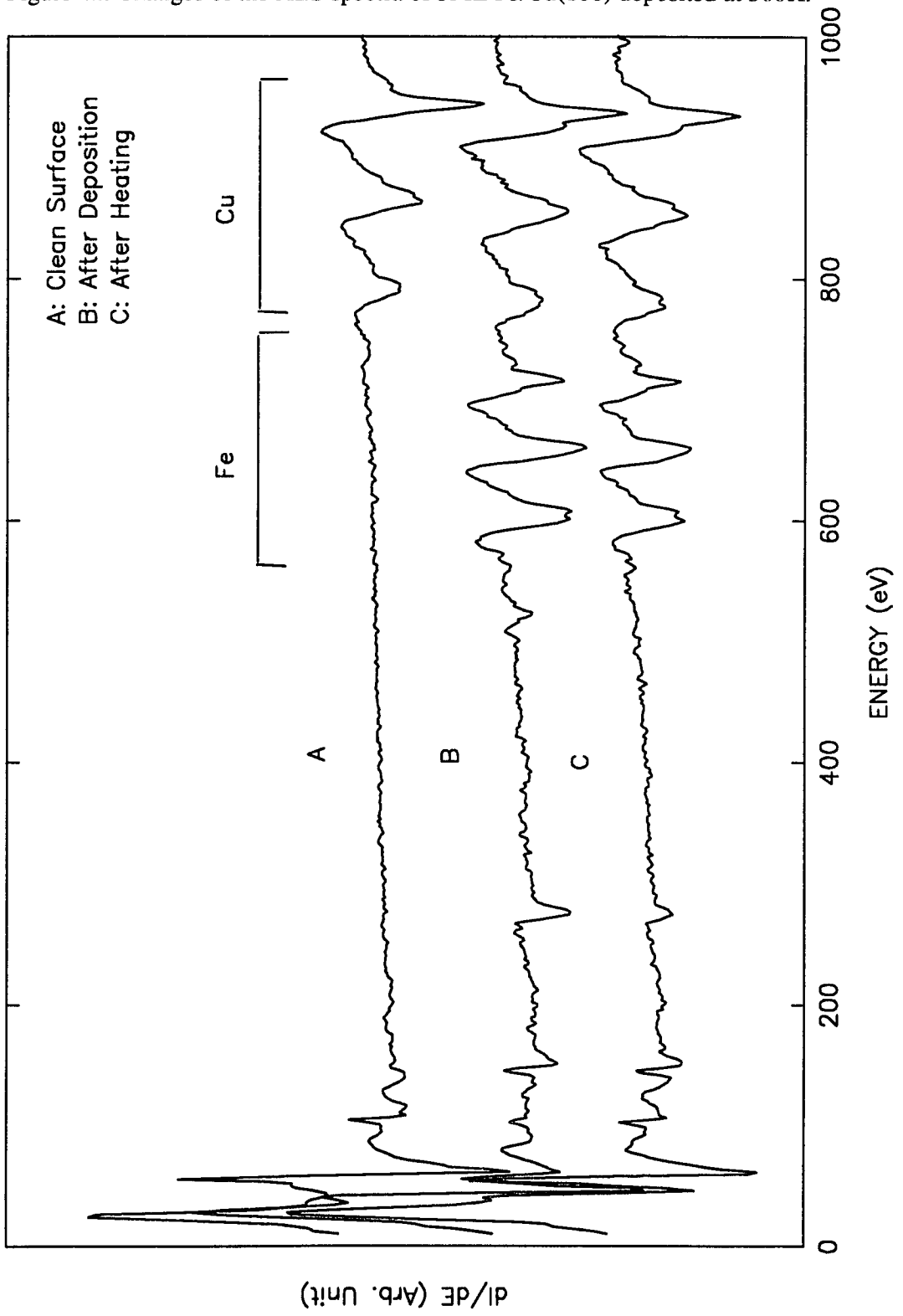

3ML Fe on Cu(100) deposited at low temperature

We deposit 3 monolayers Fe on Cu(100) at 173K and measure the LEED spot profiles at various temperatures. The intensity is much weaker. The intensity falls exponentially at first and begins to rise at 350K. It reaches the maximum at 550K and falls back again (Figure 43). The spot FWHM also shows some change in this abnormal temperature region (Figure 44). Figure 45 shows the changes of the AES spectra of 3ML Fe/Cu(100) deposited at 173K.

4.3.2 Cu(110)

1ML Fe on Cu(110) deposited at high temperature

We deposit 1 monolayer Fe on Cu(110) at 473K and measure the LEED spot profiles at various temperatures. The intensity deviates from the exponential behavior in two temperature regions: 250K and 550K (Figure 46). The spot FWHM also changes abruptly at these two temperatures (Figure 47). The spot is broad after the deposition. As the temperature rises, it becomes sharper. Figure 48 shows the changes of the AES spectra of 1ML Fe/Cu(100) deposited at 473K.

1ML Fe on Cu(110) at room temperature

We deposit 1 monolayer Fe on Cu(110) at 300K and measure the LEED spot profiles at various temperatures. The spot intensity shows an abnormal change beginning at 350K (Figure 49). The spot FWHM also makes a big change at 500K (Figure 50). Figure 51 shows the changes of the AES spectra of 1ML Fe/Cu(110) deposited at 300K.

1 ML Fe deposited on Cu(110) at low temperature

We deposit 1 monolayer Fe on Cu(110) at 173K. We can not get a clear and sharp

Figure 43. Spot intensity vs. temperature of 3ML/Cu(100) deposited at 173K

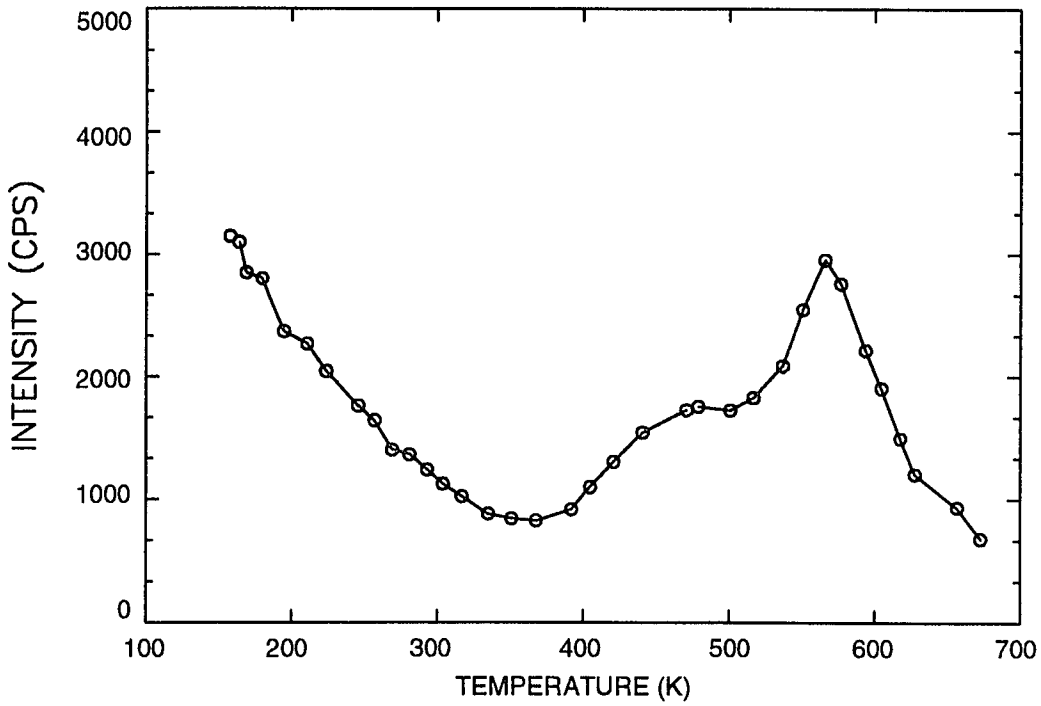

Figure 44. Spot FWHM vs. temperature of 3ML/Cu(100) deposited at 173K

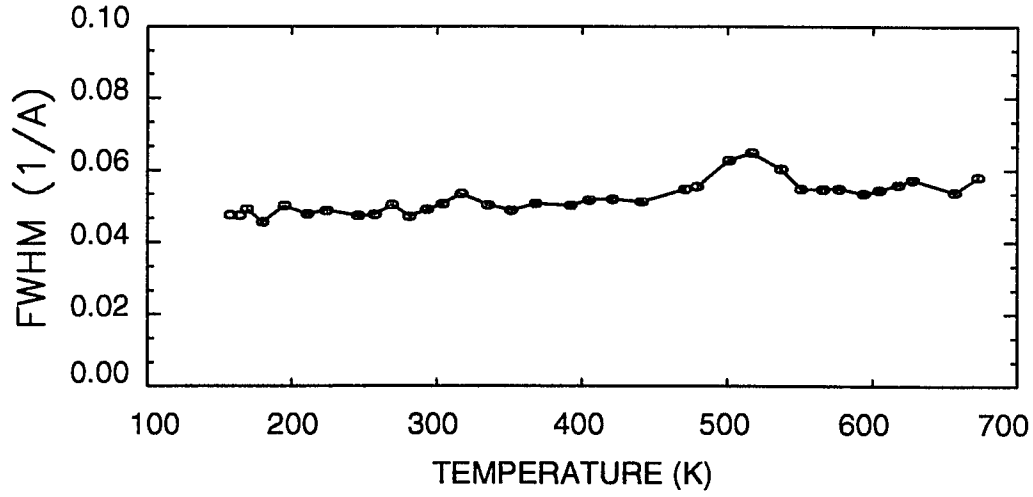

Figure 45. Changes of the AES spectra of 3ML Fe/Cu(100) deposited at 173K.

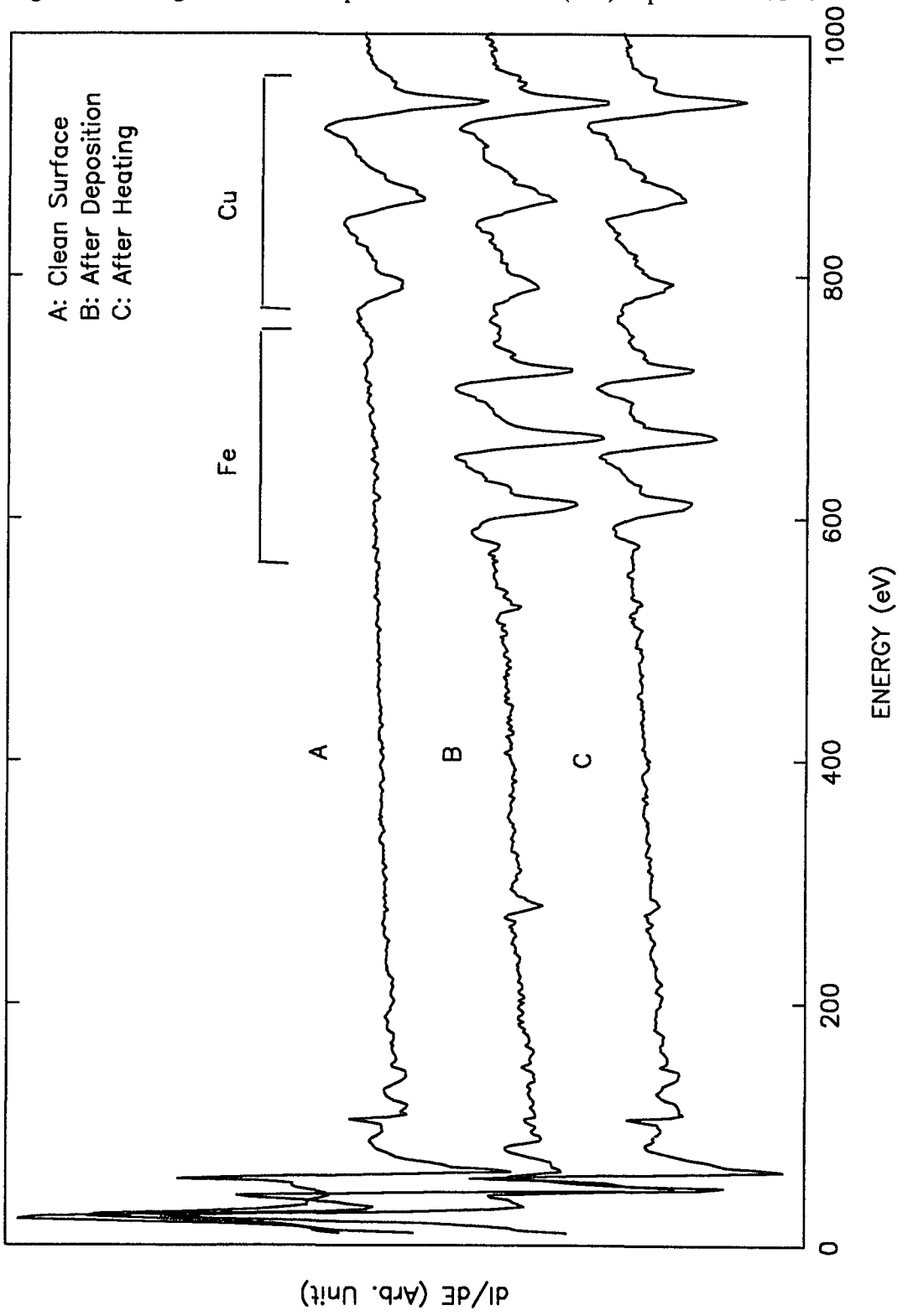

Figure 46. Spot intensity vs. temperature of 1ML/Cu(110) deposited at 473K

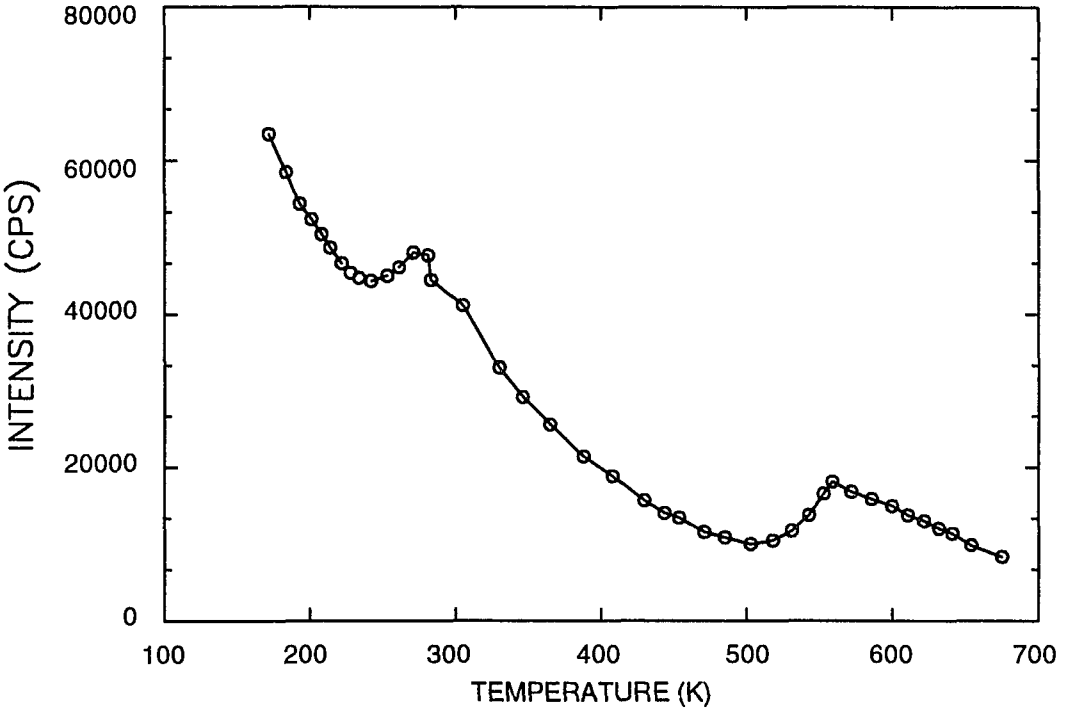

Figure 47. Spot FWHM vs. temperature of 1ML/Cu(110) deposited at 473K

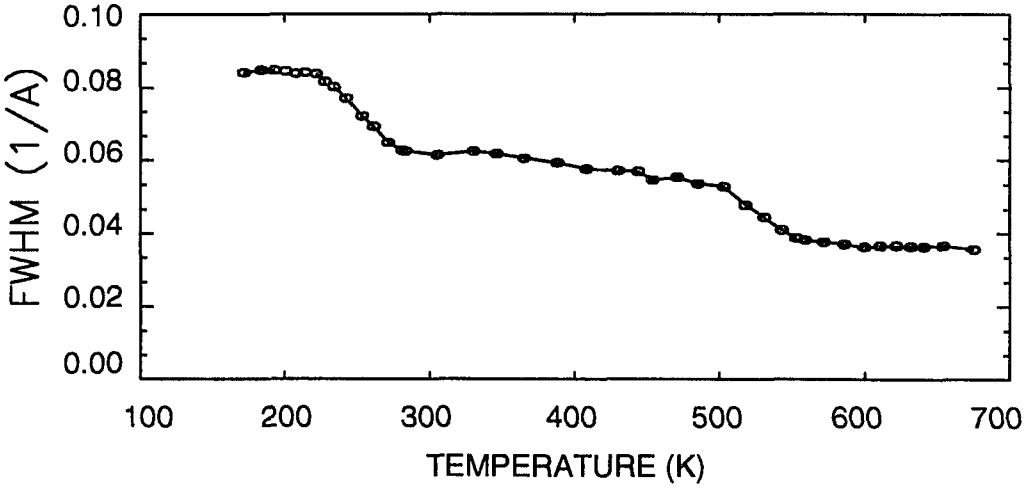

Figure 48. Changes of the AES spectra of 1ML Fe/Cu(110) deposited at 473K.

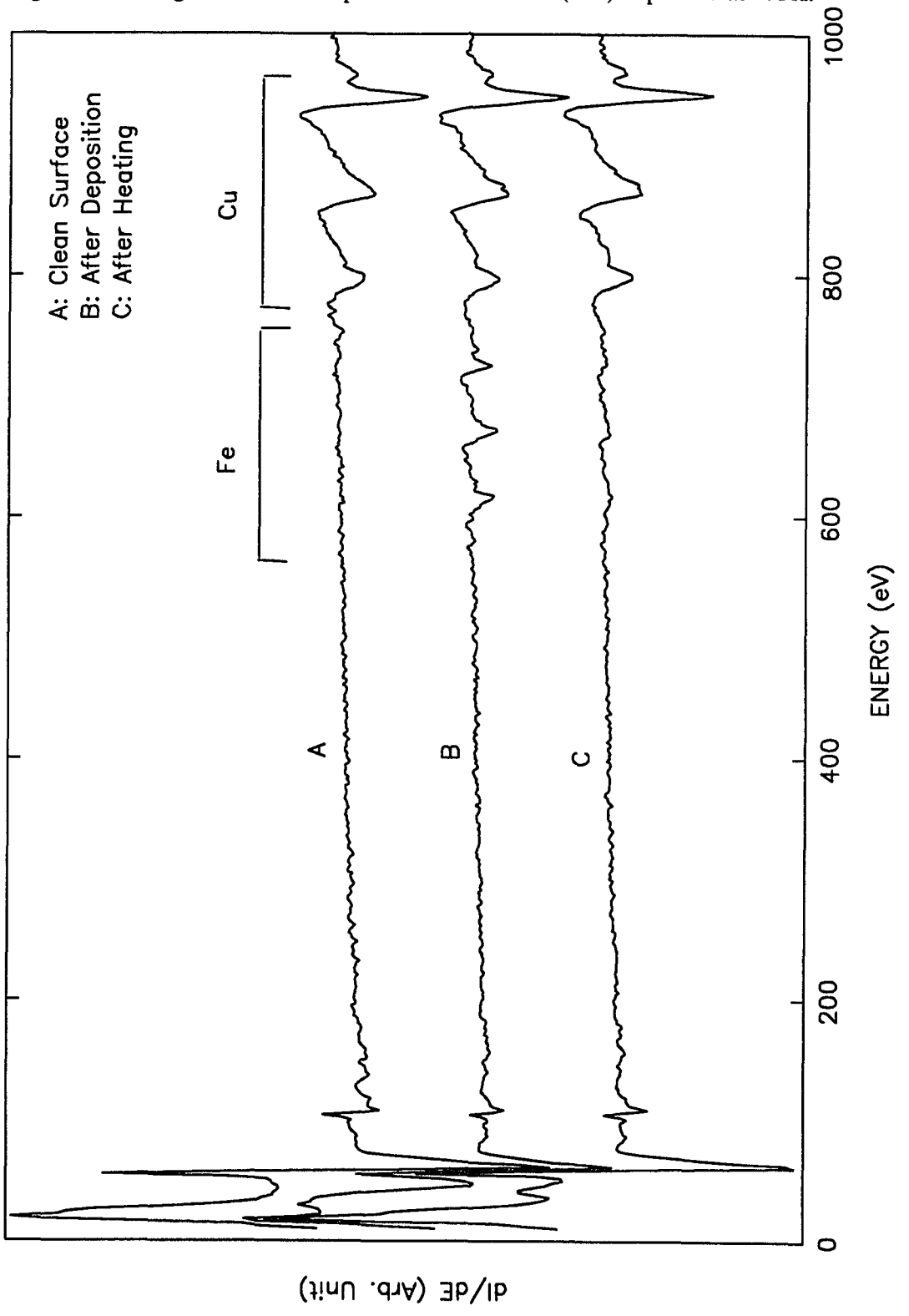

Figure 49. Spot intensity vs. temperature of 1ML/Cu(110) deposited at 300K

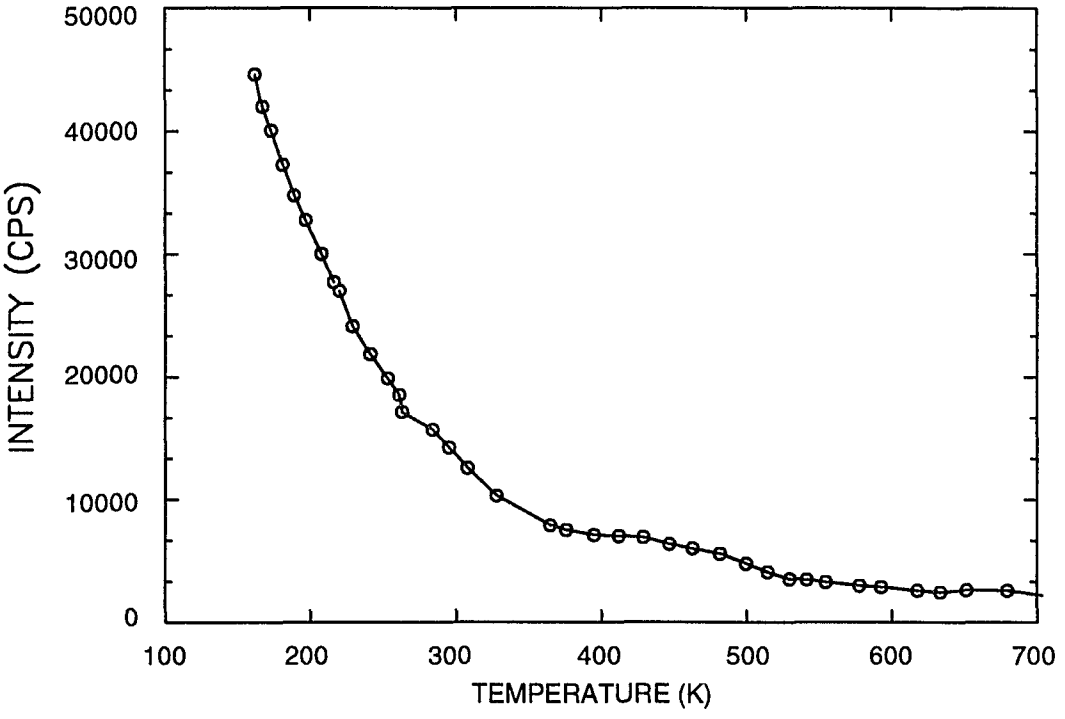

Figure 50. Spot FWHM vs. temperature of 1ML/Cu(110) deposited at 300K

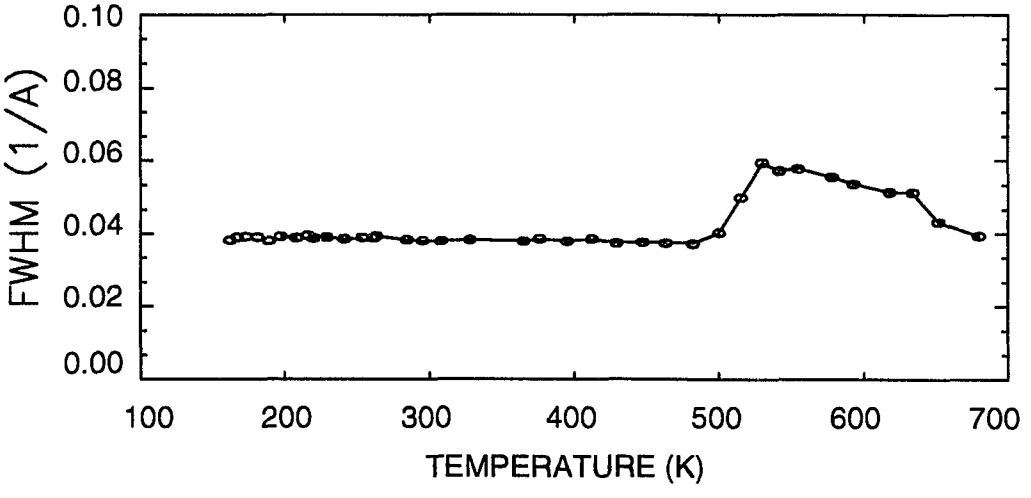

Figure 51. Changes of the AES spectra of 1ML Fe/Cu(110) deposited at 300K.

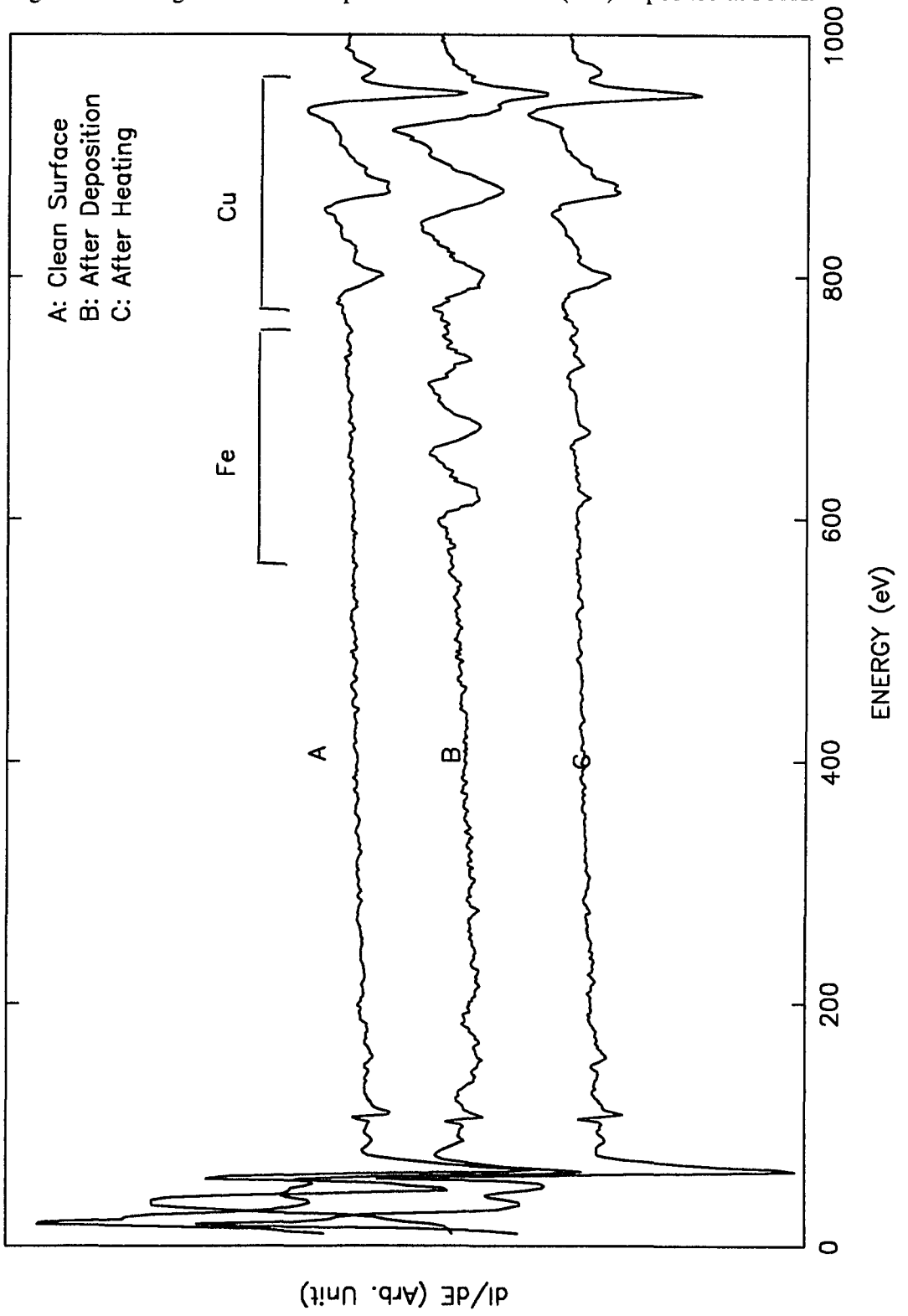

LEED pattern. The LEED signal is too weak to measure. The growth under this condition is very bad.

3ML Fe deposited on Cu(110) at high temperature

We deposit 3 monolayers of Fe on Cu(110) at 473K and measure the LEED spot profiles at various temperatures. The intensity and the FWHM change abnormally at 250K and 500K (Figure 52 and Figure 53). Figure 54 shows the changes of the AES spectra of 3ML Fe/Cu(110) deposited at 473K.

3ML on Cu(110) deposited at room temperature

We deposit 3 monolayers Fe on Cu(110) at 300K and measure the LEED spot profiles at various temperatures. The intensity vs. temperature shows a similar pattern as that of 1ML Fe/Cu(110) deposited at high temperature (Figure 55 and Figure 56). Figure 57 shows the changes of the AES spectra of 3ML Fe/Cu(110) deposited at 300K.

3ML Fe on Cu(110) deposited at low temperature

We deposit 3 monolayer Fe on Cu(110) at 173K. We can not get a clear and sharp LEED pattern. The LEED signal is too weak to measure.

4.3.3 Cu(111)

1ML Fe on Cu(111) deposited at high temperature

We deposit 1 monolayer Fe on Cu(111) at 473K and measure the LEED spot profiles at various temperatures. The intensity vs. temperature follows the exponential decreasing quite well until 550K (Figure 58 and Figure 59). Figure 60 shows the changes of the AES spectra of 1ML Fe/Cu(111) deposited at 473K.

Figure 52. Spot intensity vs. temperature of 3ML/Cu(110) deposited at 473K

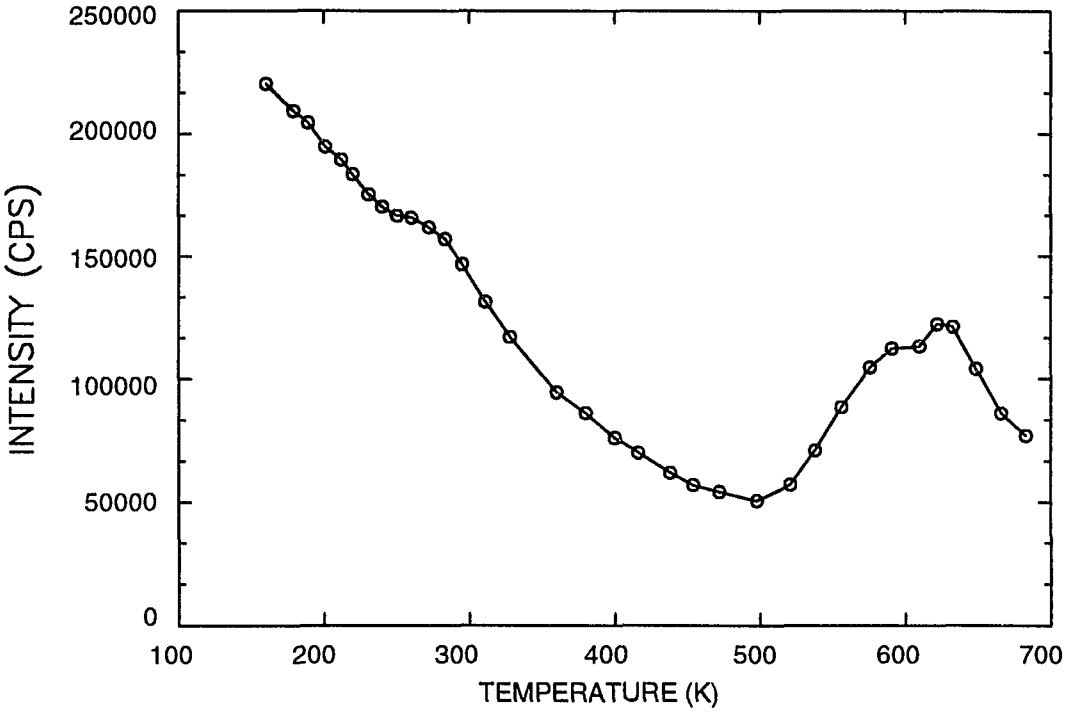

Figure 53. Spot FWHM vs. temperature of 3ML/Cu(110) deposited at 473K

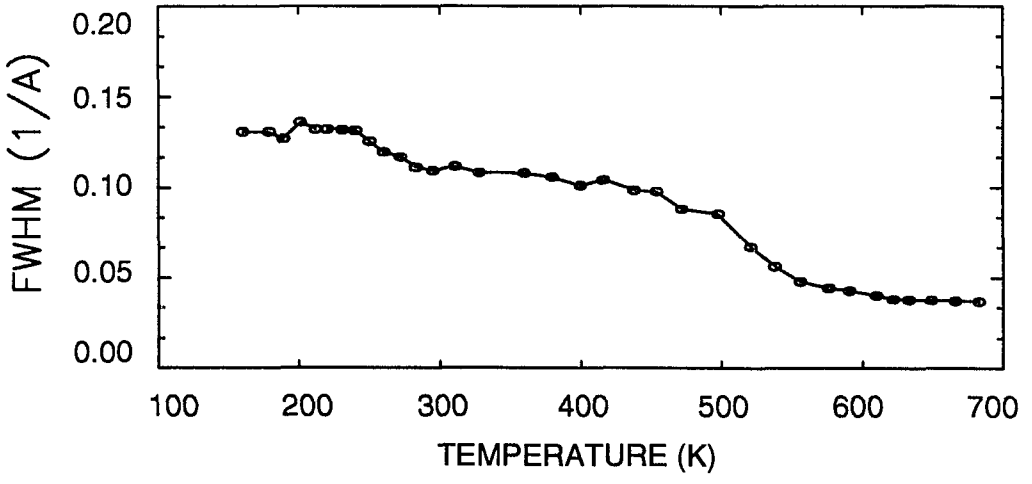

Figure 54. Changes of the AES spectra of 3ML Fe/Cu(110) deposited at 473K.

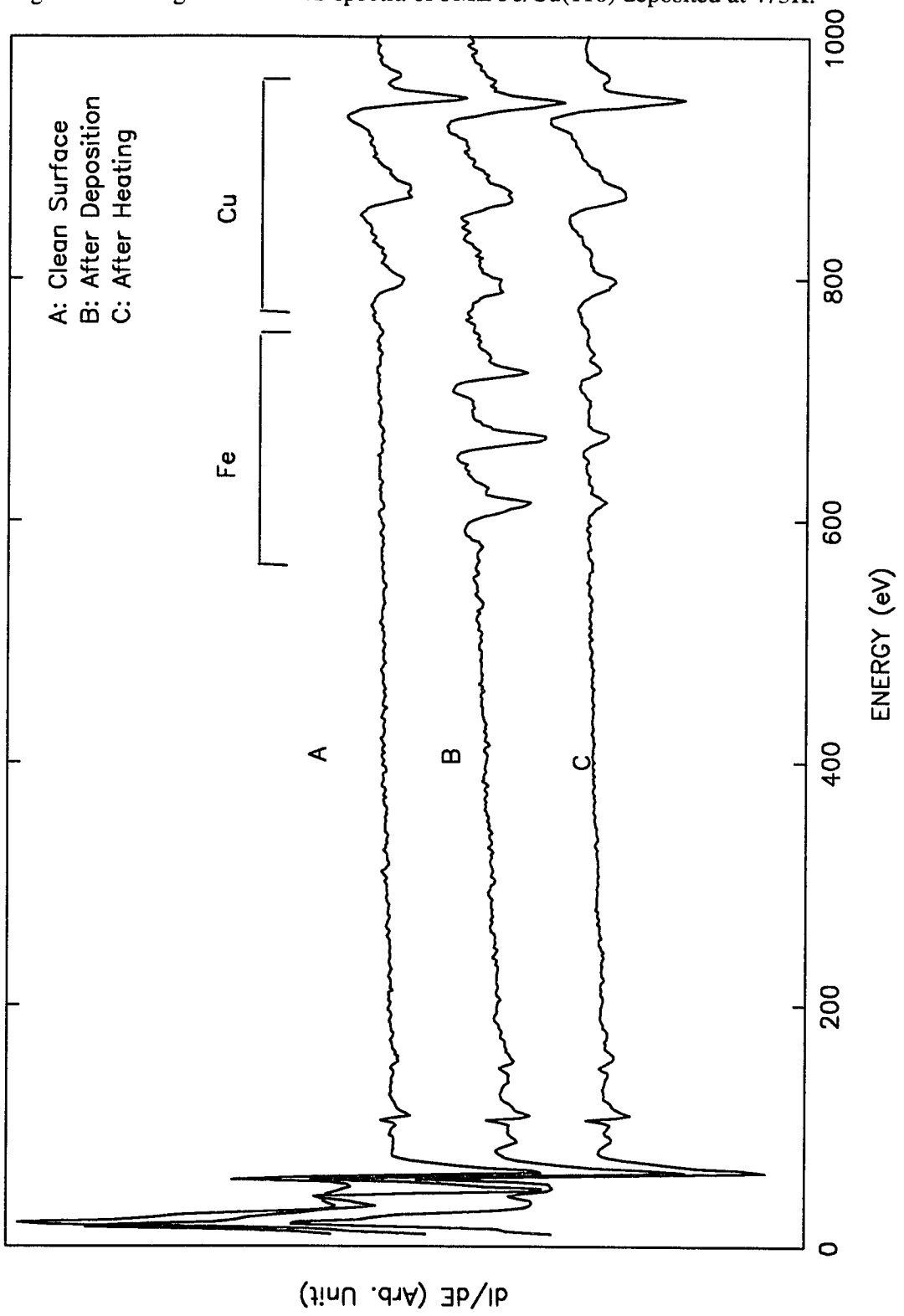

Figure 55. Spot intensity vs. temperature of 3ML/Cu(110) deposited at 300K

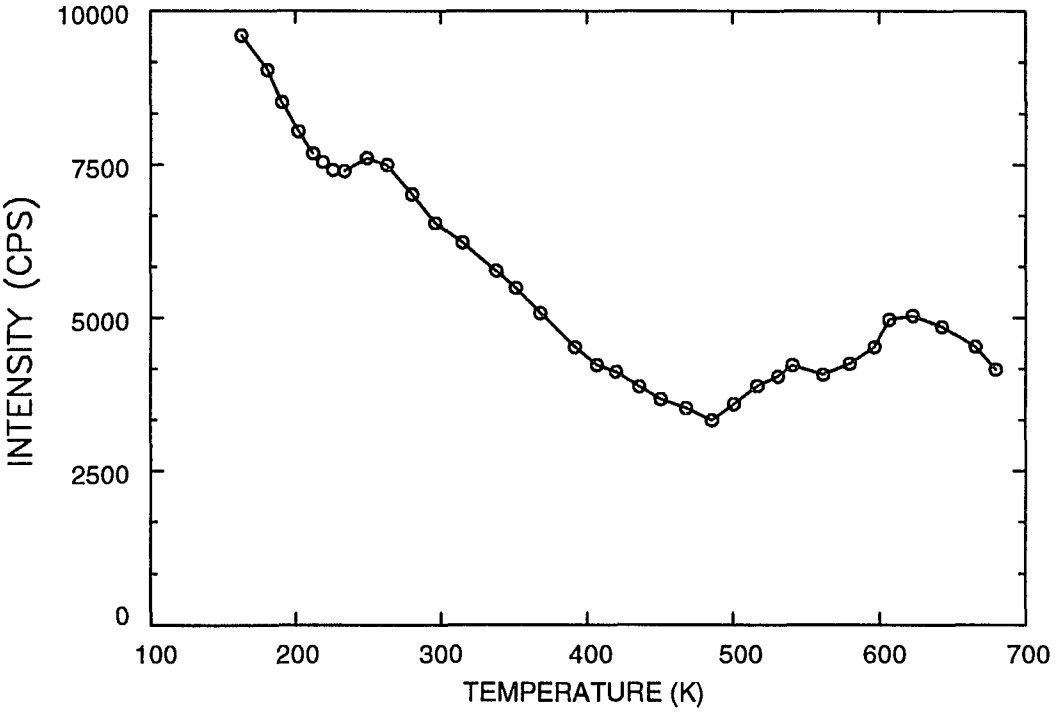

Figure 56. Spot FWHM vs. temperature of 3ML/Cu(110) deposited at 300K

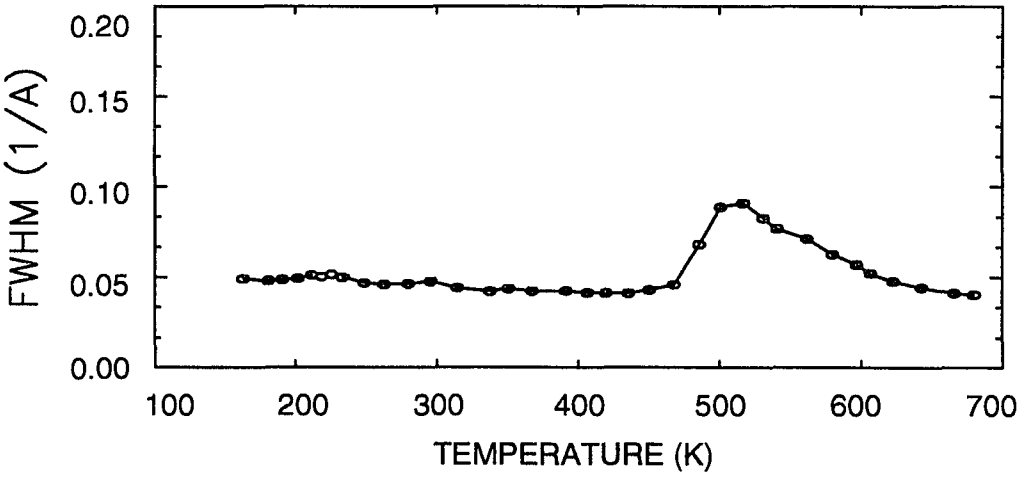

Figure 57. Changes of the AES spectra of 3ML Fe/Cu(110) deposited at 300K.

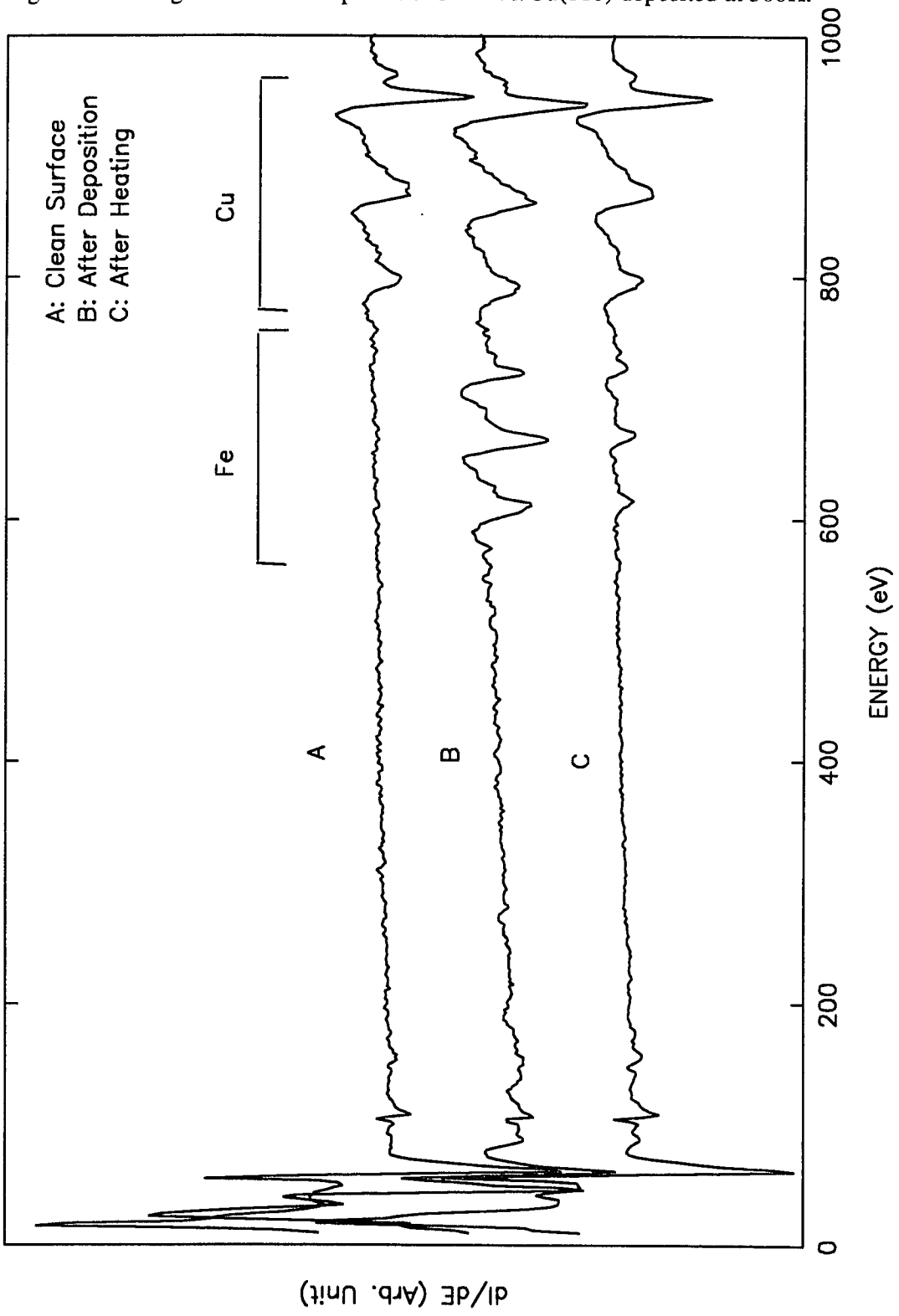

Figure 58. Spot intensity vs. temperature of 1ML/Cu(111) deposited at 473K

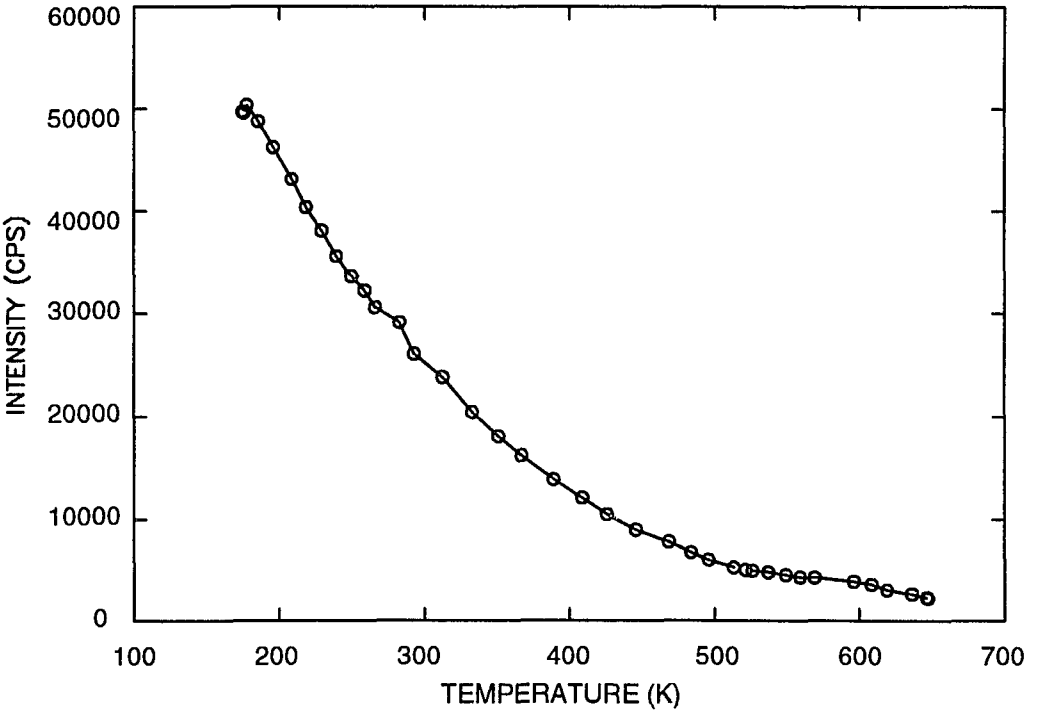

Figure 59. Spot FWHM vs. temperature of 1ML/Cu(111) deposited at 473K

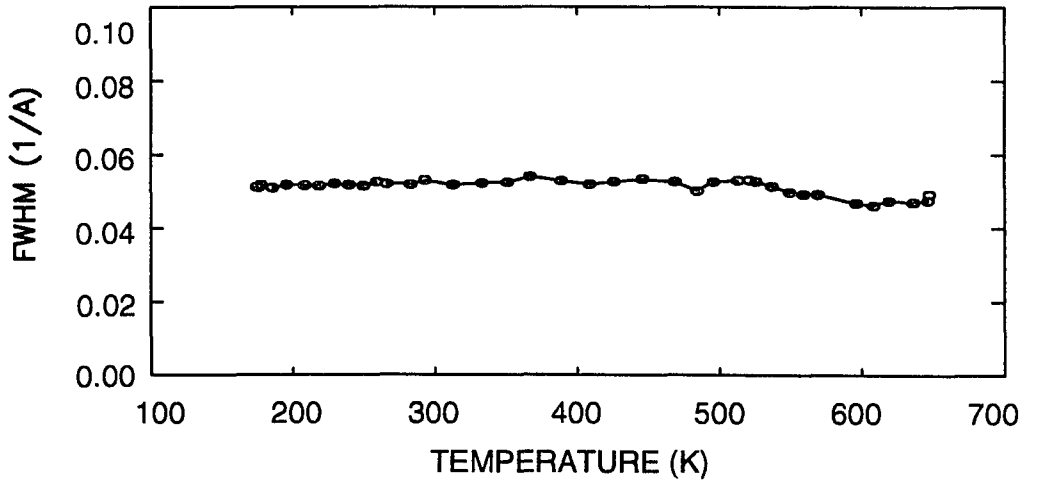

Figure 60. Changes of the AES spectra of 1ML Fe/Cu(111) deposited at 473K.

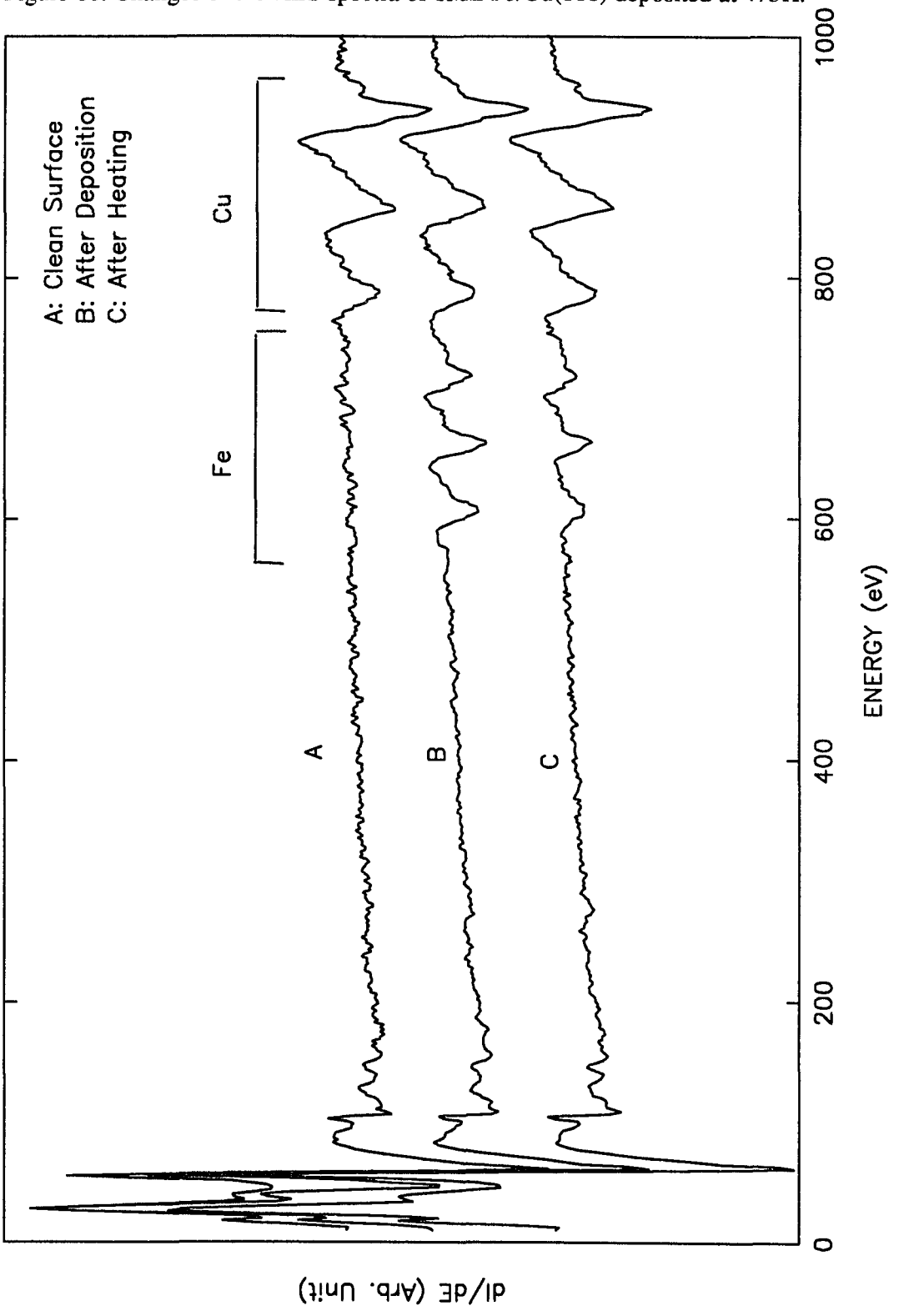

1ML Fe on Cu(111) deposited at room temperature

We deposit 1 monolayer Fe on Cu(111) at 300K and measure the LEED spot profiles at various temperatures. The intensity vs. temperature follows the exponential decreasing quite well until 450K (Figure 61). The FWHM also changes abnormally at that temperature also (Figure 62). Figure 63 shows the changes of the AES spectra of 1ML Fe/Cu(111) deposited at 300K.

1ML Fe on Cu(111) deposited at low temperature

We deposit 1 monolayer Fe on Cu(111) at 173K and measure the LEED spot profiles at various temperatures. The intensity vs. temperature follows an exponentially decreasing function quite well until 500K. The abnormality appears at 500K (Figure 64 and Figure 65). Figure 66 shows the changes of AES spectra of 1ML Fe/Cu(111) desposited at 173K.

3ML Fe on Cu(111) deposited at high temperature

We deposit 3 monolayers Fe on Cu(111) at 473K and measure the LEED spot profiles at various temperatures. The intensity vs. temperature follows an exponentially decreasing function quite well until 550K. A small abnormal increase appears at 550K (Figure 67) The FWHM also changes abnormally at that temperature (Figure 68). Figure 69 shows the changes of the AES spectra of 3ML Fe/Cu(111) deposited at 473K.

3ML Fe on Cu(111) deposited at room temperature

We deposit 3 monolayers Fe on Cu(111) at 300K and measure the LEED spot profiles at various temperatures. The intensity vs. temperature follows an exponentially decreasing function quite well until 450K. The intensity bounces up slightly as temperature increases to 600K then falls back after that (Figure 70 and Figure 71). Figure 72 shows the changes of the AES spectra of 3ML Fe/Cu(111) deposited at 300K.

Figure 61. Spot intensity vs. temperature of 1ML/Cu(111) deposited at 300K

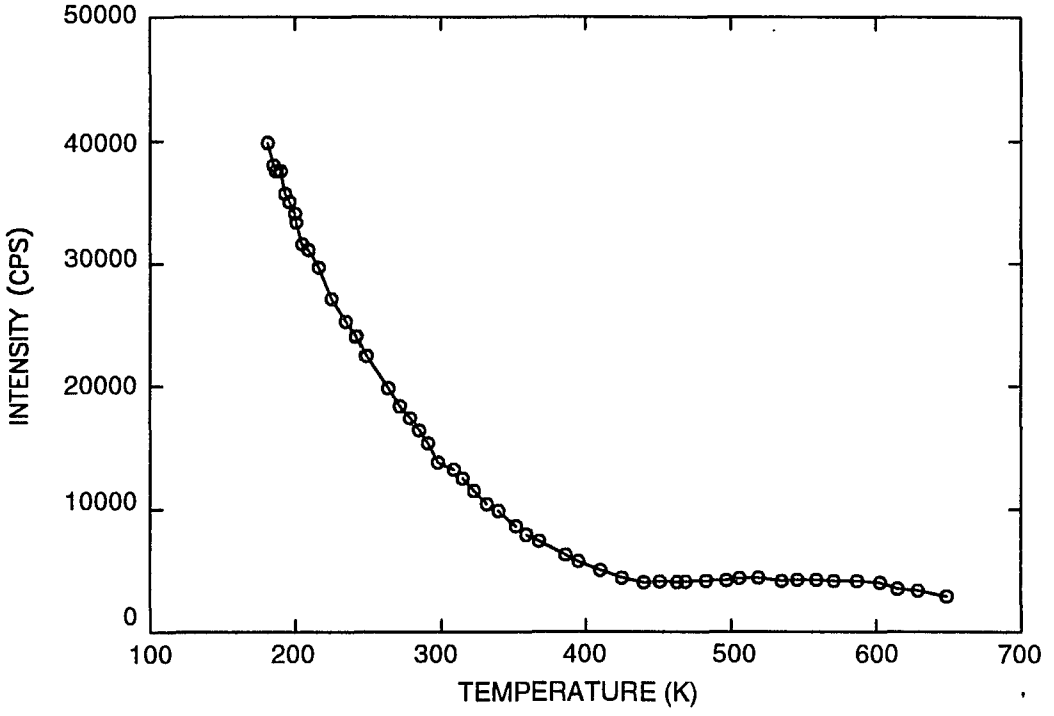

Figure 62. Spot FWHM vs. temperature of 1ML/Cu(111) deposited at 300K.

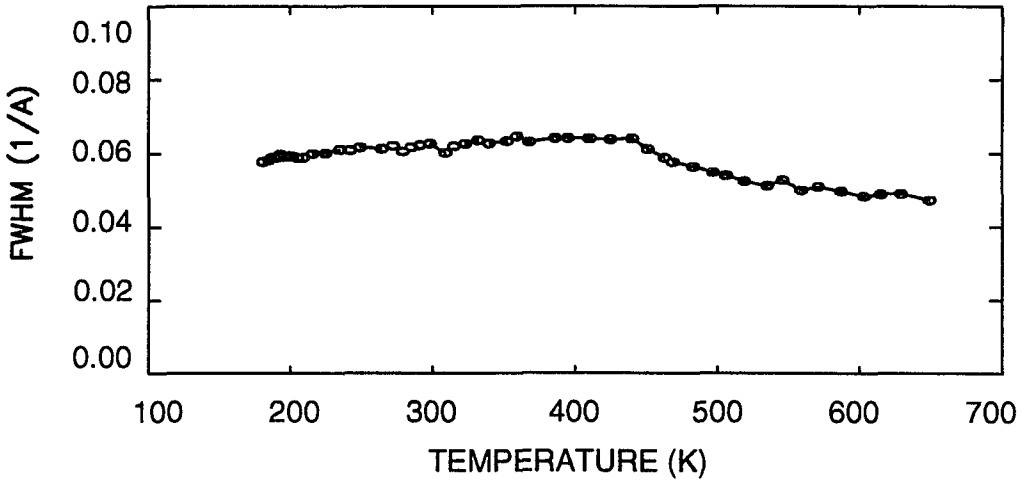

Figure 63. Changes of the AES spectra of 1ML Fe/Cu(111) deposited at 300K.

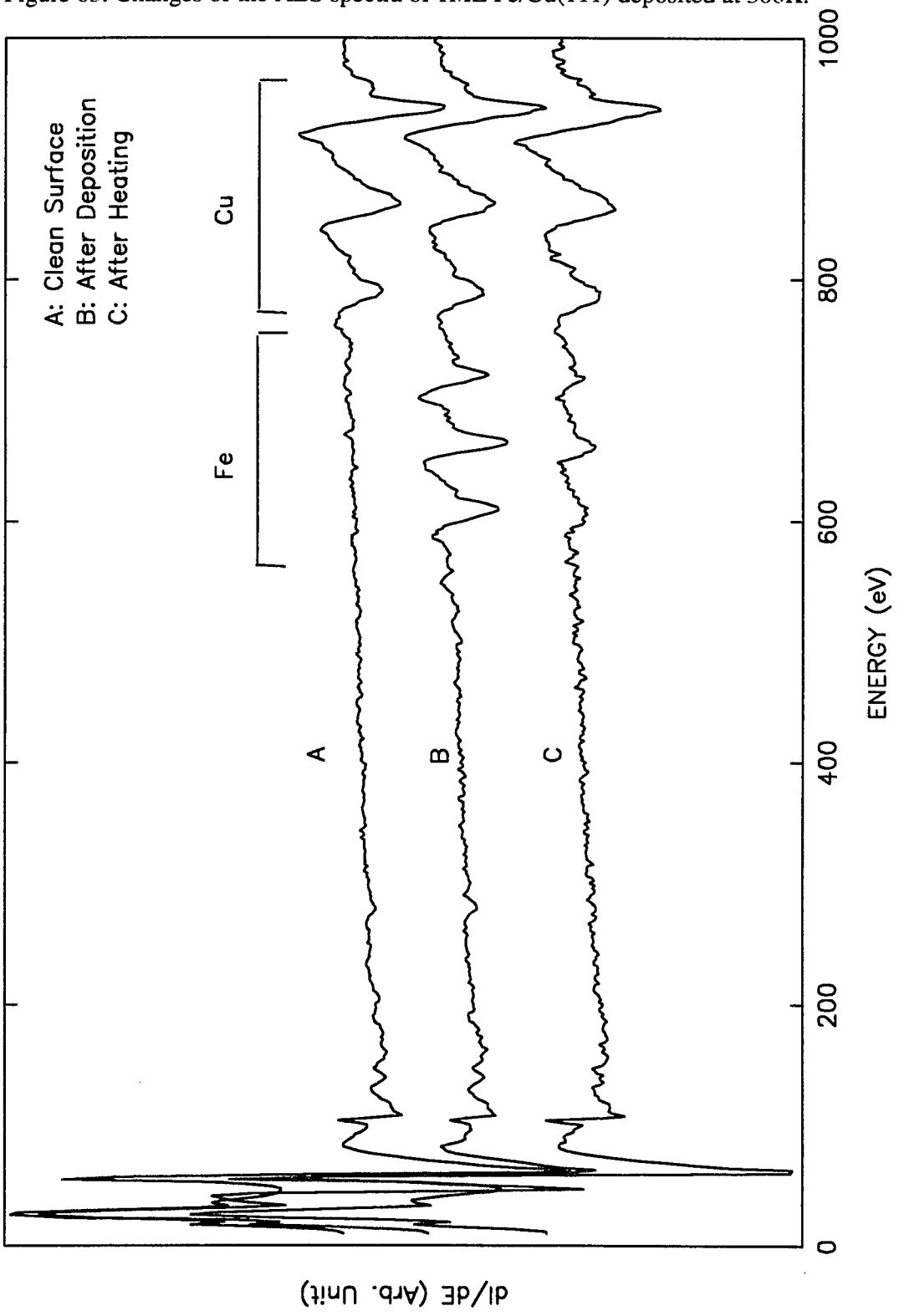

Figure 64. Spot intensity vs. temperature of 1ML/Cu(111) deposited at 173K.

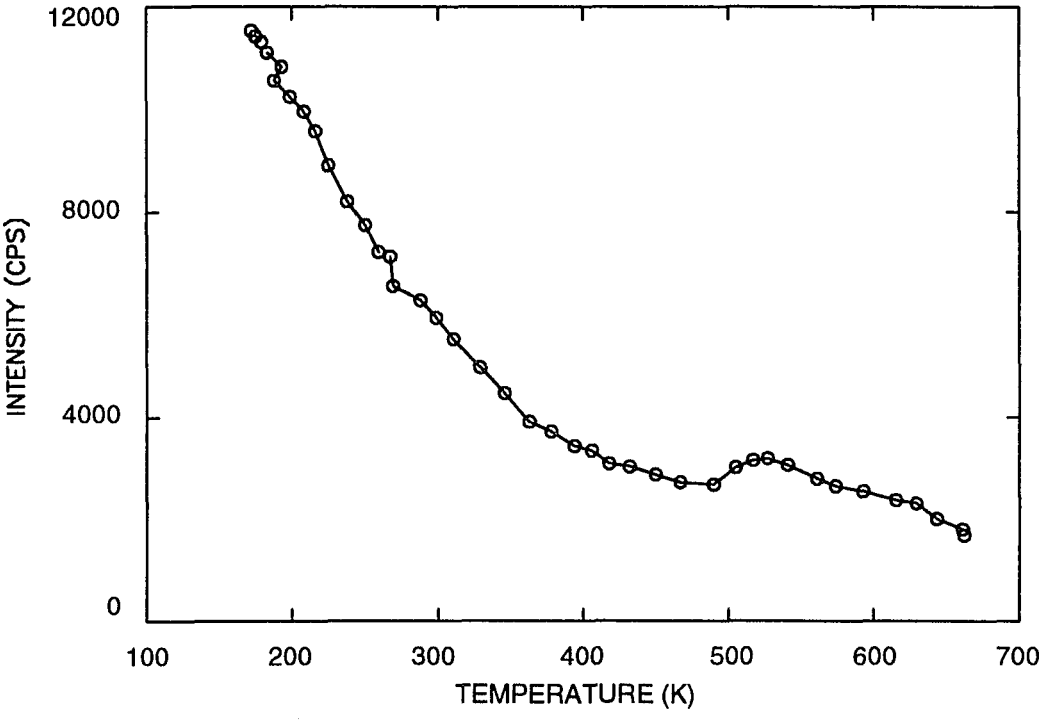

Figure 65. Spot FWHM vs. temperature of 1ML/Cu(111) deposited at 173K.

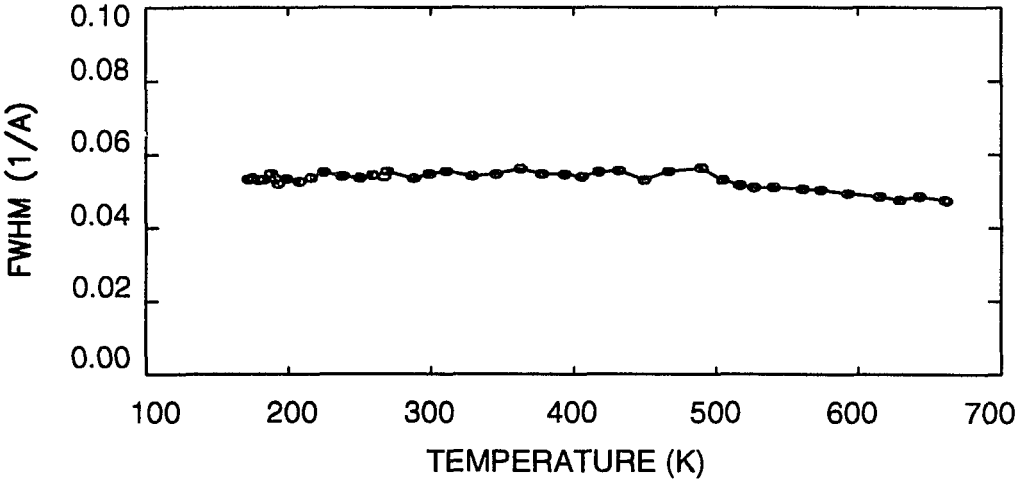

Figure 66. Changes of the AES spectra of 1ML Fe/Cu(111) deposited at 173K.

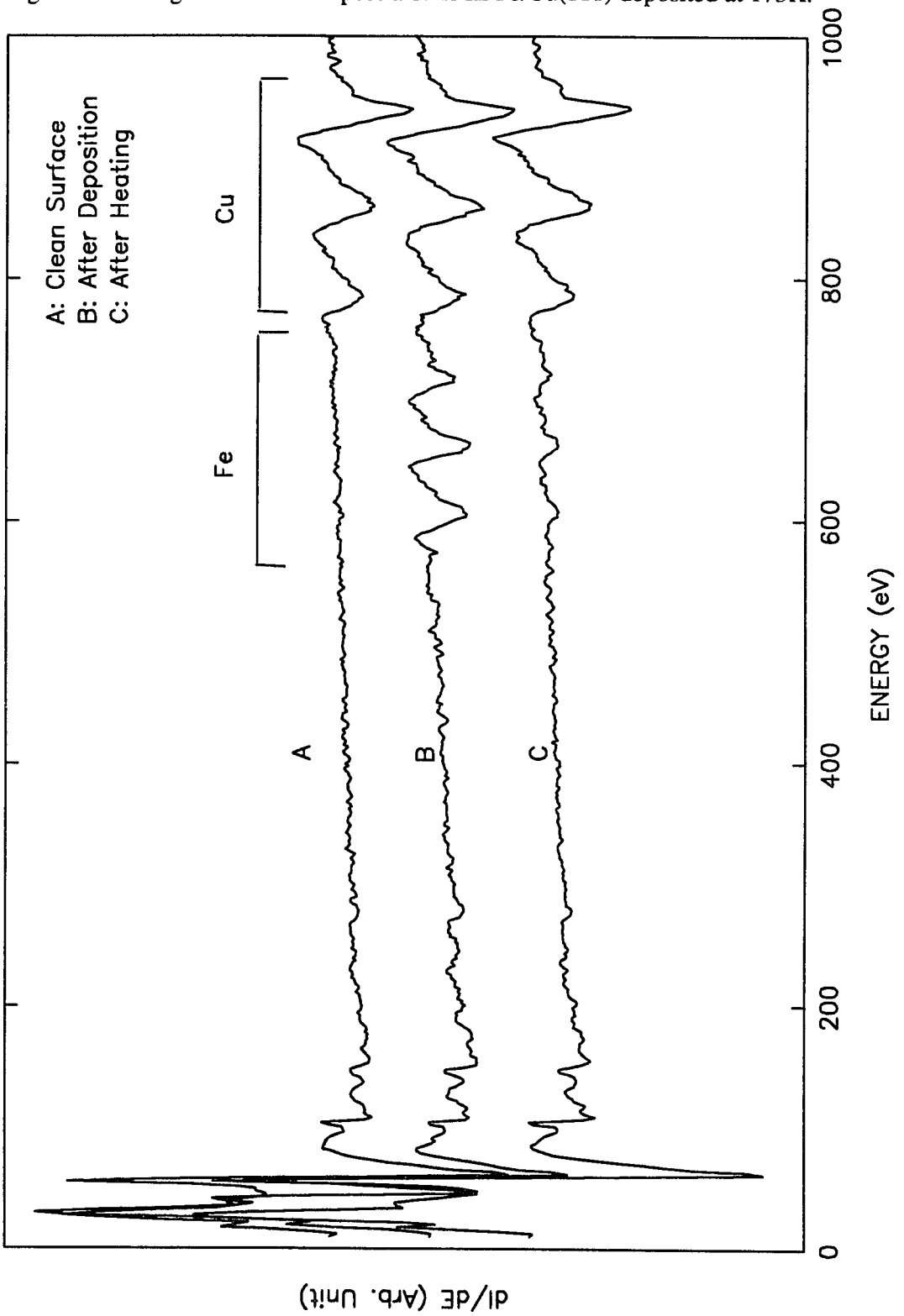

Figure 67. Spot intensity vs. temperature of 3ML/Cu(111) deposited at 473K.

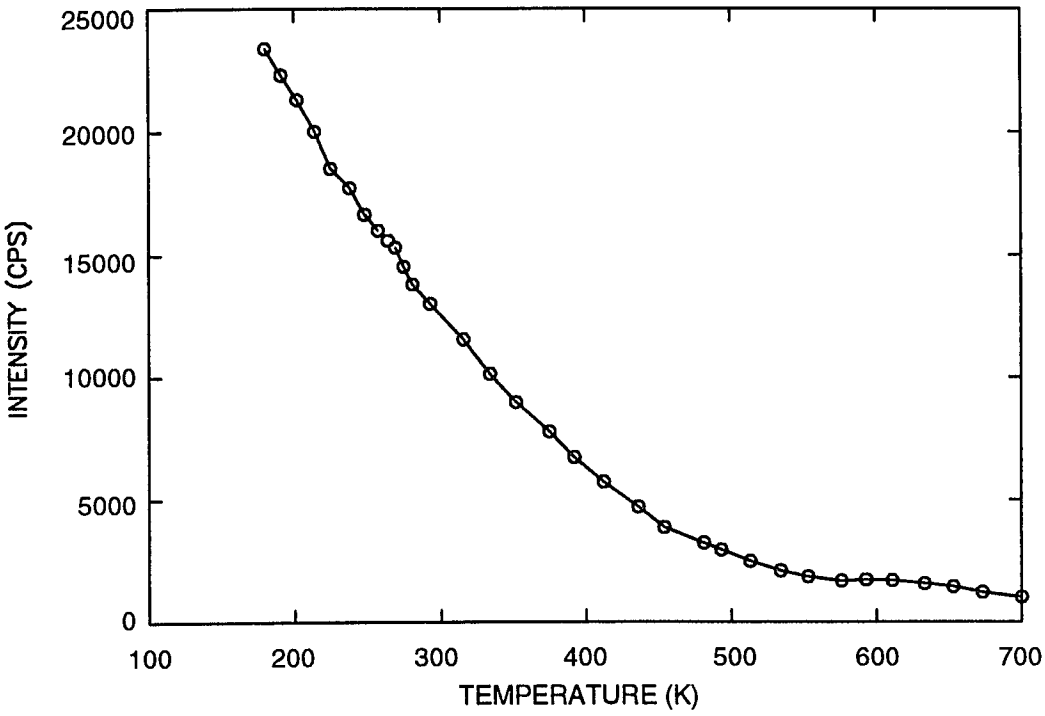

Figure 68. Spot FWHM vs. temperature of 3ML/Cu(111) deposited at 473K

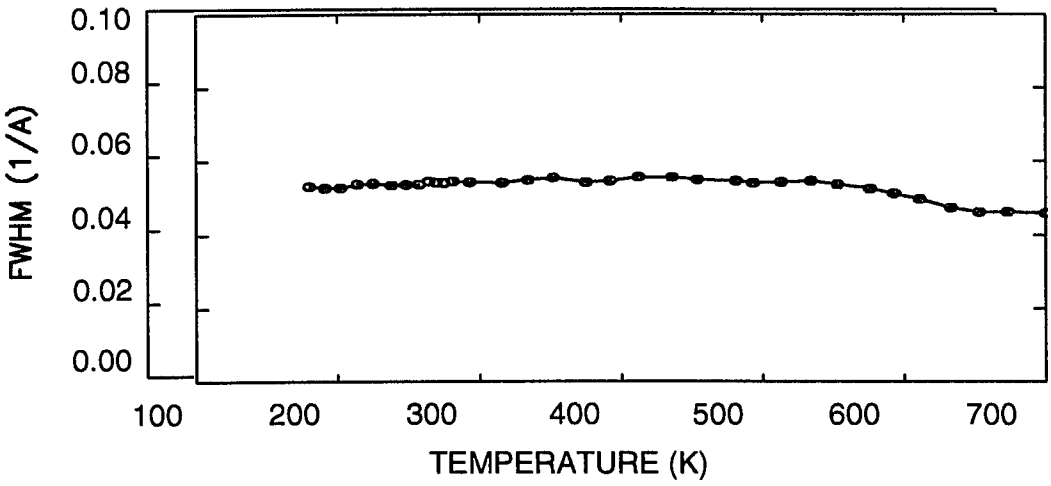

Figure 69. Changes of the AES spectra of 3ML Fe/Cu(111) deposited at 473K.

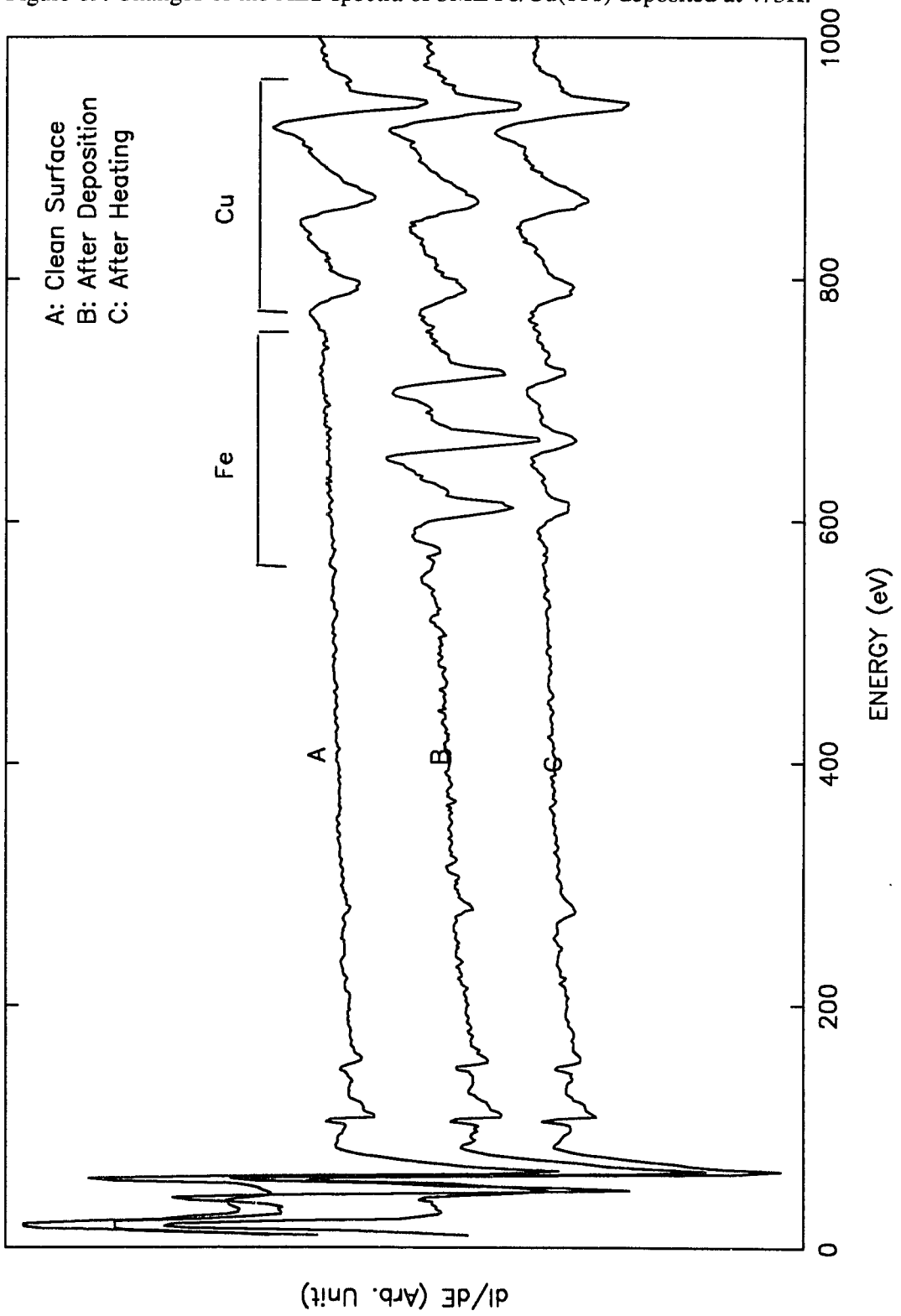

Figure 70. Spot intensity vs. temperature of 3ML/Cu(111) deposited at 300K.

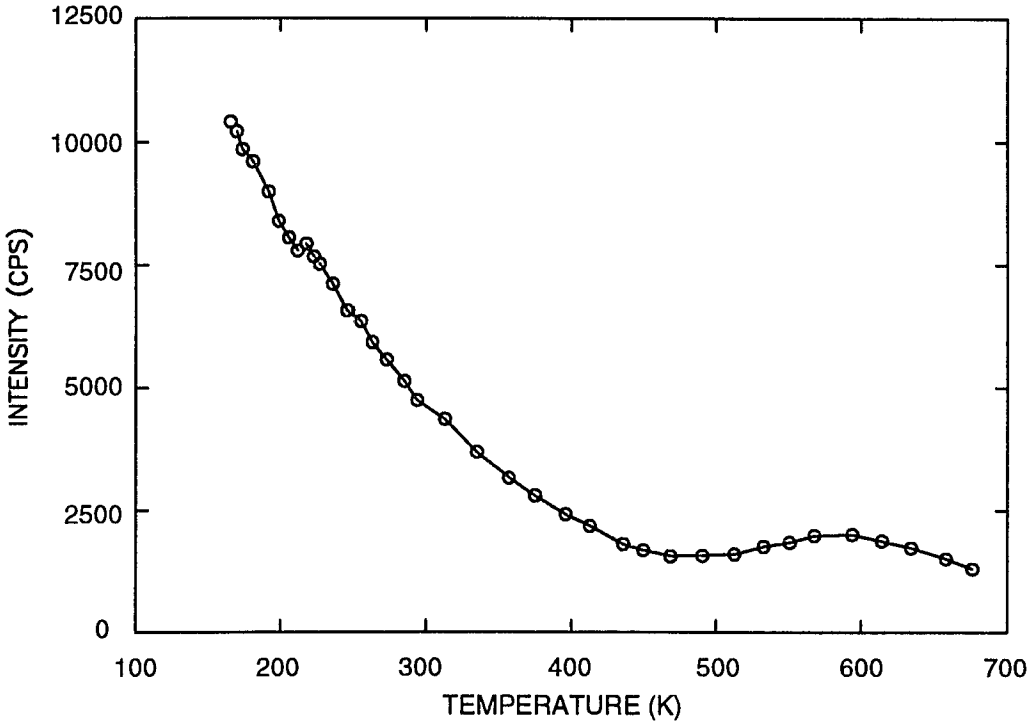

Figure 71. Spot FWHM vs. temperature of 3ML/Cu(111) deposited at 300K.

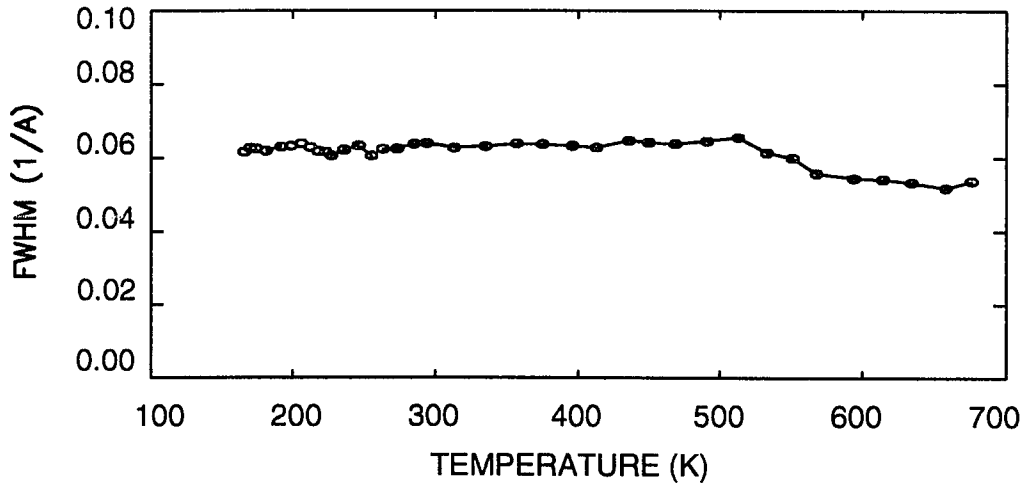

Figure 72. Changes of the AES spectra of 3ML Fe/Cu(111) deposited at 300K.

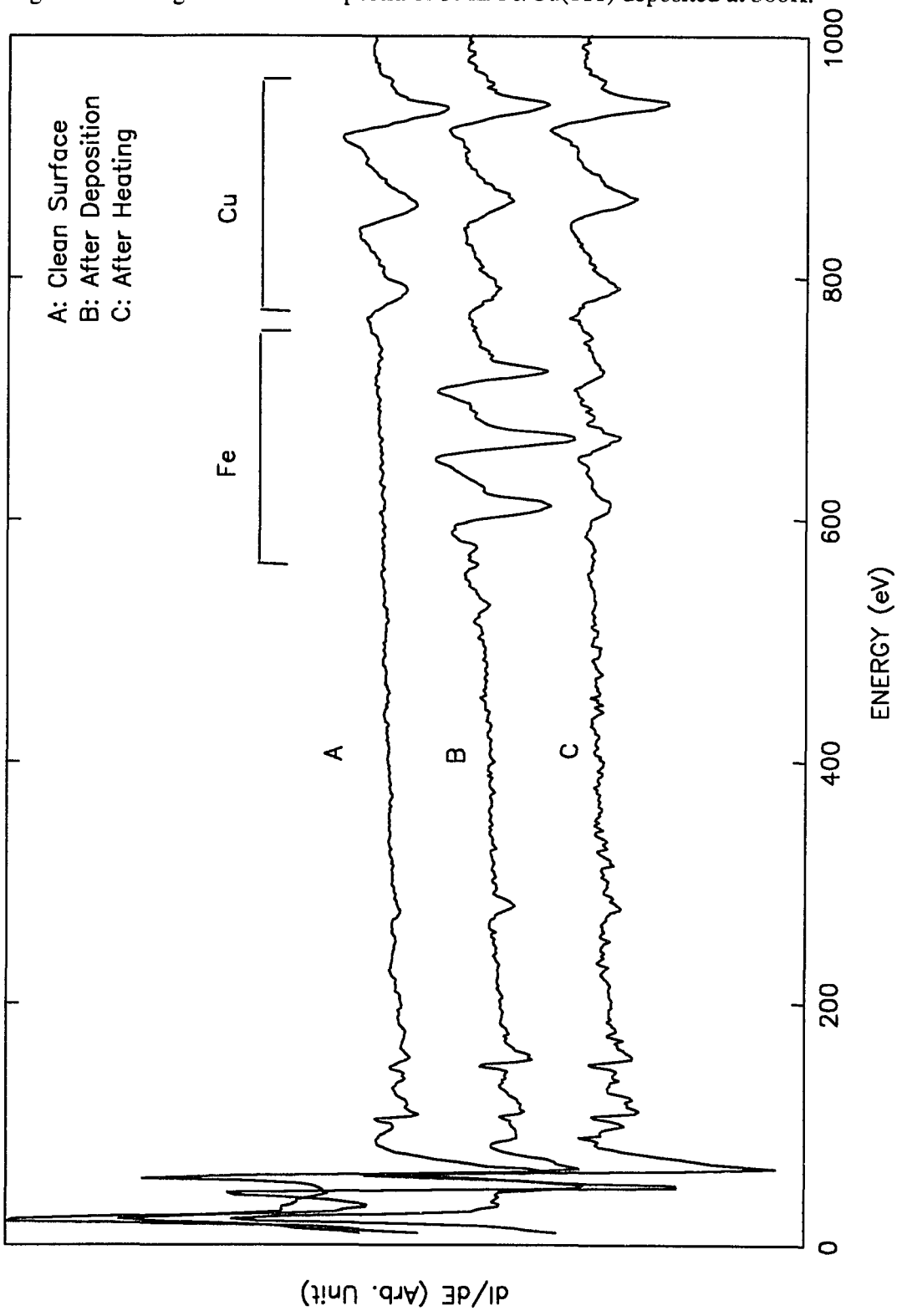

3ML Fe on Cu(111) deposited at low temperature

We deposit 3 monolayers Fe on Cu(111) at 473K and measure the LEED spot profiles at various temperatures. The intensity vs. temperature shows abnormal changes at temperature 250K and 450K (Figure 73 and Figure 74). Figure 75 shows the changes of the AES spectra of 3ML Fe/Cu(111) deposited at 173K.

4.4 Spot Profiles and Thermal Stability of the Fe Thin Films

After successful deposition of iron the coverage is measured using AES. The sample is then cooled to below 170K using LN_2. We then start with the temperature dependent measurements from 173K and raise the temperature eventually up to 673K. Along the way, we record the spot profiles every 35K. The whole process takes about 40 minutes to 1 hour, depending on the LEED signal strength. After that the sample is cooled to the beginning temperature with LN_2 flowing through the sample holder. The spot profile is measured again to make a comparison of before and after annealing process. The intensity and structure of the spot profile change dramatically as the function of temperature and iron coverage (Figure 76 **a** and **b**).

For 1ML Fe on Cu(100), Figure 76**a**, the spot profile has a clear ring structure around the sharp central spike before the heating. As the temperature rises, it shrinks and disappears eventually when the temperature is above 550K. The change is irreversible when the temperature is brought back to where it has started. The spot profile does not have the ring structure any more. However, the central spike is much brighter than it was before the annealing.

For 3ML Fe on Cu(100), Figure 76**b**, the result is similar although the spot profile starts with a broad shoulder around the central spike. The shoulder disappears at temperature above 550K and the change is irreversible. The intensity of the central spike is much higher after the annealing.

Figure 73. Spot intensity vs. temperature of 3ML/Cu(111) deposited at 173K.

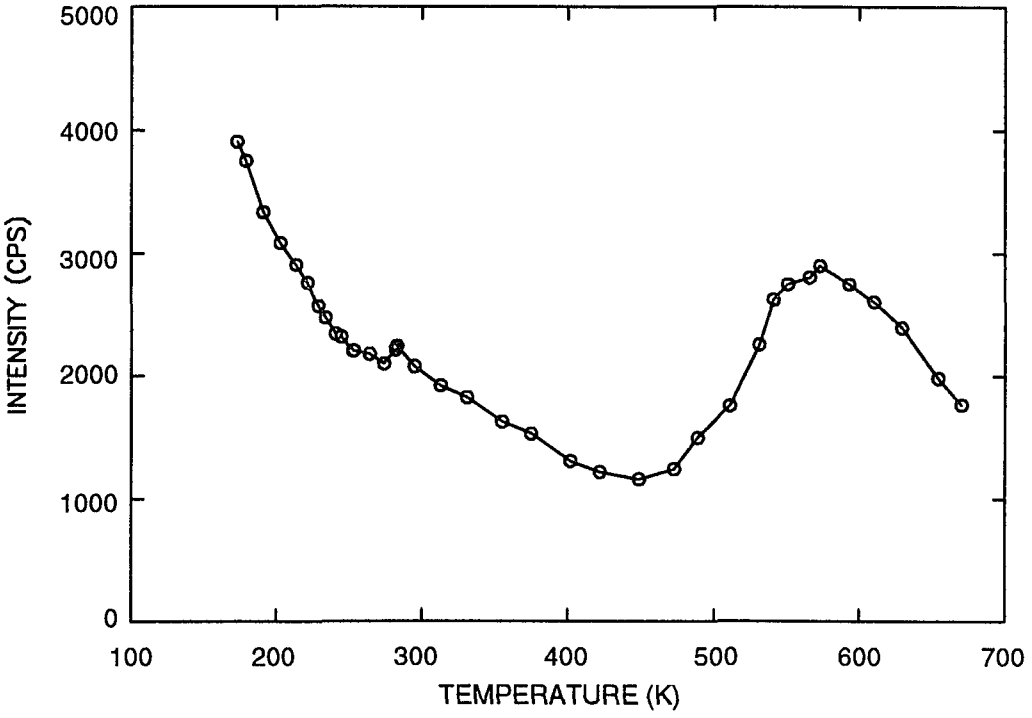

Figure 74. Spot FWHM vs. temperature of 3ML/Cu(111) deposited at 173K

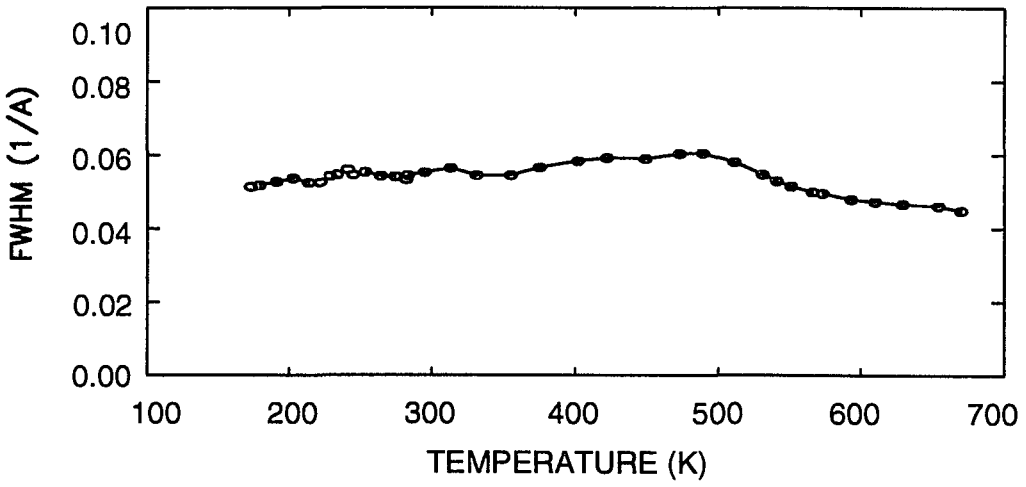

Figure 75. Changes of the AES spectra of 3ML Fe/Cu(111) deposited at 173K.

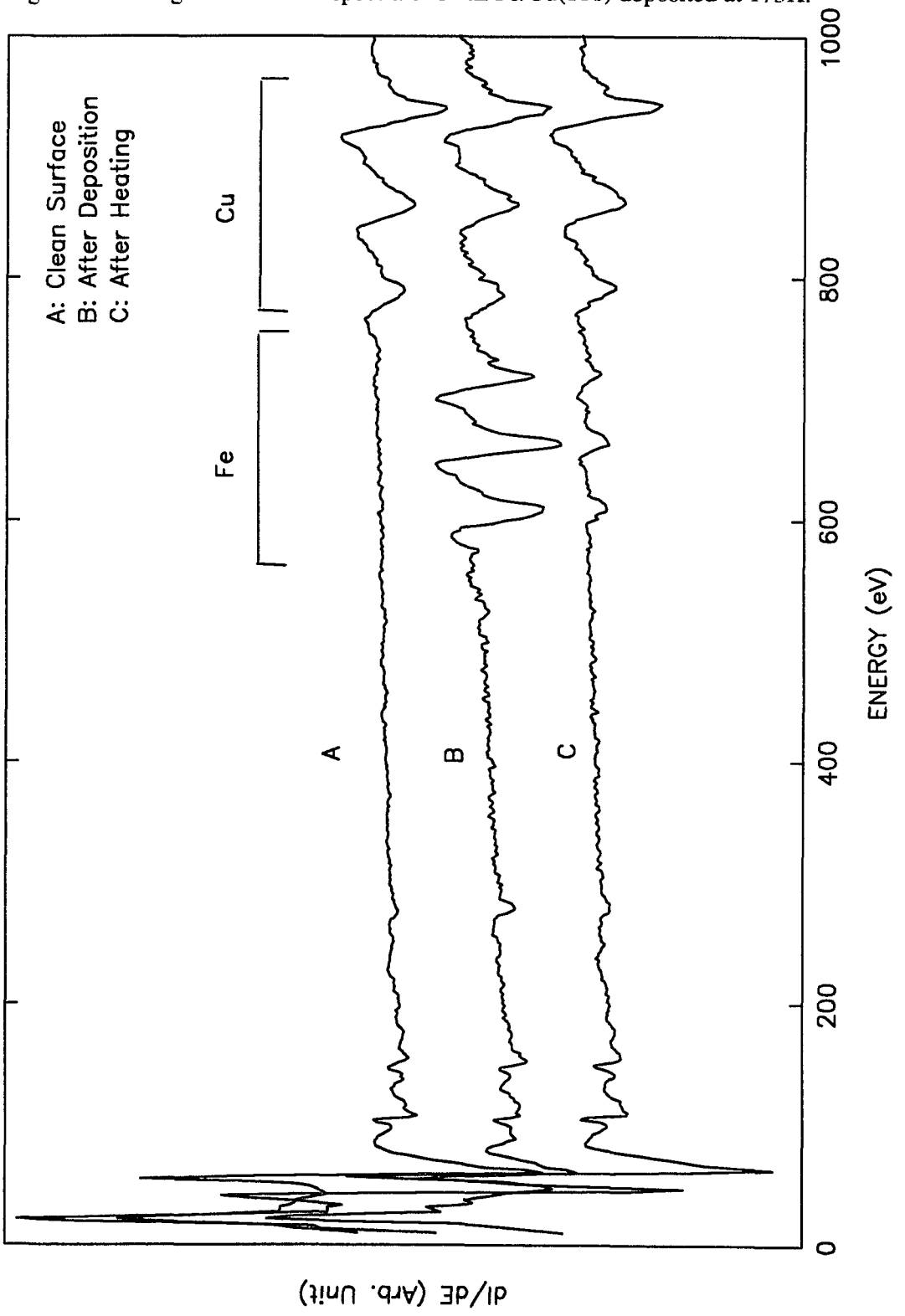

Figure 76 Profiles and the temperature after the Fe depositions.

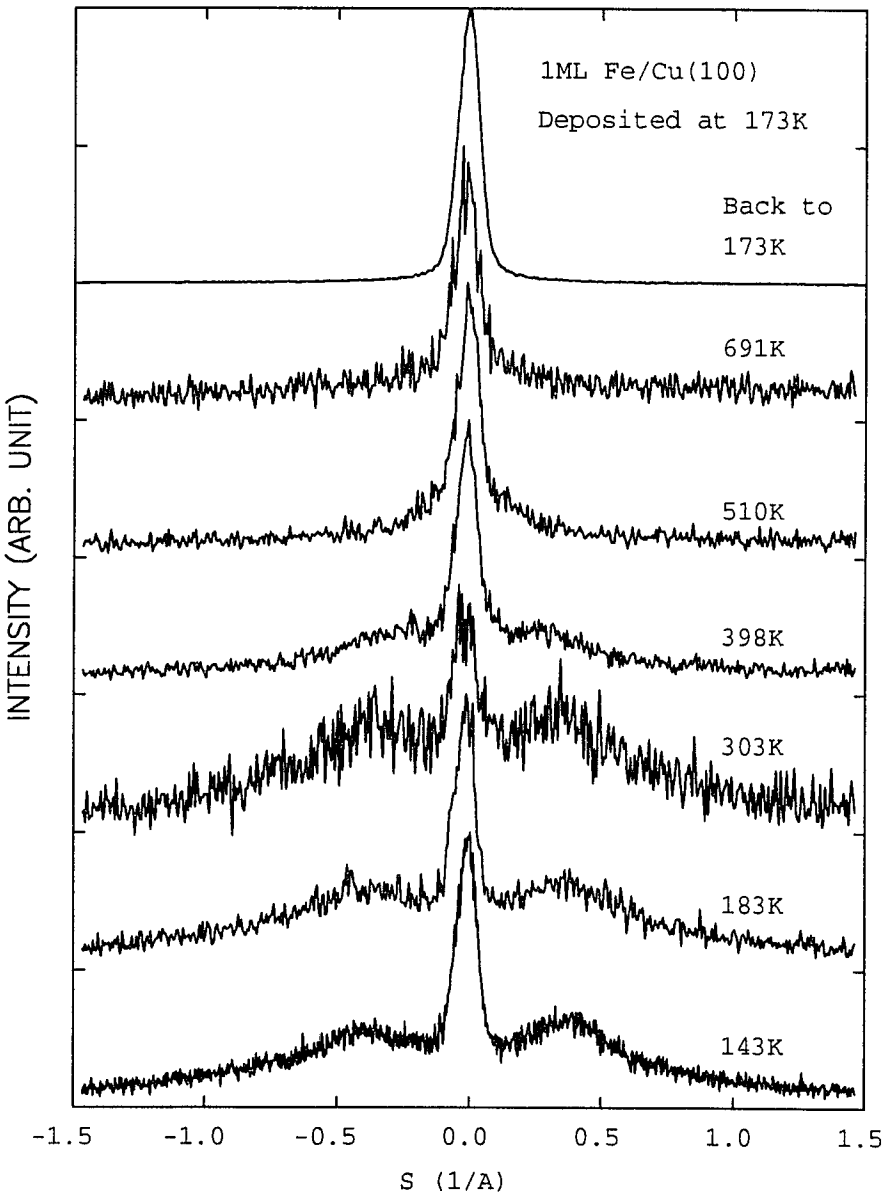

(a)

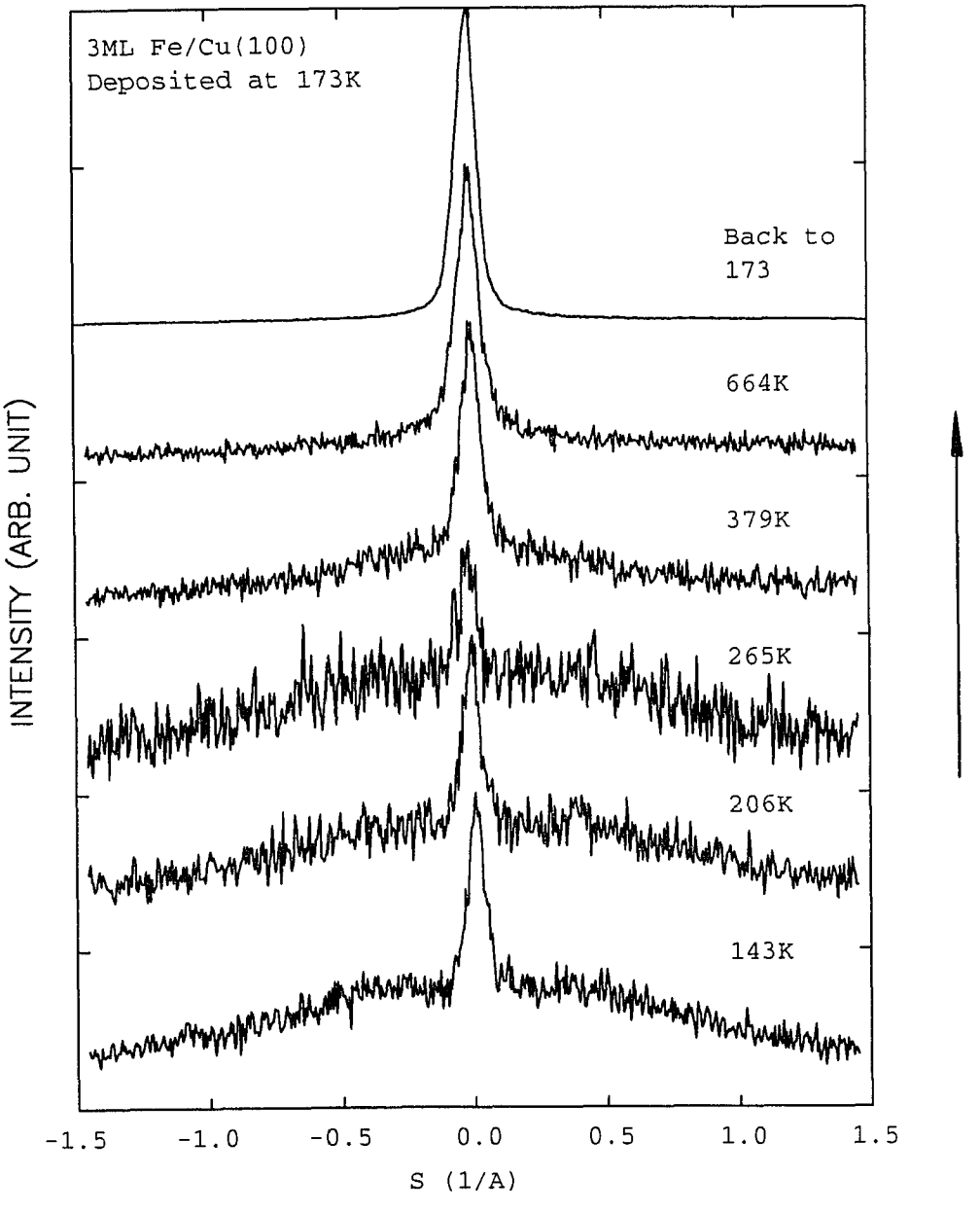
3ML Fe/Cu(100)
Deposited at 173K
Back to
173
664K
379K
265K
206K
143K
INTENSITY (ARB. UNIT)
-1.5
-1.0
-0.5
0.0
0.5
1.0
1.5
S (1/A)

(b)

For those Fe films that deposited at other conditions, their spot profiles do not change as much as in the above cases. There is a trend that the spot becomes sharper after annealing and the changes are irreversible.

4.5 Auger Electron Spectra

AES spectra are measured many times during the cleaning-annealing-deposition processes. We save those important spectra, i.e., the cleaned one before the deposition, the one after the deposition and before the temperature dependence measurement, and the one after the temperature dependence measurement. The AES spectrum not only services as a mean to monitor the impurity and to determine the iron coverage, but also gives us a hint on what may change on the surface.

We use the peak-to-peak intensity at the characteristic Auger electron energies 105eV and 920eV for Cu and 47eV and 651eV for Fe to determine the Fe coverage on the Cu substrates. Figure 77(**a**) for Cu(100) and figure 77(**b**) for Cu(111) show some typical Auger spectra for a set of measurement. Spectrum A is measured on the clean Cu surface before the Fe deposition. Only the Cu Auger peaks are there in the spectrum. Spectrum B is taken right after the depostion and before the heating. The spectrum shows both the Fe and Cu Auger peaks. The Fe coverage for this particular deposition is 3ML determined by the peak-to-peak intensities mentioned above. The spectrum C is taken at room temperature after the sample is heated to 700K in the temperature dependent measurement. It is clear that the Fe Auger signal reduces significantly by the heating process.

The decrease of the Fe Auger signal after the heating is observed for all three Cu samples. The amount of decrease is correlated to the change of LEED spot intensity. The change is more significant for sample deposited at low temperature than high temperature. Among the samples deposited at the same temperature, the Fe Auger signal of the sample with 3ML coverage changes the most.

Figure 77. (**a**) AES spectra before and after temperature dependence measurement for 3ML Fe/Cu(100).

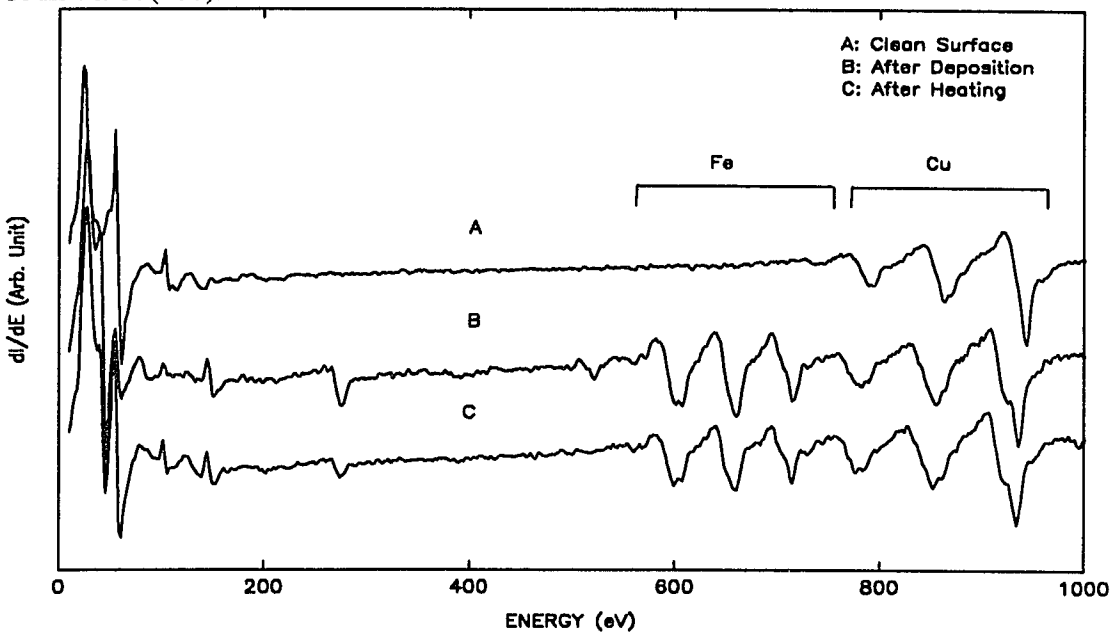

(**b**) AES spectra before and after temperature dependence measurement for 3ML Fe/Cu(111).

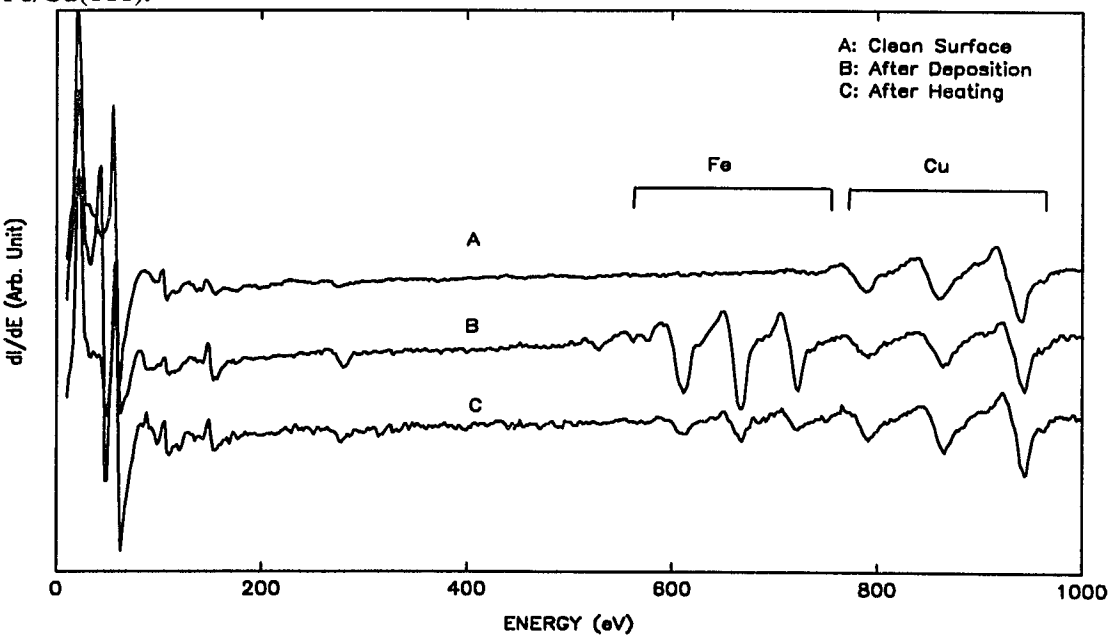

CHAPTER 5

DISCUSSION

5.1 Previous Works

A lot of research has been devoted to the study of metastable fcc iron films grown on Cu(100) after it was shown that these films have intriguing magnetic properties. 3-5 monolayer thick films prepared at low temperature (below room temperature) [10, 34] are ferromagnetic with an easy axis perpendicular to the surface, and an irreversible loss of magnetization is observed on heating these films to 350K [12]. On the other hand, 10-17 monolayer thick films prepared at 500K are paramagnetic at room temperature and antiferromagnetic at low temperature [11], and the coated films have an average magnetic dipole moment per atom that depends on their thickness and their growth temperature [13]. Films prepared at 463K shows in-plane surface ferromagnetism for the top layer, and the ferromagnetism disapperars after the sample is cooled down or after a certain amount of time[9]. A structural study done by measurement of the angular distribution of the $2p_{3/2}$ core-level photoemission intensity shows that the temperature of the substrate during the growth of the film influences its quality [4]. The initial stage of epitaxy (1-2 monolayers) of Fe on Cu(100) is found to be of critical importance in determining the quality of the films, sandwiches, and superlattices. Their results show that Fe grows as a poorly ordered film for substrate temperatures below ~200K, that Fe agglomerates for substrate temperatures of about 200-300K, and that for substrate temperatures at or slightly above 300K Cu segregation accompanies Fe deposition, yielding an intermixed film of Fe and Cu. This intermixing is particularly severe above 400K. Pescia et al. [10] could not grow fcc-Fe films thicker than 5 layers (owing to increasing amounts of bcc inclusions). Darici et al. [3] grew 17-layer films with no apparent difficulty. Clarke et al. [14] determined that 7-layer films have the same structure, i.e., the same layer spacing, as bulk terminated

Cu(100) crystal; thicker films contained an appreciable amount of disorder. With regard to the crystallographic structure of fcc-Fe, Onellion et al. [16] claim that 4-layer films grown on heated (423-473K) Cu(100) substrates have essentially the same layer spacing as Cu to within ±0.05Å.

The different substrate temperatures used by the various groups for growth of Fcc-Fe on Cu(100) would have produced varying amounts of Fe-Cu alloys, of bulk fcc-Fe, and of partially agglomerated Fe films. Thus the conflicting results reported for the magnetic properties of these samples are quite understandable.

The controversies in the literature prompt us to investigate the growth modes under certain growth conditions, especially at the growth temperatures that appeared in the literature. 170K, 300K and 473K are the temperatures that most people used as low, room and high temperatures for the Fe/Cu epitaxial growth study. We place our emphases on the initial stages of growth (~1 monolayer) because it is the most critical phase in the epitaxial growth.

5.2 Spot Intensity and Thermal Stability of the Fe Thin Films

For the clean Cu surfaces, the relation of spot intensity vs. the sample temperature fits the Debye model pretty well, Figure 78. The Debye model gives a straight line in the logarithm scale (Eq. 19 and Eq. 21) at high temperature. The data points are slightly off the straight line at the low temperature end. This is because the assumption of $T>>\Theta_D$ in the integral of equation Eq. 20 does not longer hold. The coherence length of the surface is derived from the FWHM of the spot profile. It decreases linearly as the temperature increases. Cu(100) and Cu(111) decrease at about the same rate 0.025 Å/K while Cu(110) has a much smaller rate (0.001 Å/K).

Figure 78. Intensity vs. temperature measured on clean Cu surfaces.

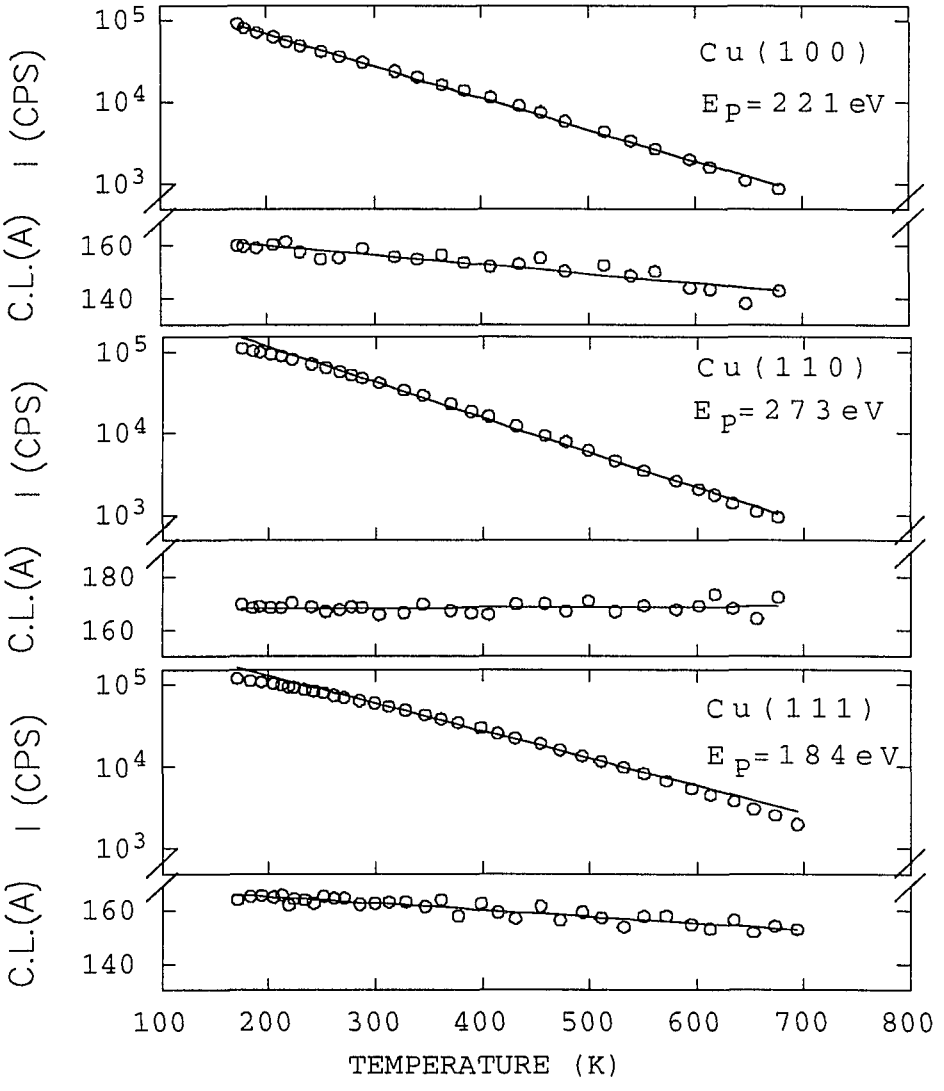

Upon the deposition of Fe, the temperature dependence begins to deviate from the behavior of the Debye model. Figure 79 is the spot intensity vs. temperature for 1ML Fe/Cu deposited at various temperatures and Figure 80 for 3ML. The abnormality occurs when the sample temperature reaches about 500 K. The spot becomes brighter as the temperature continues to rise, opposite to the normal Debye model behavior. At a certain temperature, the intensity stops increasing and begins to fall following a Debye model as the temperature keeps rising. In addition to the absolute intensity change, the shape and the relative intensity of the diffusion peak change as well. The exact behavior depends on the iron coverage and deposition temperature. The change of the profile is irreversible even if the temperature drops to its previous value. The abnormal change in profile reflects that the Fe overlayer undergoes a re-arrangement.

The up-shift of the intensity at certain temperature during the annealing depicts the transition of the surface from the as-grown state to a more ordered surface. The annealing appears to remove the misfit dislocations and limited diffusion of the as-grown film. The change resulted in a radical improvement in the quality of the film. This change arises from the re-arrangement of surface atoms, not necessary the intermixing at the Fe/Cu interface. Auger measurements show that the change corresponds to a small, but significant, drop in the iron Auger signal averaged over the topmost surface layers. The lower intensity of the as-grown film deposited at lower temperature implies a large number of surface defects and is expected when there are a number of simultaneously growing layers at the surface. Such behavior is expected when the surface diffusion coefficient is too small to allow migration of atoms from the point of deposition to a nearby island or step edge, or when the barrier to migration across a step is significant.

The largest deviation from the straight line also happens for samples deposited at low temperature, Figure 79 and Figure 80. When the iron is deposited at high temperature, the re-arrangement may have taken place and reached its equilibrium state at the same time

Figure 79. Temperature dependence of 1ML Fe/Cu(100) deposited at various temperatures.

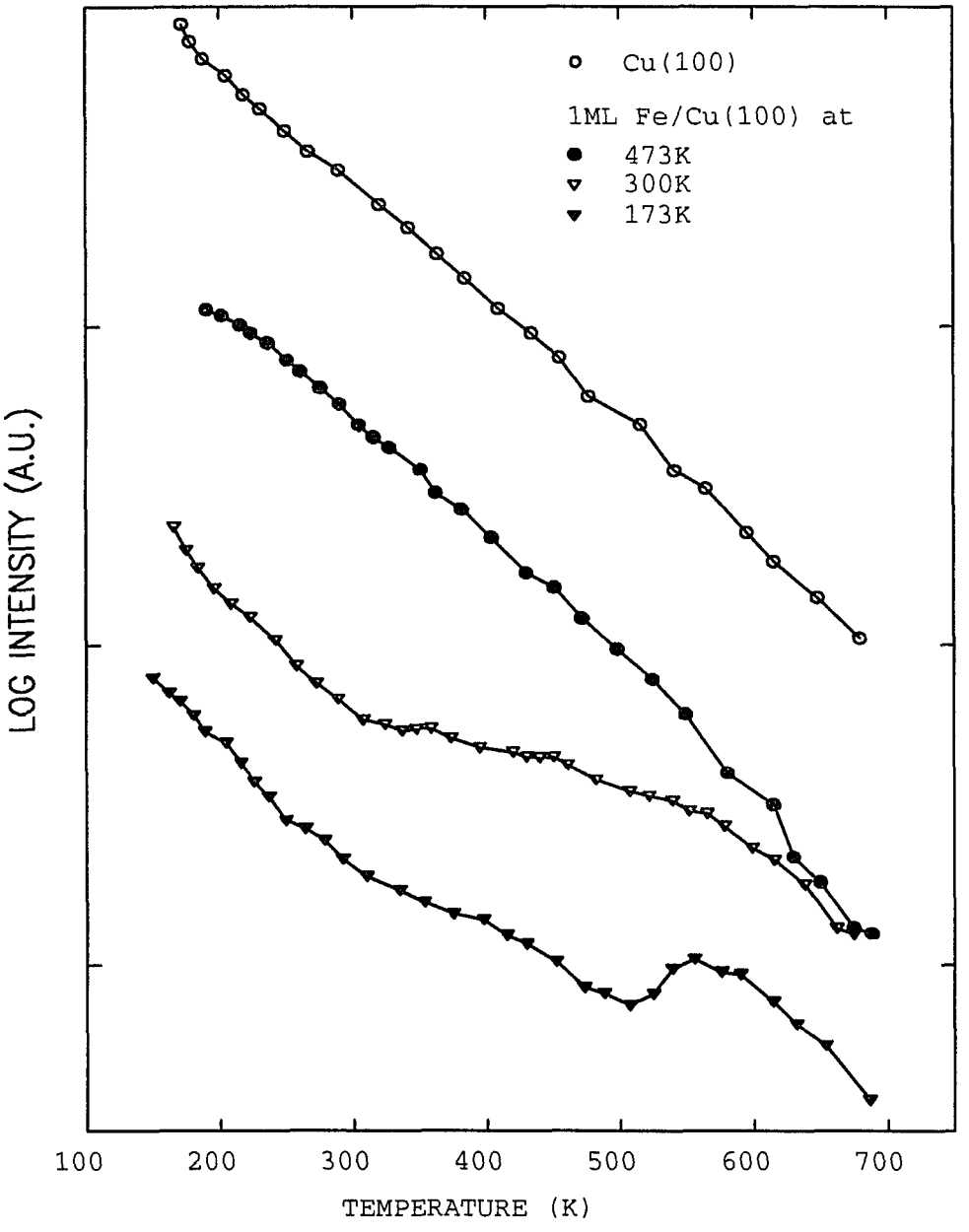

Figure 80. Temperature dependence of 3ML Fe/Cu(100) deposited at various temperatures.

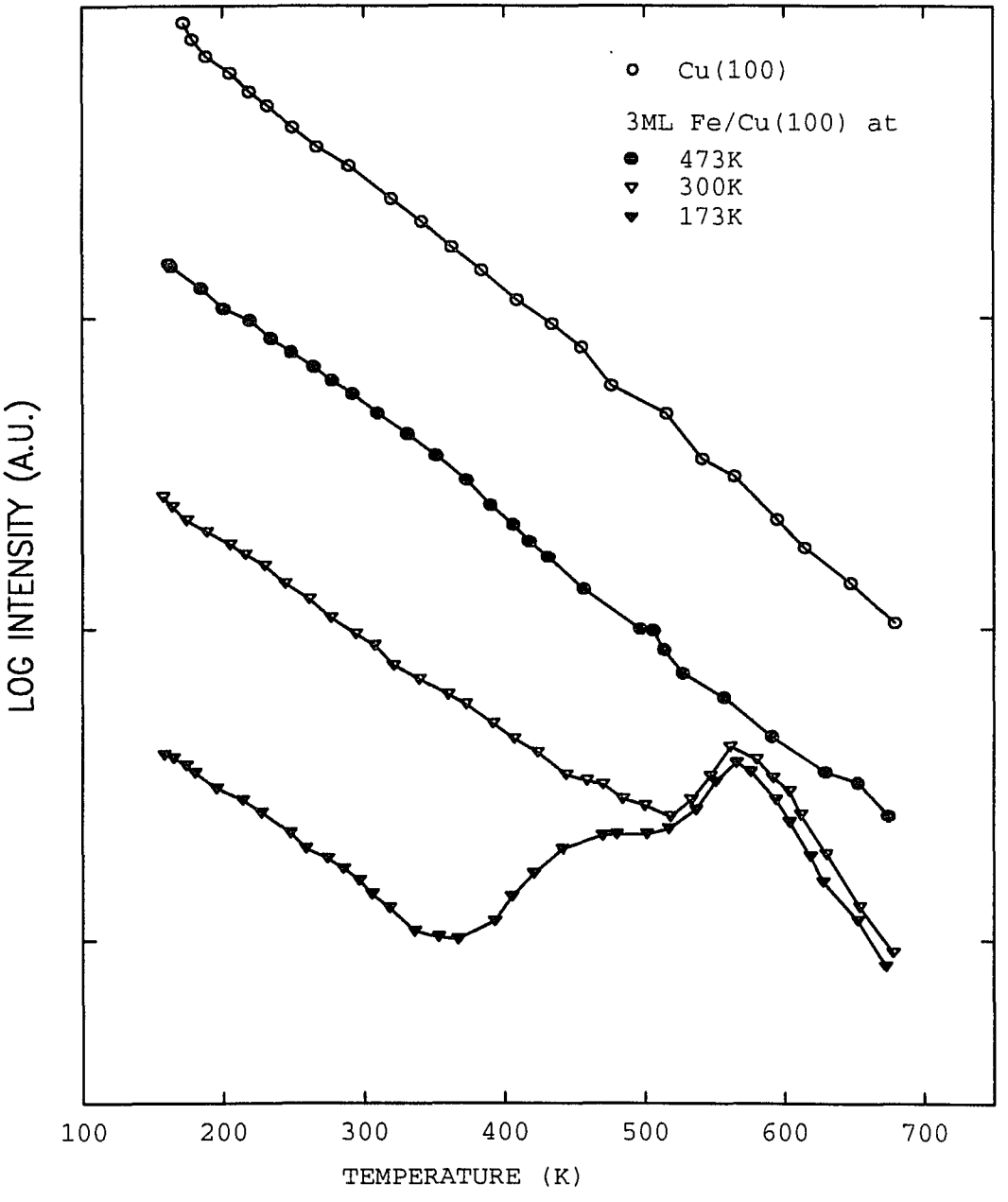

because of higher mobility of the surface atoms at this temperature. Therefore, the up-shift of the intensity is less significant in the annealing process followed.

The deviation from the straight line is maximum when the iron coverage is about 3 ML, Figure 80. A re-arrangement of the surface atoms is easier to detect at this coverage. When there is less iron on the surface, the diffraction signal is mostly from the Cu substrate. Thus the signal from deposited Fe and the surface re-arrangement are weaker. On the other hand, when there is more Fe on the surface, the surface is covered completely by the Fe film and the diffraction signal mostly comes from it. Therefore, it is also not easy to see directly the transformation underneath.

The on-set temperature of the intensity up-shift depends on the Cu substrate and the deposition conditions. The shift happens roughly in two temperature regimes: 250K and 500K. They should relate to some of the states such that the surface atoms begin to move around or jump over steps. The complexity of the problem does not enable a quantative analysis at the present time.

5.3 Spot Profiles of Clean Cu Surfaces

The spot profile of the clean Cu surface has a FWHM significantly larger than the instrument response function. The FWHM of the central narrow peak is mainly caused be the finite size of the domains on the surface. Figure 81 is a spot profile of the clean Cu(100) measured at the out-phase condition at low temperature. The broad diffusion peak is barely visible even under the out-phase condition. It is caused by the interference between layers. It indicates that the surface is very smooth. The solid line is the sum of two gaussian functions and a straight line background which best fit the experiment points. The FWHM and the intensity of the peaks are two of the fitting parameters.

Figure 81. Spot profile (out-phase) of clean Cu(100) surface at 173 K.

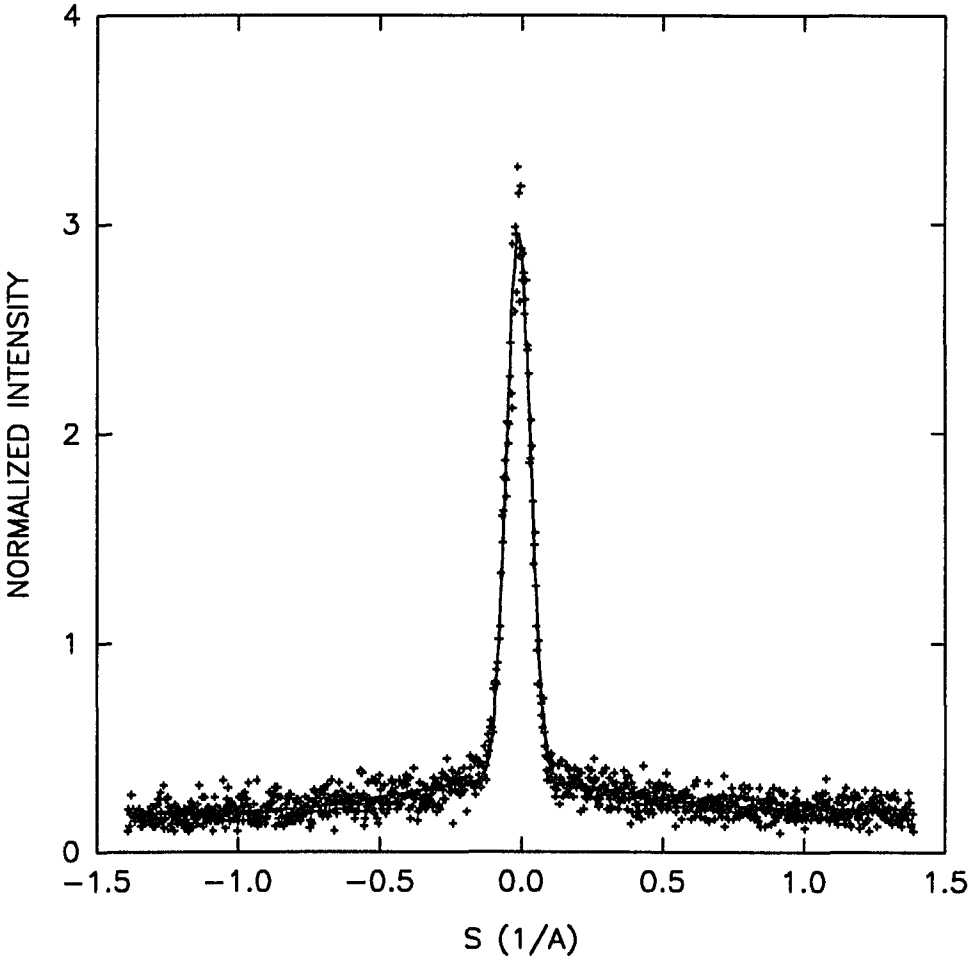

The narrow peak is the result of the convolution of the instrument response function and the diffraction signal from the finite size domains (or islands and mosaics) of the Cu surface. The transfer width of the HRLEED is much larger than the size of the domains, i.e. coherence length of the surface. The average coherence length of the Cu surfaces can be determined from the FWHM of the narrow peak in the spot profiles. The three Cu surfaces have different average coherence lengths ranging from 120(±10) Å to 200(±10) Å at room temperature depending on the cleaning and annealing process. Table 2 is a list of the measured coherence length for the three Cu sample surfaces. The limited coherence length of the Cu surface has great implication to the explanation of the experiment data of Fe thin film growth on a Cu surface.

The diffusion peak is due to the defects (roughness, steps) within the domains and is visible only in the out-of-phase condition. The average terrace length can be estimated from the half width of the diffusion peak at the out-of-phase condition. The value depends on the sample preparing process. A typical value is 12(±3) Å for a Cu(100) surface.

Table 2. Coherence length of the three Cu samples at room temperature.

Coherence Length(Å)	Cu(100)	Cu(111)	Cu(110)
0ML	180±10	180±10	180±10
1ML	150±10	140±10	130±10
3ML	130±10	130±10	120±10

5.4 Spot Profiles of Fe/Cu(100)

As Fe is deposited on the Cu(100) surface, the spot profiles depend strongly on the deposition conditions (deposition temperature, coverage), Figure 82. In all cases, the narrow peak is dominant under either the in-phase and out-of-phase conditions. Also, the narrow peak is slightly broader than the one of the clean Cu(100) surface. The corresponding coherence length is about 110(±10) Å at room temperature after deposition. The major change of the profiles under various deposition conditions lies in the diffusion peak. With 1 ML of Fe deposited on the substrate at low temperature, the diffusion signal has a 2-dimensional ring structure in the out-of-phase condition. If the primary electron energy moves away from the out-phase condition, the ring structure disappears and only the central peak is left. Figure 83 shows the change of the profile as the primary electron energy changes from the out-phase condition to the in-phase condition. This ring structure can only be observed at coverages not too far away from 1 ML and deposited at low temperature. The ring structure is produced by certain periodicity on the surface, i.e. constant island size or island spacing. This indicates that at low substrate temperature Fe grows in a 3-dimensional island mode with more or less the same size for the first one or two monolayers. The size of the 3-dimensional island can be estimated from the ring diameter and turns out to be 9(±2) Å. The structure is not thermally stable. As the sample being annealed to higher temperatures, an irreversible transition takes place on the surface. The evidence is that the ring structure of the profile shrinks and eventually disappears when the sample is annealed to high temperature, Figure 84. As the Fe atoms gain their mobility, the 3-dimensional islands begin to merge into larger island. The defects on the surface are reduced by the annealing process.

With the Fe coverage of 3 ML deposited at low temperature, the ring is almost invisible (Fig. 85). Figure 86 is the profile for 3ML Fe/Cu(100) deposited at room temperature. It shows how the narrow central peak and the broad diffusion peak are fitted

Figure 82. Comparison of spot profiles with different Fe coverages and deposited at different temperatures.

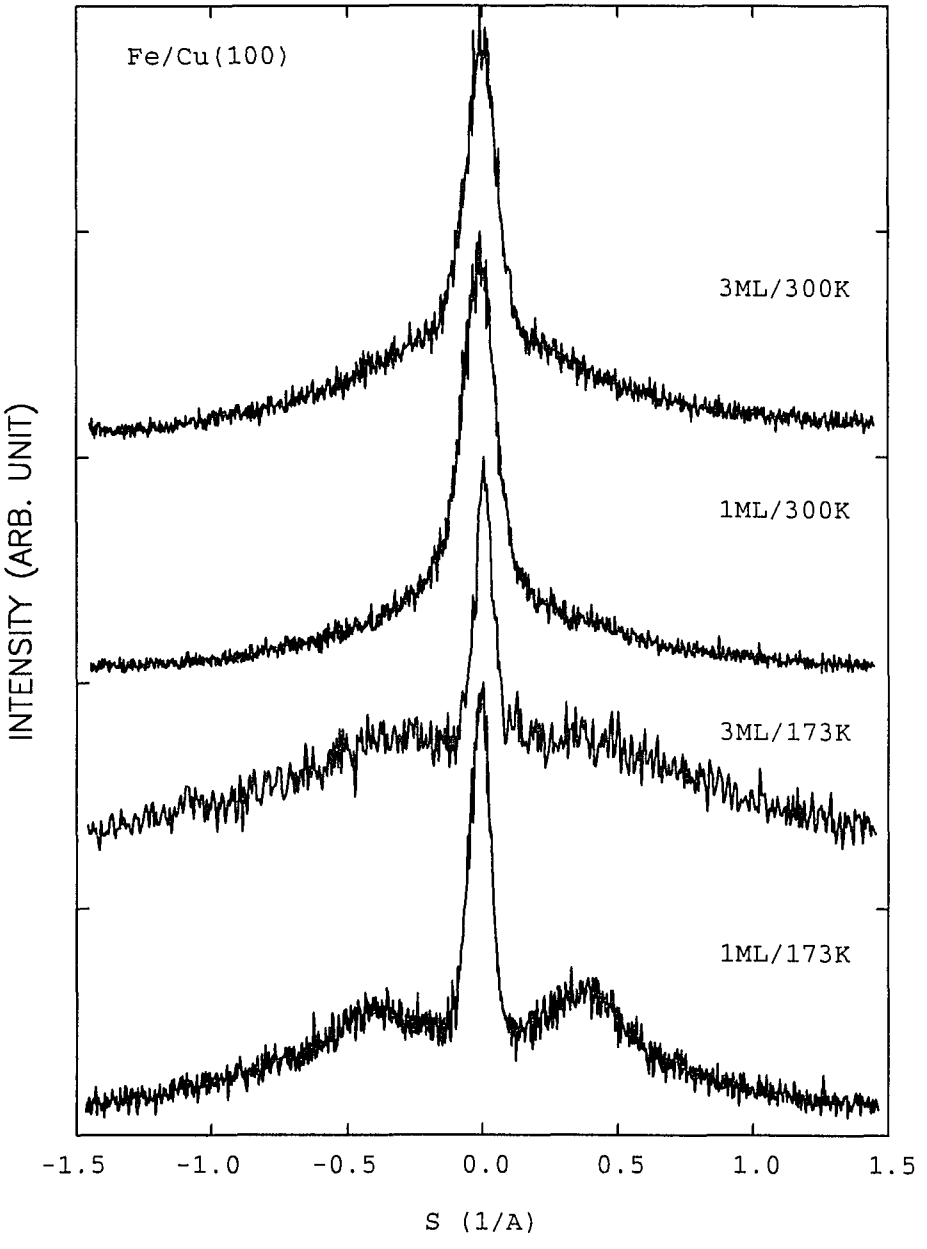

Figure 83. Variation of spot profiles of 1ML Fe on Cu(100) deposited at 173K as the primary electron energy changes.

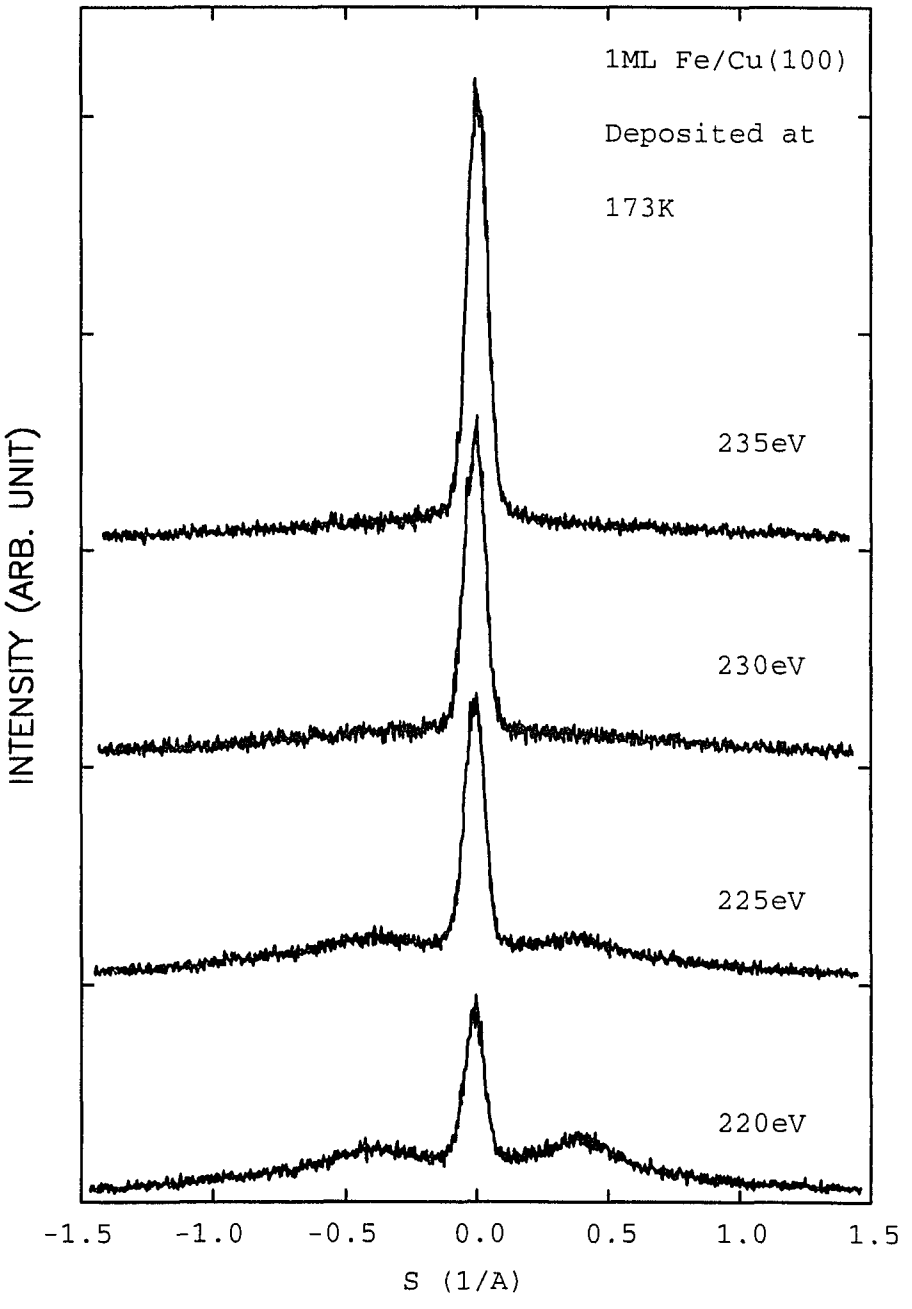

Figure 84. Variation of spot profiles of 1ML Fe on Cu(100) deposited at 173K as temperature rises from low to high.

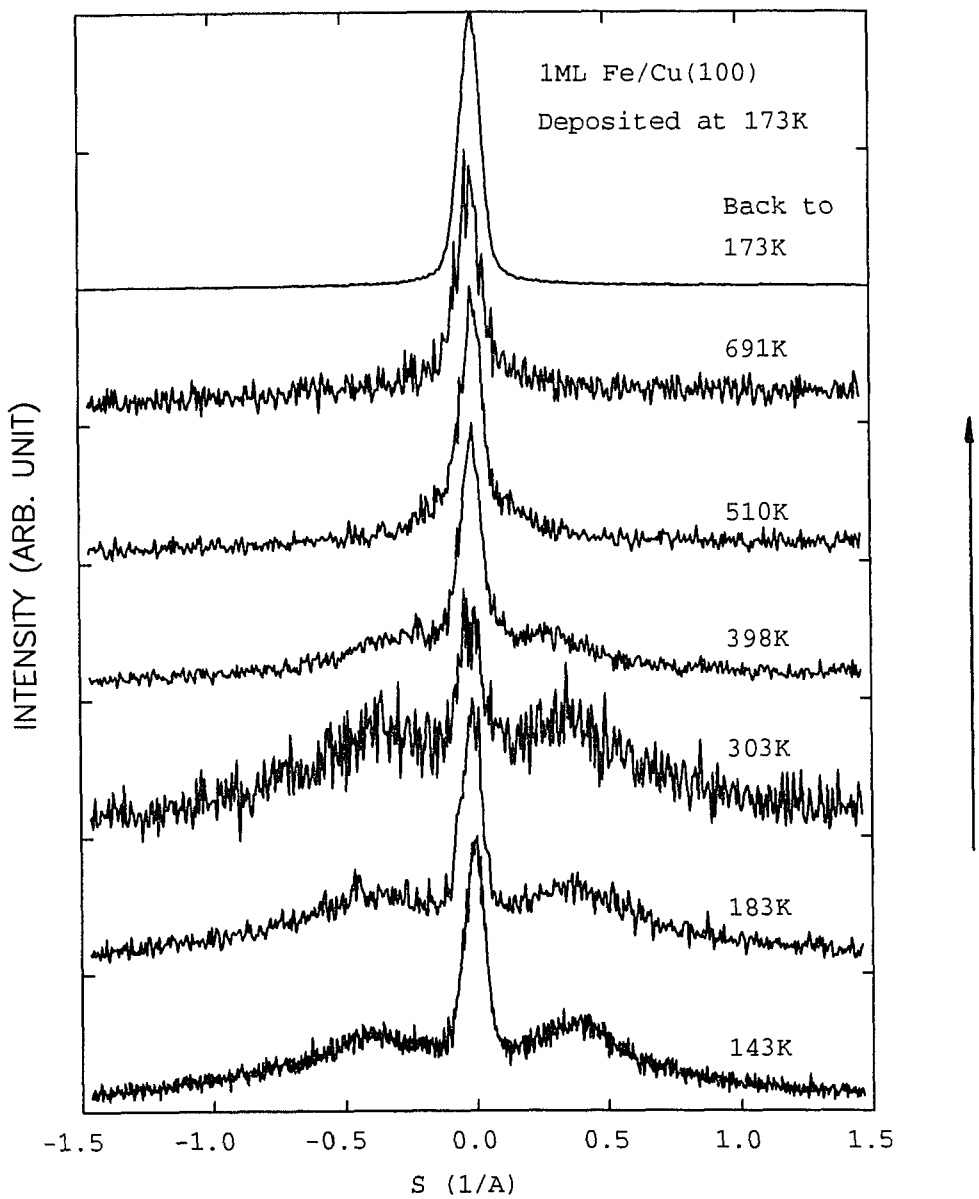

Figure 85. Variation of spot profiles of 3ML Fe on Cu(100) deposited at 173K as the primary electron energy changes

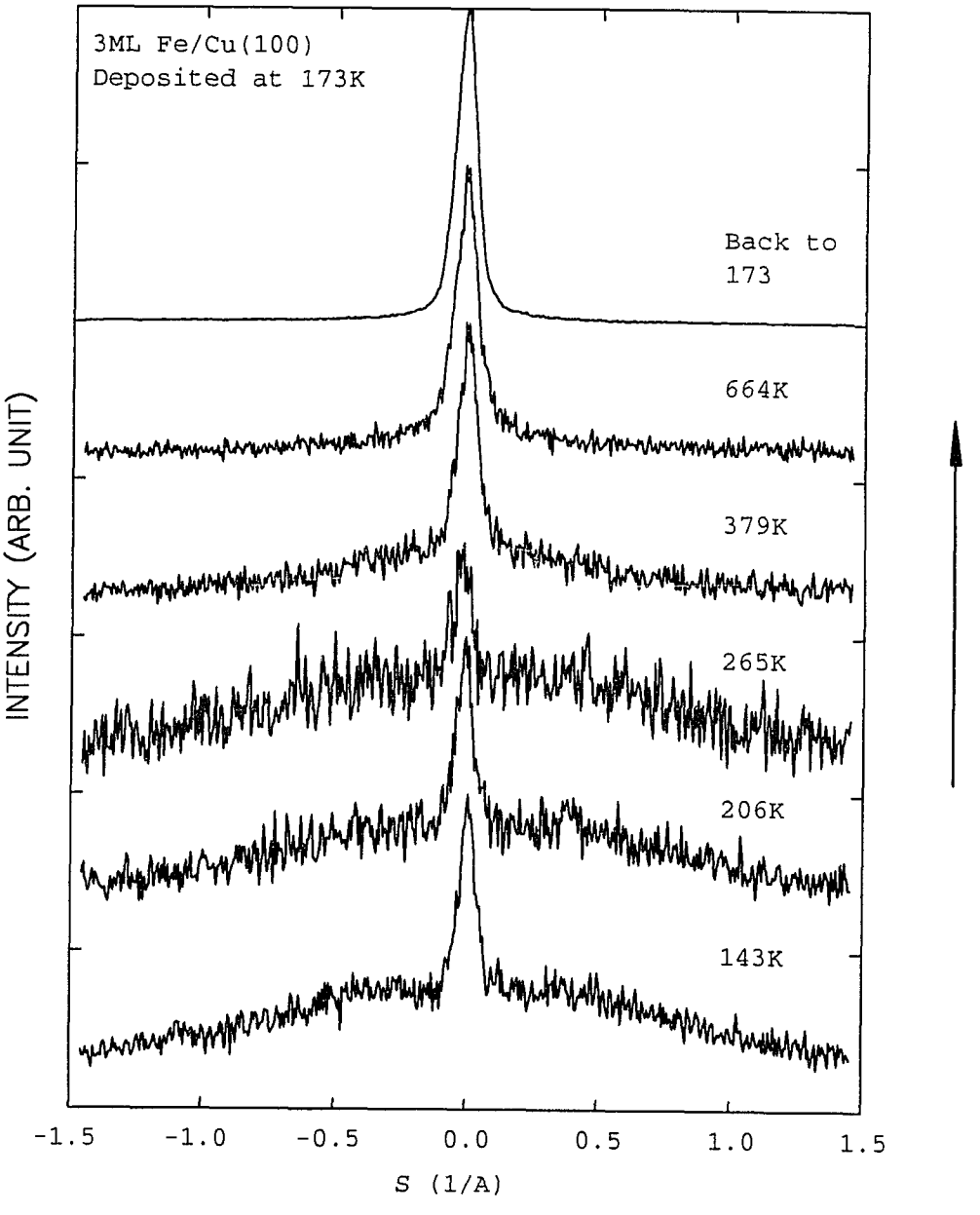

Figure 86. A typical spot profile composed of a sharp central spike and a broad diffusion peak.

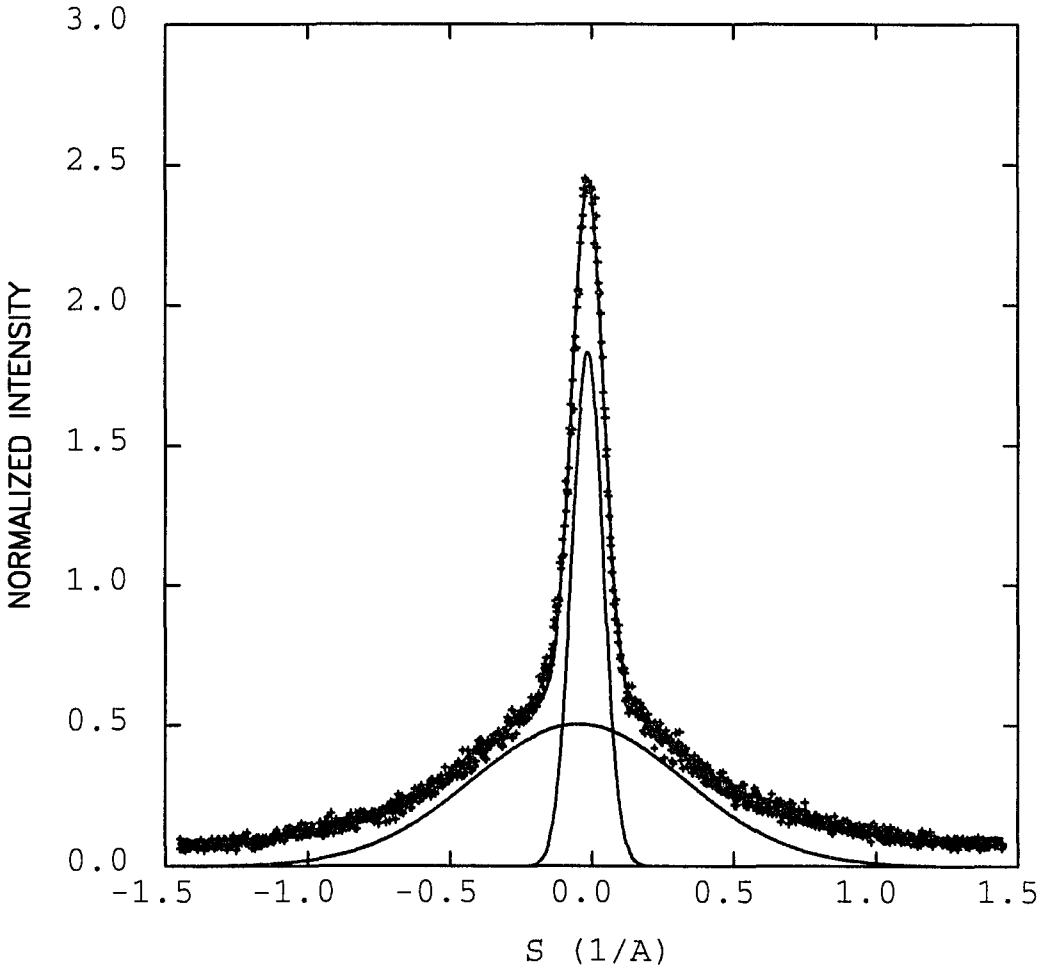

by two gaussian functions. For higher Fe coverage the diffusion signal is just a broad peak with higher relative intensity. For depositions at room temperature and high temperature, the diffusion signal is also a smooth broad peak with less relative intensity for high temperature deposition. The spot profile measurements suggest that the films grown at higher temperature (473K) are of better quality than those at lower temperature.

Figure 87 is an attempt to compare the computed spot profile with the measured data for the 1ML Fe/Cu(100) using the procedure outlined in Chapter 2. The solid line is the computed result of a 2-layer system with the following parameters: coherence length = 30 atomic distances; l = 0, 1, 2 with $p_0 = p_1 = p_2 = 1/3$; Γ = 1, 2, 3, 4, 5 with P(3) = 0.56, P(2)=P(4) = 0.21, P(1)=P(5)=0.01 (Gaussian distribution) and the coverage θ = 1ML. The shape of the profile matches the key features of the data, ie. the width and the position of peaks. However, the intensity does not match so well.

For all the deposition temperatures and coverages we investigated, the annealing process always reduces the diffusion peak in the profiles with most significant change for low deposition temperature and low coverage. The change is irreversible even if the temperature is brough back to its start point. The annealing process mentioned here is actually the temperature dependence measurement.

We can reach the following conclusions from the spot profile measurement. The sample grown at high temperature is stable and produces a smooth surface. The sample grown at low temperature is not smooth and shows an irreversible structural transformation as the temperature increases. The annealing process reduces the number of defects of the film grown at low temperature.

Figure 87. Measured and computed profiles. Data measured at the out-phase condition from the sample 1ML Fe/Cu(100) deposited at 173K.

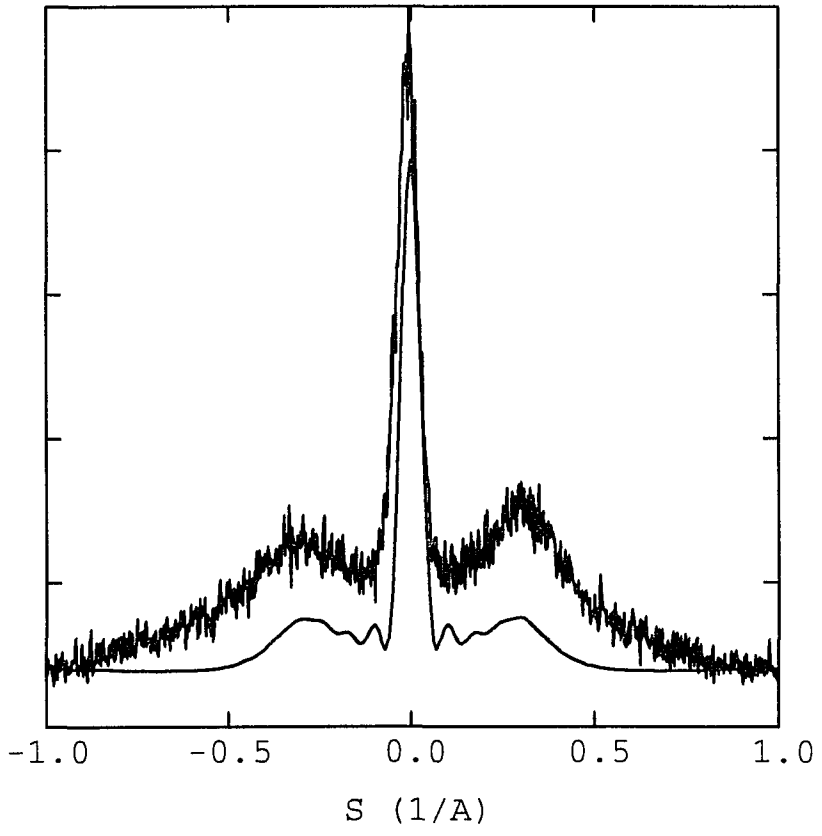

5.5 Auger Electron Spectra and the Growth Model

In the temperature dependent measurements, the sample is heated from low temperature (173 K) up to high temperature (673 K). The sample is then let to cool down to room temperature. Auger electron spectra are recorded at room temperature before and after the temperature dependent measurement. For the sample covered with Fe, the AES signal for the Fe/Cu ratio is reduced after the sample has been heated. The annealing temperature is not high enough to evaporate the Fe deposited on the surface. To find out the cause of the reduced Fe AES signal, we measured the ion sputtering AES profile of the annealed sample. During the sputtering process, we keep the vacuum chamber under 10^{-6} torr of Ar partial pressure. The ion gun is set to its low setting: 10 mA emission current and 500 V ion energy. We measure the AES spectrum every 20 minutes. Figure 88 is the AES intensity vs. the sputtering time. The Fe/Cu ratio goes down monotonously as the sputtering time increases. This is suggesting that the surface Fe atoms do not diffuse in the Cu substrate during the annealing process. Otherwise we would have seen that the Auger Fe/Cu ratio oscillates in the sputtering profile when the top layer atoms are bombarded away. On the other hand, the surface segregation behavior in the Fe-Cu system can be a very strong effect because of its thermodynamic properties. If the substrate surface was ideally flat, then the differences in the surface free energies and the positive mixing heat will promote a surface segregated state in which Cu atoms are exposed on the surface, Figure 89. The annealing process tends to increase the mobility of the Fe atoms and wet the surface with the Fe atoms. This would produce a smooth layer of Fe on the substrate surface and increased the Auger Fe/Cu signal ratio after the annealing. This picture can explain the other LEED measurements, such as sharper and brighter spots for depositions at higher substrate temperature, more significant changes in the spot profiles for depositions at lower substrate temperature and the annealing process. However, it can not explain the decrease of Auger Fe/Cu ratio after the annealing. Because the Cu surface is not as flat as the Si surface, we need to take into consideration that it has only a limited

coherence length in order to explain the experiment data. Figure 90 schematically shows the diffusion process and can be used to explain the drop in the Fe/Cu signal. The non-perfect substrate surface reduces the segregation and produces a mono-layer of Fe after the deposition. The annealing process rearranges the Fe atoms to produce a smooth surface. The substrate Cu atoms get exposed because the Fe atoms on top of them diffuses to neighboring hollow sites. This will cause the decrease of the Auger Fe/Cu ratio after the annealing.

Figure 88. AES sputtering profiles of 3ML Fe/Cu(100).

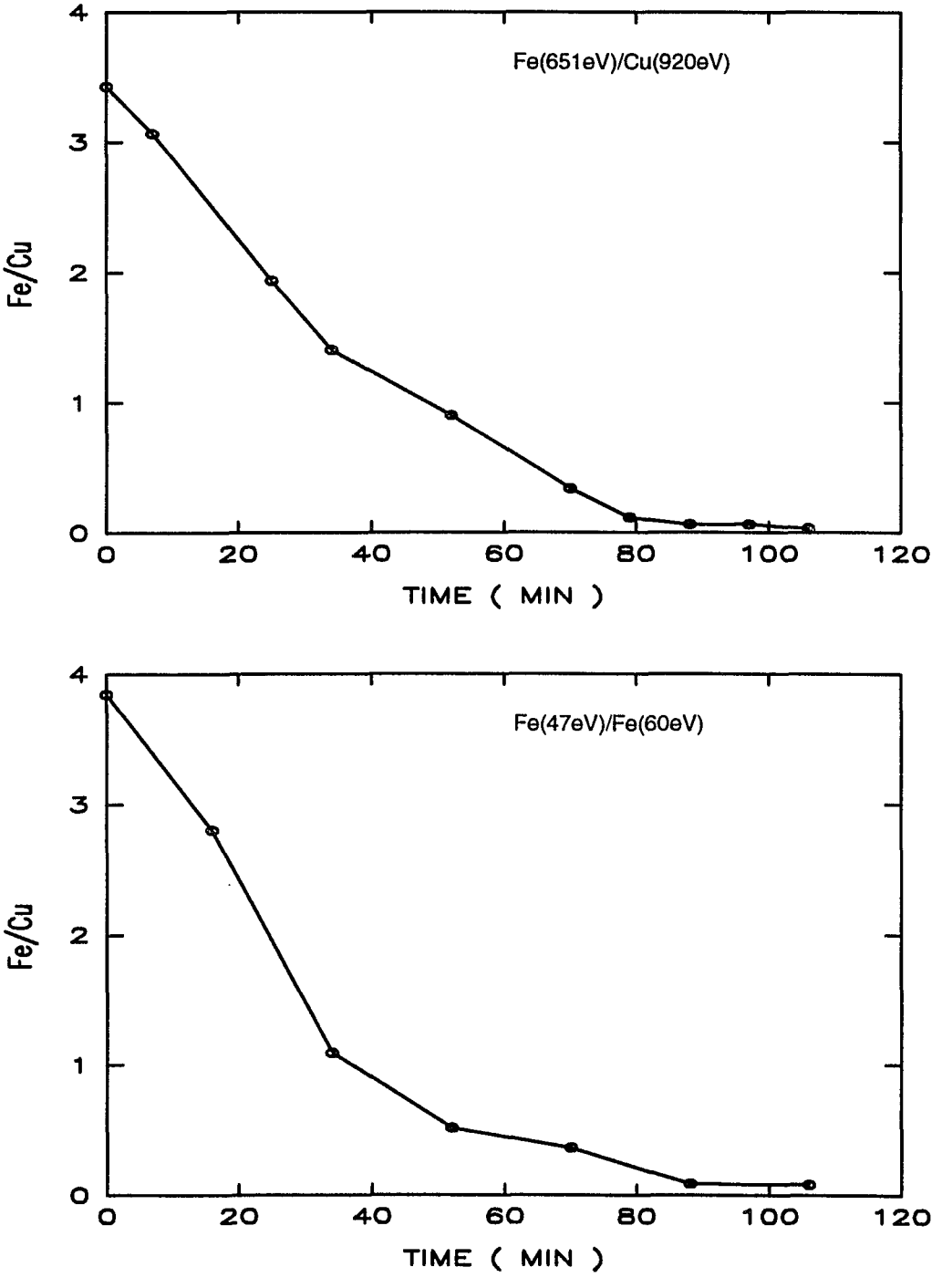

Figure 89. Auger electrons from the overlayer on a flat substrate surface.

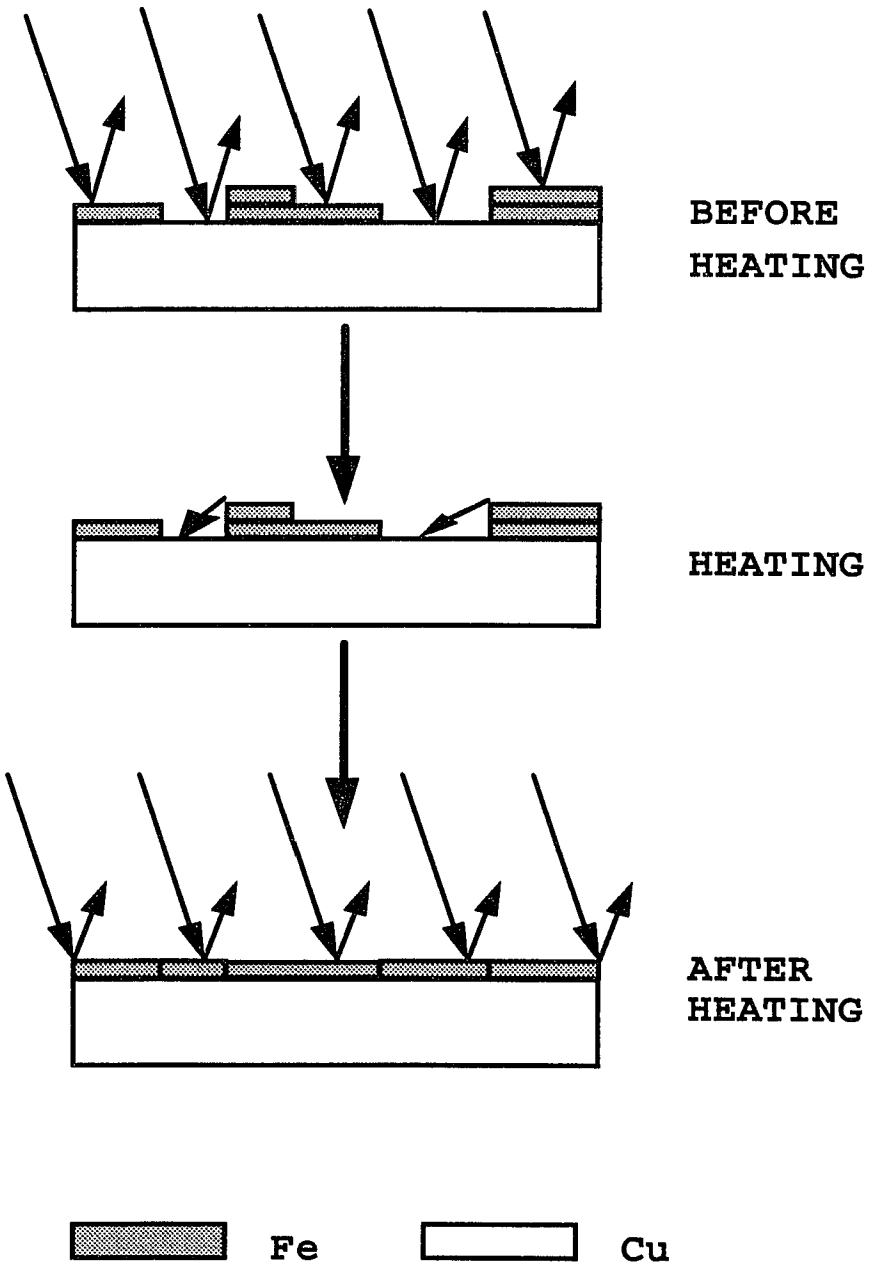

Figure 90. Auger electrons from the overlayer on a stepped substrate surface.

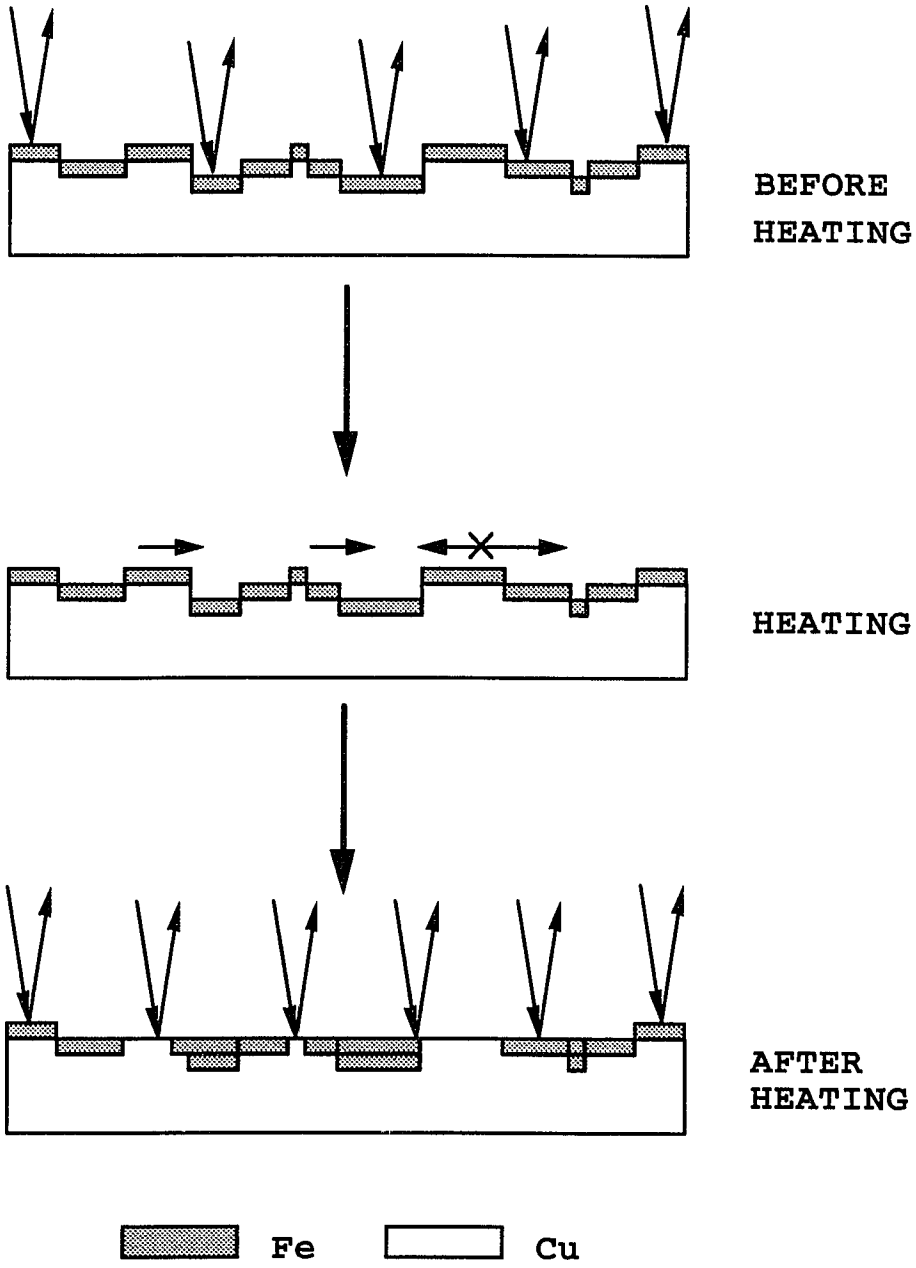

CHAPTER 6

SUMMARY

The principal aim of this paper is to demonstrate, through observations of the intensity of the LEED spots, how surface order develops at various stages of growth and thermal treatment of iron films on the copper substrates. Our HRLEED measurement shows that the growth of Fe on the Cu surfaces is a complex process. It is far from the simple hetero-epitaxial system that might be expected on the basis of lattice match and mutual immiscibility. At low deposition temperature, Fe initially grows into 3-dimensional islands for the first few of layers. As the 3-dimensional islands grow in size they will tend to merge so that further rearrangement of iron within islands will be possible. Because of limited diffusion, the resulting Fe overlayer has a large number of surface defects at all coverage we studied (up to 6 ML). At high deposition temperature, Fe film grows in a well-ordered layer-by-layer manner. It is in accordance with the previous investigations [3, 6, 9, 16, 19, 58] which have indicated that the "best" expitaxial films are grown in the higher temperature regime. At room temperature there are two stages of growth, multilayer growth followed by layer-by-layer growth. The Fe films grown at low and room temperature are not thermally stable and will undergo an irreversible structural re-arrangement when heated to high temperatures. Annealing the Fe/Cu system to 500K will cause interfacial re-arrangements that relieve some of the lattice strain and give an unknown degree of inter-mixing. The annealing process helps to reduce the number of defects of the overlayer, thus improving the quality of the thin film.

Under the same growth condition, the best Fe expitaxial film is grown on Cu(100) surface. Cu(110) and Cu(111) surfaces produce poor Fe overlayer with Cu(111) the most difficult to grow on. This makes the Cu(100) the most important surface to study the magnetic property of the Fe expitaxial film.

A model of surface atom re-arrangement is introduced to explain the LEED spot intensity up-shift and the drop of the Fe Auger signal by the annealing process. The model is based on the fact that the Cu substrate surface has a finite coherence length, which is more realistic than assuming the substrate is ideally flat as most people do. It allows us to explain the Auger signal drop without using the inter-mixing model, which is not thermodynamically favorable because of the positive mixing heat of Fe/Cu.

It is clear that such a complex growth process will invalidate many of the magnetic measurement results. In such measurements the structure of the surface is constantly changing. The presence of feromagnetism is probably due to the bcc inclusion during the low temperature growth.

APPENDIX

A.1 Surface Energy and Growth Mode

The thermodynamic properties such as the surface energy can be used to estimate when any one of the three growth modes is likely to occur. Let us consider the energy difference between the two epitaxial overlayer arrangements depicted in Figure 91. The inputs to this calculation are three macroscopic surface tensions: γ_A , γ_I and γ_S - the free energy/unit area at the overlayer-vacuum interface, the overlayer-substrate interface and the substrate-vacuum interface, respectively. We may assume, without loss of generality, that the Volmer-Weber cluster occupies half the available surface area (A). It follows immediately that

$$E_{FV} = (\gamma_A + \gamma_I) \cdot \text{Area}$$

$$E_{VW} = \tfrac{1}{2}(\gamma_A + \gamma_I + \gamma_S) \cdot \text{Area}$$

and the energy difference of the two growth modes,

$$\Delta E = E_{FV} - E_{VW} = \tfrac{1}{2}(\gamma_A + \gamma_I - \gamma_S) \cdot \text{Area}$$

Therefore, we expect complete wetting (FV growth) when $\Delta\gamma = \gamma_A - \gamma_I - \gamma_S < 0$, VW growth when $\Delta\gamma > 0$ and SK growth when $\Delta\gamma \cong 0$.

It is important to bear in mind that this estimate is only qualitatively useful because we have completely neglected any effects which might arise from the anisotropy of the surface tensions. Even then, it is not entirely clear what one should choose for γ_I for any particular epitaxial pair. Existing methods [57] of measurement rely on bulk grain boundary data which are not obviously transferable to the epitaxial situation of interest where additional contributions from misfit dislocations, strain, etc., might be significant.

Figure 91. Simple thermodynamic explanation of growth mechanism (surface energy approach)

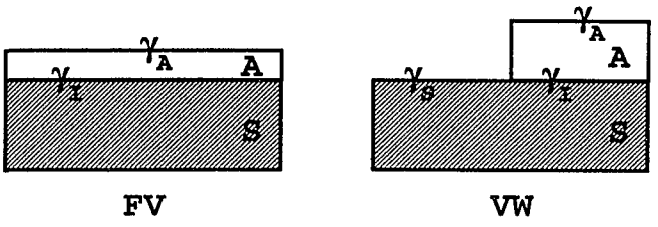

A.2 SIMULATE.C

The C program to simulate the epitaxial growth and compute the LEED spot profile. Compiled using the Borland C++ version 3.1 and run on a 486-50MHz PC.

```
//
// simulate.c
// program to simulate the diffraction spot profile from rough surface
// with cubic primitive cell (a,b,c).
// This is a 1-dimensional model. lattice constant 'b' is obsolete.
//
// by Yuqun Cao
// 5/24/93

#include <stdlib.h>
#include <stdio.h>
#include <conio.h>
#include <time.h>
#include <math.h>
#include <complex.h>

// discrete distribution function

typedef struct {
      int i;            // integer value, e.g. layer, step size, etc
      double pi;        // probability of taking value i
      } POINT_T;
```

```
typedef struct {
      int n;            // number of points
      POINT_T *prob;    // probabilities,sum(p1,...pn)=1
      } DIST_T;

// global variables

// parameters
double phase;           // k_perpendicular*c, (c - lattice constant)
int grid_size;          // i.e. coherence length
int max_iteration;      // number of iterations
int num_output;         // number of output points
DIST_T size_dist;       // step size distribution
DIST_T layer_dist;      // layer distribution

// variables
double      ave_step_size;    // average step size
int         *surface;         // surface atom positions
double      *intensity;       // intensity array, size = num_output


void get_para(void)
// read parameters from para.ini into variables. The parameters appear
// in the following order, seperated by white space, i.e.,space,tab,CR.
// In the distribution functions, 'n' must match the number of points.
//
// para.ini:
```

```
// phase
// grid_size
// max_iteration
// num_output
// size_dist.n
// size_dist.prob[1].i, ..., prob[n].i
// size_dist.prob[1].pi, ..., prob[n].pi
// layer_dist.n,
// layer_dist.prob[1].i, ..., prob[n].i
// layer_dist.prob[1].pi, ..., prob[n].pi
{
   FILE *fp;            // input file
   int i;
   int success;         // number of parameters successfully read

   fp = fopen("para.ini","rt");
   if(!fp) {
      perror("\nOpen file para.ini error.\n");
      exit(1);
      }

   success = fscanf(fp,"%lg%d%d%d", \
                  &phase, &grid_size, &max_iteration, &num_output);
   if(success != 4) {
      perror("\nReading parameters: " \
             "a, phase, grid_size, max_iteration, num_output error.\n");
      exit(1);
```

```
    }

fscanf(fp,"%d", &size_dist.n);
size_dist.prob = (POINT_T *)calloc(size_dist.n, sizeof(POINT_T));
if(!size_dist.prob) {
   perror("\nMemory allocation for 'size_dist' error.\n");
   exit(1);
   }
for(i=0, success=0; i<size_dist.n; i++)
   success += fscanf(fp, "%d", &size_dist.prob[i].i);
if(success != size_dist.n) {
   perror("\nRead 'size_dist.prob[].i' error.\n");
   exit(1);
   }
for(i=0, success=0; i<size_dist.n; i++)
   success += fscanf(fp, "%lg", &size_dist.prob[i].pi);
if(success != size_dist.n) {
   perror("\Read 'size_dist.prob[].pi' error.\n");
   exit(1);
   }

fscanf(fp, "%d",&layer_dist.n);
layer_dist.prob = (POINT_T *)calloc(layer_dist.n, sizeof(POINT_T));
if(!layer_dist.prob) {
   perror("\nMemory allocation for 'layer_dist' error.\n");
   exit(1);
   }
```

```
   for(i=0, success=0; i<layer_dist.n; i++)
      success += fscanf(fp,"%d",&layer_dist.prob[i].i);
   if(success != layer_dist.n) {
      perror("\nRead 'layer_dist.prob[].i' error.\n");
      exit(1);
      }
   for(i=0, success=0; i<layer_dist.n; i++)
      success += fscanf(fp,"%lg",&layer_dist.prob[i].pi);
   if(success != layer_dist.n) {
      perror("\nRead 'layer_dist.prob[].pi error.\n");
      exit(1);
      }

   fclose(fp);
   }


void print_para(FILE *fp)
{
   int i;

   fprintf(fp,"\nParameters read in from 'para.ini':");

   fprintf(fp,"\nphase=%f",phase);
   fprintf(fp,"\ngrid_size=%d",grid_size);
   fprintf(fp,"\nmax_iteration=%d",max_iteration);
```

```
   fprintf(fp,"\nnum_output=%d",num_output);

   fprintf(fp,"\n\nsize distribution:\nn=%d\nprob=",size_dist.n);
   for(i=0; i<size_dist.n; i++)
      fprintf(fp,"(%d, %f) ",size_dist.prob[i].i, size_dist.prob[i].pi);

   fprintf(fp,"\n\nlayer distribution:\nn=%d\nprob=",layer_dist.n);
   for(i=0; i<layer_dist.n; i++)
      fprintf(fp,"(%d, %f) ",layer_dist.prob[i].i,
layer_dist.prob[i].pi);

   //printf("\nPress any key to continue ...\n");
   //getch();

   return;
   }

void init(void)
{
   int i;

   intensity = (double *)calloc(num_output,sizeof(double));
   if(!intensity) {
      perror("\nMemory allocation for intensity[] error.\n");
      exit(1);
      }
```

```
   surface = (int *)calloc(grid_size+1, sizeof(int));
   if(!surface) {
      perror("\nMemory allocation for surface[] error.\n");
      exit(1);
      }

   randomize();          // initialize the system random # generator
   for(i = 0; i < num_output; i++) intensity[i] = 0;
   }

void clean_up(void)
{
   free(intensity);
   free(surface);
   free(size_dist.prob);
   free(layer_dist.prob);
   printf("\nDone\n");

   }

double gen_rand(DIST_T *dist)
// generate a random number according the discrete distribution function
{
   int            i;
   double   *s;          // working space to select a random number
   double   r, val;
```

```
   s = (double *)calloc(dist->n, sizeof(double));

   s[0] = dist->prob[0].pi;
   for(i = 1; i < dist->n; i++) s[i] = s[i-1] + dist->prob[i].pi;

   r = (double)rand()/RAND_MAX;     // r is normalized to 1
   r *= s[dist->n - 1];       // r is normalized to the sum of pi's

   for(i = 0; r > s[i]; i++); // compare r with selection critiria

   val = dist->prob[i].i;     // look up the value
   free(s);                   // free the memory!

   return val;
   }

void gen_surface(void)
// generates a stepped surface using size and layer distribution
// function. size <= grid_size
{
   int size = 0;        // actual size
   int old_layer = -1;
   int layer;           // randomly generated layer, -1 marks the end
   int step_size;       // randomly generated step size

   while(1) {
      step_size = gen_rand(&size_dist);         // generate a new step
```

```
      if(size + step_size > grid_size) break;    // stop if won't fit

      do {
         layer = gen_rand(&layer_dist);                // at new layer
         } while(layer == old_layer);

      while(step_size-- > 0) surface[size++] = layer;
      old_layer = layer;
      }

   while(size <= grid_size) surface[size++] = -1;// fill up the rest
   }

void prt_surface(void)
{
   int i;

   printf("\nSurface atom position:\n");
   for(i = 0; i < grid_size; i++) printf("%3d\n",surface[i]);

   return;
   }

void comp_intensity(void)
// amplitude:
// A(K)=[sum on x](exp(iKx))=[sum on (n,l)](exp(iKa*n+iphase*l),
// where x is the surface atom positions and K the momentum transfter.
```

```
// intensity(K) = square(|A(K)|).
// Ka - K_parallel*a, [-pi,pi]
// phase - K_parpendicular*c, [0, 2pi]
{
   long double Ka;                          // K_parallel*a
   long double dKa = 2*M_PI/(num_output-1);// increament
   long double amp_real, amp_imag;
   int n,i;

   for(Ka = -M_PI, i = 0; i < num_output; i++, Ka += dKa) {
      amp_real = 0.0;
      amp_imag = 0.0;

      for(n = 0; surface[n] != -1; n++) {
            amp_real += (long double)cos(n*Ka + phase*surface[n]);
            amp_imag += (long double)sin(n*Ka + phase*surface[n]);
            }

      intensity[i] += (amp_real*amp_real + amp_imag*amp_imag)/(n*n);
      }
   }

void prt_intensity(void)
{
   int    i;
   double Ka;
   double dKa = 2.0/(num_output-1); // unit -- pi
```

```
    FILE   *fp;

    fp = fopen("sim.out","wt");
    if(!fp) {
       perror("Open output file 'sim.out' error.\n");
       exit(1);
       }

    print_para(fp);
    fprintf(fp,"\nIntensity:\n");

    for(i = 0, Ka = -1; i < num_output; i++, Ka += dKa)
       fprintf(fp,"%8.5f  %15e\n", Ka, intensity[i]);

    fclose(fp);
    }

void main()
{
    int iter = 0;  // number of iteration so far
    int i;

    get_para();    // read parameters from file para.ini to variables
    print_para(stdout);  // check parameters

    init();        // use the parameter just read in to initialize
```

```
printf("\nI am working on it.\n");
while(iter++ < max_iteration) {
   if(fmod(iter,500) == 0) printf("iter=%d\n",iter);
   gen_surface();
   comp_intensity();
   }

for(i = 0; i < num_output; i++) intensity[i] /= iter;     // normalize

prt_intensity();      // print result to a file.

clean_up();           // free allocated memory
}
```

BIBLIOGRAPHY

1. O. Haase, Z. Naturforsch A**14**, 920 (1959)
2. Y. C. Lee, H. Min, and P. A. Montano, Surf. Sci. **166**, 391 (1986)
3. Y. Darici, J. Marcano, H. Min, and P. A. Montano, Surf. Sci. **182**, 477 (1987)
4. D. A. Steigerwald, I. Jacob, and W. F. Egelhoff, Jr., Surf. Sci. **202**, 472 (1988)
5. S. H. Lu, J. Quinn, D. Tian, and F. Jona, Surf. Sci. **209**, 378 (1989)
6. J. Marcano, Y. Darici, H. Min, Y. Yin, and P. A. Montano Surf. Sci. **217**, 1 (1989)
7. Y. Darici, J. Marcano, H. Min, and P. A. Montano, Surf. Sci. **217**,512 (1989)
8. R. Rochow, C. Carbone, Th. Dodt, F. P. Johnen, and E. Kisker, Phys. Rev. B**41**, 3426 (1990)
9. P. A. Montano, G. W. Fernando, B. R. Cooper, E. R. Moog, H. M. Naik, S. D. Bader, Y. C. Lee, Y. N. Darici, H. Min, and J. Marcano, Phys. Rev. Lett. **59**, 1041 (1987)
10 D. Pescia, M. Stampanoni, G. L. Bona, A. Vaterlaus, R. F. Willis and F. Meier, Phys. Rev. Lett. **58**, 2126 (1987)
11 W. A. A. Macedo and W. Keune, Phys. Rev. Lett. **61**, 475 (1988)
12 D. P. Pappas, K.-P. Kamper and H. Hopster, Phys. Rev. Lett. **64**, 3179 (1990)
13 W. Schwarzacher, W. Allison, R. F. Willis, J. Penfold, R. C. Ward, I. Jacob, and W. F. Egelhoff, Solid State Commun. 71, 563 (1989)
14. A. Clarke, P. J. Rous, M. Arnott, G. Jennings, and R. F. Willis, Surf. Sci. **192**, L843 (1987)
15. S. A. Chambers, T. J. Wagener, and J. H. Weave, Phys. Rev B**36**, 8992 (1987)
16 M. Onellion, M. A. Thompson, J. L. Erskine, C. B. Duke and A. Paton, Surf. Sci. 179, 219 (1987)
17. C. L. Fu and A. J. Freeman, Phys. Rev B **25**, 925 (1987)
18. M. Arnott, E. M. McCash and W. Allison, Surf. Sci. **269/270**, 724 (1992)

19. P. Dastoor, M. Arnott, E. M. McCash and W. Allison, Surf. Sci. **272**, 154 (1992)

20 W. B. Pearson, A Handbook of Lattice Spacings and Structures of Metals and Alloys, Vol. 2, Pergamon, New York (1967)

21 R. Boom, F. R. Boer, A. K. Nielsen and A. R. Miedema, Physica **B115**, 285 (1983)

22 C. S. Lent and P. I. Cohen, Surf. Sci. **139**, 121 (1984)

23 M. Henzler, in: the Structure of Surfaces II, Springer Series in Surface Sciences 11, 431 (1988)

24. U. Gradmann, W. Kummerle, and P. Tillmanns, Thin Solid Films **34**, 249 (1976)

25. W. A. Jesser and J. W. Matthews, Philos. Mag. **15**, 1097 (1967)

26. W. Kummerle and U. Gradmann, Solid State Commun. **24**, 33 (1977)

27. C. Rau, C. Schneider, G. Xing, and K. Jamison, Phys. Rev. Lett. **57**, 3221 (1986)

28. U. Gradmann and P. Tillmanns, Phys. Status Solidi A **539**, (1977)

29. J. G. Wright, Philos. Mag. **24**, 217 (1971)

30. W. Keune, R. Halbauer, U. gonser, J. Lauer, and D. L. Williamson, J. Appl. Phys. **48**, 2976 (1977)

31. W. Keune, R. Halbauer, U. gonser, J. Lauer, and D. L. Williamson, J. Magn. Magn. Mater. **6**, 192 (1977)

32. R. Halbauer and U. Gonser, J. Magn. Magn. Mater. **35**, 55 (1983)

33. W. Becker, H.-D. Pfannes, and W. Keune, J. Magn. Magn. Mater. **35**, 53 (1983)

34. C. Liu, E. R. Moog, and S. D. Bader, Phys. Rev. Lett. **60**, 2422 (1988)

35. R. W. Vook, Int. Metals Rev **27**, 209 (1982)

36. R. Ludeke, J. Vac. Sci. Tech. **B2**, 400 (1984)

37. E. Bauer, Z. Krist. **110**, 372 (1958)

38. F. C. Frank and J. H. van der Merwe, Proc. R. Soc. London, Ser. A **198**, 205 (1949)

39. M. Volmer and A. Weber, Z. Phys. Chem. **119**, 277 (1926)

40. J. N. Stranski and L. Krastanov, Ber. Akad. Wiss. Wien **146**, 797 (1938)

41. R. Germar, W. Durr, J. W. Krewer, D. Pescia, and W. Gudat, Appl. Phys. A **47**, 797 (1988)

42. K-P Kamper, W. Schmitt, G. Guntherodt, and H. Kuhlenbeck, Phys. Rev. B **38**, 9451 (1988)

43. K. Takayanagi, D. M. Kolb, K. Kambe, and G. Lehmpfuhl, Surf. Sci. **100**, 407 (1980)

44. K. Gurtler and K. Jacobi, Surf. Sci. **134**, 309 (1983)

45. J. W. A. Sachtler, M. A. van Hove, J. P. Biberian, and G. A. Somorjai, Surf. Sci. **110**, 19 (1981)

46. G. E. Rhead, M.-G. Barthes, and C. Argile, Thin Solid Films **82**, 201-211 (1981)

47. M. Henzler, Appl. Surf. Sci. **12**, 450 (1982)

48. J. Wollschlager, J. Falta, and M. Henzler, Appl. Phys. **A50**, 57 (1990)

49. R. L. Park, J. E. Houston and D. G. Schreiner, Rev. Sci. Instr. **43**, 60 (1971)

50. R. L. Park and J. E. Houston, Surf. Sci. **18**, 43 (1969)

51. J. E. Houston and R. L. Park, Surf Sci. **21**, 209 (1970)

52 P. Auger, J. Phys. Radium **6**, 205 (1925)

53 J. J. Lander, Phys. Rev. **91**, 1382 (1953)

54 L. A. Harris, J. Appl. Phys. **39**, 1419 and 1428 (1967)

55 R. E. Weber and A. L. Johnson, J. Appl. Phys. **40**, 314 (1968)

56 M. P. Seah and W. A. Dench, Surface Interface Anal. **1**, 2 (1979)

57 N. Eustathopoulos and J.-C. Joud, In Current Topics in Materials Science, Vol. **4**, 281, **ed.** Kaldis, Amsterdam: North-Holland

58 H. Magnan, D. Chandesris, B. Villette, O. Heckmann and J. Lecante, Phys. Rev. Lett. **67**, 859 (1991)